UNIVERSITY OF NAPLES "FEDERICO II"

Thesis submitted for the Degree of Doctor of Philosophy on

NOVEL TECHNOLOGIES FOR MATERIALS, SENSORS, AND IMAGING

21st cycle

Coordinator: Professor Giancarlo Abbate

POROUS SILICON BASED OPTICAL DEVICES FOR BIOCHEMICAL SENSING

Dr. Ilaria Rea

Supervisor: Luca De Stefano, PhD

Institute for Microelectronics and Microsystems

National Council of Research

Naples, Italy October, 2008

RINGRAZIAMENTI

Quando sono arrivata all'IMM qualche anno fa, ero una neo-laureata ansiosa di scoprire il mondo della ricerca che tanto avevo agognato negli anni di studio universitario. Mi presentai al mio tutor, il Dr. Luca De Stefano, dicendogli di voler imparare ogni cosa lui avesse da insegnarmi su questo "lavoro". Volevo fare quello per cui mi ero preparata e che avevo desiderato dal primo giorno di università. Luca mi ha dato l'opportunità che gli avevo chiesto. Mi ha spronato ogni giorno a superare quei limiti che io stessa credevo di avere. Quello che ho imparato in questi anni lo devo soprattutto a lui ed è per questo che lo ringrazio.

Ringrazio il direttore, il Dr. Ivo Rendina, per i preziosi spunti di riflessione che mi ha offerto, per i consigli e perché ha sempre cercato di garantire a me e agli altri aspiranti ricercatori del gruppo la migliore formazione possibile.

Ringrazio tutti gli altri ricercatori e colleghi dell'IMM, molti dei quali sono diventati amici, con cui ho avuto la fortuna di lavorare e dividere la passione per la ricerca. Conserverò un buon ricordo di questi anni anche perché ci siete stati voi.

Un ringraziamento va al coordinatore di dottorato, il Prof. Giancarlo Abbate, che mi ha seguito in questa importante fase di formazione e studio, proponendo corsi e seminari sempre aggiornati che mi hanno permesso di venire a contatto con nuove tematiche di ricerca che hanno suscitato in me grande curiosità ed interesse.

Ringrazio il gruppo del Prof. Paolo Arcari, del Dipartimento di Biochimica e Biotecnologie Mediche, ed il gruppo della Prof.ssa Paola Giardina, del Dipartimento di Chimica Organica e Biochimica, con cui si è sviluppata in questi anni una collaborazione scientifica basata su competenze e linguaggi diversi ma che ha portato al conseguimento di interessanti risultati, molti dei quali illustrati in questo lavoro di tesi.

Ringrazio la mia famiglia per avermi insegnato che nella vita è importante inseguire le proprie passioni. Ringrazio Mimmo che da anni mi è vicino, appoggiandomi e condividendo le mie scelte.

Ilaria Rea

ABSTRACT

This thesis summarizes a three years scientific research investigation on the design and fabrication of porous silicon based optical devices for applications in the field of biochemical sensing. Porous silicon is an ideal transducer material due to its sponge-like morphology, characterized by a specific surface area up to 500 m^2 cm^{-3}, which assures an effective interaction with gas and liquid substances. Moreover, porous silicon is a low cost material, completely compatible with standard microelectronic processes.

In this work, different porous silicon structures such as Fabry-Perot interferometer, Bragg mirror, optical microcavity, Thue-Morse sequences and optical waveguide have been realized and characterized as optical transducers for the monitoring of chemical and biological interactions. The selectivity, reversibility and sensitivity of these devices as optical sensors have been discussed.

The porous silicon surface has been modified in order to gain chemical stability, proper wettability, and specific features such as biomolecules immobilization. Standard chemical functionalizations, but also an innovative pure biological passivation method based on selfassembled biofilms of the *Hydrophobins* proteins, have been successfully experimented.

Some standard micromachining techniques, such as HF wet etching and anodic bonding, have been optimized to integrate the porous silicon sensing element into a Lab-on-Chip prototype. The integrated devices have been characterized as fast sensors of chemical compounds and response times shorter than 100 ms have been demonstrated. The Direct-Laser-Writing of the porous silicon surface, as alternative process to the photolithographic patterning in the device miniaturization has been also exploited.

Finally, a bottom-up approach in microoptics has been developed by using the silica shells of some marine *Diatoms*, microalgae which show impressive morphological and physical analogies with porous silicon.

LIST OF PUBBLICATIONS

The following papers have been published on the results described in this thesis.

Journals

J1. L. De Stefano, I. Rea, I. Rendina, L. Rotiroti, M. Rossi, S. D'Auria, "Resonant cavity enhanced optical microsensor for molecular interactions based on porous silicon", *Phys. Stat. Sol. (a)* **203**, 886-891 (2006).

J2. S. D'Auria, M. de Champdorè, V. Aurilia, A. Parracino, M. Staiano, A. Vitale, M. Rossi, I. Rea, L. Rotiroti, A. M. Rossi, S. Borini, I. Rendina. L. De Stefano, "Nanostructured silicon-based biosensors for the selective identification of analytes of social interest", *Journal of Physics: Condensed Matter* **18**, S2019-S2028 (2006).

J3. L. De Stefano, L. Rotiroti, I. Rea, L. Moretti, G. Di Francia, E. Massera, A. Lamberti, P. Arcari, C. Sanges, I. Rendina, "Porous silicon-based optical biochips", *Journal of Optics A: Pure and Applied Optics* **8**, S540-S544 (2006).

J4. L. De Stefano, K.Malecki, F. G. Della Corte, L. Moretti, I. Rea, L. Rotiroti, I. Rendina, "A Microsystem Based on Porous Silicon-Glass Anodic Bonding for Gas and Liquid Optical Sensing", *Sensors* **6**, 680-687 (2006).

J5. L. Moretti, I. Rea, L. Rotiroti, I. Rendina, G. Abbate, A. Marino, L. De Stefano, "Photonic band gaps analysis of Thue-Morse multilayers made of porous silicon", *Optics Express* **14**, 6264-6272 (2006).

J6. L. De Stefano, L. Rotiroti, I. Rea, M. Rossi, S. D'Auria, I. Rendina, "Assessment of a porous silicon transducer for the development of optical biochips", *Rivista di Materiali Nanocompositi e Nanotecnologie* **3**, 39-41 (2006).

J7. L. De Stefano, L. Rotiroti, I. Rea, L. Moretti, I. Rendina, "Quantitative measurements of hydro-alcoholic binary mixtures by porous silicon optical microsensors", *Phys. Stat. Sol. (c)* **4**, 1941-1945 (2007).

J8. L. De Stefano, I. Rea, L. Rotiroti, L. Moretti, I. Rendina, "Optical properties of porous silicon Thue-Morse structures", *Phys. Stat. Sol. (c)* **4**, 1966-1970 (2007).

J9. I. Rendina, I. Rea, L. Rotiroti, L. De Stefano, "Porous Silicon Based Optical Biosensors and Biochips", *Physica E* **380**, 188-192 (2007). **Invited Paper** at E-MRS 2006 Symposium C: Silicon Nanocrystals and Sensing Applications.

J10. L. De Stefano, I. Rea, L. Rotiroti, L. Fragomeni, F.G. Della Corte, I. Rendina, "An integrated hybrid optical device for sensing applications", *Phys. Stat. Sol. (c)* **4**, 1946-1950 (2007).

J11. L. De Stefano, D. Alfieri, I. Rea, L. Rotiroti, K. Malecki, L. Moretti, F. G. Della Corte, I. Rendina, "An integrated pressure-driven microsystem based on porous silicon for optical monitoring of gaseous and liquid substances", *Phys. Stat. Sol. (a)* **204**, 1459-1463 (2007).

J12. L. De Stefano, I. Rea, L. Rotiroti, M. Iodice, I. Rendina, "Optical microsystems based on a nanomaterial technology", *J. Phys.: Condens. Matter* **19**, 395008 (2007).

J13. L. De Stefano, P. Arcari, A. Lamberti, C. Sanchez, L. Rotiroti, I. Rea, I. Rendina, "DNA optical detection based on porous silicon technology: from biosensors to biochips", *Sensors* **7**, 214-221 (2007).

J14. L. Moretti, I. Rea, L. De Stefano, I. Rendina, "Periodic versus aperiodic: Enhancing the sensitivity of porous silicon based optical sensors", *Applied Physics Letters* **90**, 191112 (2007).

J15. L. De Stefano, I. Rea, A. Armenante, I. Rendina, P. Giardina, M. Giocondo, "Self-assembled biofilm of hydrophobins protect the silicon surface in the KOH wet etch process", *Langmuir* **23**, 7920-7922 (2007).

J16. L. De Stefano, I. Rea, I. Rendina, M. De Stefano, L. Moretti, "Lensless light focusing with the centric marine diatom Coscinodiscus walesii", *Optics Express* **15**, 18082-18088 (2007).

J17. L. De Stefano, A. Vitale, I. Rea, M. Staiano, L. Rotiroti, T. Labella, I. Rendina, V. Aurilia, M. Rossi, S. D'Auria, "Enzymes and proteins from extremophiles as hyperstable probes in nanotechnology: the use of D-trehalose/D-maltose-binding protein from the hyperthermophilic archaeon Thermococcus litoralis for sugars monitoring", *Extremophiles* **12**, 69-73 (2008).

J18. L. De Stefano, I. Rea, P. Giardina, A. Armenante, I. Rendina, "Protein Modified Porous Silicon Nanostructures", *Advanced Materials* **9999,** 1-5 (2008).

J19. L. De Stefano, I. Rea, M. A. Nigro, F. G. Della Corte, I. Rendina, "A parametric study of laser induced ablation-oxidation on porous silicon surfaces", *J. Phys.: Condens. Matter* **20**, 265009 (2008).

J20. L. De Stefano, E. De Tommasi, I. Rea, L. Rotiroti, L. Giangrande, G. Oliviero, N. Borbone, A. Galeone, G. Piccialli, "Oligonucleotides direct synthesis on porous silicon chip", *Nucleic Acids Symposium Series* **52**, 721-722 (2008).

J21. I. Rea, A. Marino, M. Iodice, G. Coppola, I. Rendina, L. De Stefano, "A Porous Silicon Bragg Grating Waveguide By Direct Laser Writing", *J. Phys.: Condens. Matter* **20**, 365203 (2008).

J22. I. Rea, M. Iodice, G. Coppola, I. Rendina, A. Marino, L. De Stefano, "A Porous Silicon based Bragg Grating Waveguide Sensor for Chemical Monitoring", accepted for publication on *Sensors and Actuators B: Chemical,* (2008).

J23. S. Houmadi, F. Ciuchi, M. De Santo, L. De Stefano, I. Rea, P. Giardina, A. Armenante, E. Lacaze, M. Giocondo, "Langmuir Blodgett film of hydrophobin protein from Pleurotus ostreatus at the air-water interface", *Langmuir* **24**, 12953-12957 (2008).

J24. E. De Tommasi, L. De Stefano, I. Rea, V. Di Sarno, L. Rotiroti, P. Arcari, A. Lamberti, C. Sanges, I. Rendina, "Porous Silicon Based Resonant Mirrors for Biochemical Sensing", *Sensors* **8**, 6549-6556 (2008).

J25. L. De Stefano, P. Maddalena, L. Moretti, I. Rea, I. Rendina, E. De Tommasi, V. Mocella, M. De Stefano, "Nano-biosilica from marine diatoms: a brand new material for photonic applications", accepted for publication on *Superlattices and Microstructures* (2008).

Proceedings

P1. L. De Stefano, L. Rotiroti, I. Rea, L. Moretti, I. Rendina, "Quantitative determinations in liquid and gaseous binary mixtures by porous silicon optical microsensors", Proceedings of First International Workshop on Advances in Sensors and Interfaces, p. 178-180, Aprile 19-20, 2005, Bari, Italia.

P2. L. De Stefano, M. De Stefano, I. Rea, L. Moretti, A. Bismuto, P. Maddalena, I. Rendina, “Optical characterization of biological nano-porous silica structures”, Proc. SPIE 5925, 59250S (2005).

P3. L. De Stefano, K. Malecki, F. Della Corte, L. Moretti, I. Rea, L. Rotiroti, I. Rendina, “Silicon/glass integrated optical sensor based on porous silicon for gas and liquid inspection”, Proceedings EUROSENSORS XIX, MC8, Settembre 11-14, 2005, Barcellona, Spagna.

P4. L. De Stefano, I. Rea, L. Rotiroti, L. Moretti, I. Rendina, “Optical properties of porous silicon Thue-Morse structures”, Extended Abstracts of 5th International Conference on Porous Semiconductuctors-Science and Technology, p. 73-74, Marzo 12-17, 2006, Sitges-Barcellona, Spagna.

P5. L. De Stefano, L. Rotiroti, I. Rea, F. Della Corte, D. Alfieri, L. Moretti, I. Rendina, “An integrated pressure-driven microsystem based on porous silicon for optical monitoring of gaseous and liquid substances”, Extended Abstracts of 5th International Conference on Porous Semiconductuctors-Science and Technology, p. 126-127, Marzo 12-17, 2006, Sitges-Barcellona, Spagna.

P6. L. De Stefano, L. Rotiroti, I. Rea, L. Moretti, I. Rendina, “Quantitative determinations in hydro-alcoholic binary mixtures by porous silicon optical microsensors”, Extended Abstracts of 5th International Conference on Porous Semiconductuctors-Science and Technology, p. 248-249, Marzo 12-17, 2006, Sitges-Barcellona, Spagna.

P7. L. De Stefano, I. Rea, L. Rotiroti, L. Fragomeni, F. Della Corte, I. Rendina, “An integrated hybrid optical device for sensing applications”, Extended Abstracts of 5th International Conference on Porous Semiconductuctors-Science and Technology, p. 250-251, Marzo 12-17, 2006, Sitges-Barcellona, Spagna.

P8. L. De Stefano, P. Maddalena, L. Moretti, I. Rea, I. Rendina, “Porous biosilica from marine diatoms: a new brand porous material for photonic applications”, Extended Abstracts of 5th International Conference on Porous Semiconductuctors-Science and Technology, p. 252-253, Marzo 12-17, 2006, Sitges-Barcellona, Spagna.

P9. L. De Stefano, I. Rea, L. Rotiroti, L. Moretti, I. Rendina, “Resonant photonic devices based on porous silicon: a perfect tool for optical sensing”, Proceedings of XX EUROSENSORS Conference, p. 294-295, Settembre 17-20, 2006, Göteborg, Svezia.

P10. L. De Stefano, L. Rotiroti, I. Rea, E. De Tommasi, A. Vitale, M. Rossi, I. Rendina, S. D'Auria, “Design and realization of highly stable porous silicon optical biosensor based on proteins from extremophiles”, Proc. SPIE 6585, 658517 (2007).

P11. L. De Stefano, L. Rotiroti, I. Rea, E. De Tommasi, M. A. Nigro, F. G. Della Corte, I. Rendina, “Laser oxidation micropatterning of a porous silicon based biosensor for multianalytes microarray”, Sensors and Microsystems, Proceedings of the 12th AISEM Conference, 382, A G Mignani et al. editor (2007).

P12. L. De Stefano, I. Rendina, I. Rea, L. Rotiroti, E. De Tommasi, G. Barillaro, “An optical microsystem based on vertical silicon-air Bragg mirror for liquid substances monitoring”, Proc. SPIE 6585, 65850N (2007).

P13. L. De Stefano, M. De Stefano, P. Maddalena, L. Moretti, I. Rea, V. Mocella, I. Rendina, “Playing with light in diatoms: small water organisms with a natural photonic crystal structure”, Proc. SPIE 6593, 659313 (2007). **Invited Paper** at Microtechnologies for the New Millennium 2007

P14. I. Rea, L. Moretti, L. Rotiroti, I. Rendina, L. De Stefano, "Aperiodic photonic bandgap devices based on nanostructured porous silicon", Proc. SPIE 6593, 65931A (2007).

P15. I. Rea, L. Rotiroti, L. Moretti, I. Rendina, L. De Stefano, "Multistrati aperiodici Thue-Morse realizzati con la tecnologia del silicio poroso", proc. FOTONICA 2007, Maggio 21-23, 2007, Mantova, Italia.

P16. I. Rendina, I. Rea, L. Rotiroti, E. De Tommasi, L. De Stefano, "Integrated optical biosensors and biochips based on porous silicon technology", Proc. SPIE 6898, 68981D (2008). **Invited Paper** at Silicon Photonics III (2008).

P17. I. Rendina E. De Tommasi, I. Rea, L. Rotiroti, L. De Stefano, "Porous silicon optical transducers offer versatile platforms for biosensors", SPIE Newsroom DOI: 10.1117/2.1200801.0982 (2008).

P18. E. De Tommasi, I. Rea, V. Di Sarno, I. Rendina, L. De Stefano, "Porous silicon resonant mirror biosensors", Extended Abstracts of 6th International Conference on Porous Semiconductuctors-Science and Technology, p. 352-353, Marzo 10-14, 2008, Mallorca, Spagna.

P19. L. De Stefano, I. Rea, P. Giardina, A. Armenante, I. Rendina, "Porous silicon devices modified by self-assembled molecular biofilm", Extended Abstracts of 6th International Conference on Porous Semiconductuctors-Science and Technology, p. 135-136, Marzo 10-14, 2008, Mallorca, Spagna.

P20. I Rea, M. Iodice, G. Coppola, I. Rendina, L De Stefano, "Direct laser writing of optical microsystems on porous silicon", Extended Abstracts of 6th International Conference on Porous Semiconductuctors-Science and Technology, p. 198-199, Marzo 10-14, 2008, Mallorca, Spagna.

P21. I. Rea, M. Iodice, G. Coppola, I. Rendina, E. De Tommasi, L. De Stefano, "Optical sensing of chemicals by a porous silicon Bragg grating waveguide", Proc. SPIE 7003, 70031E (2008).

P22. E. De Tommasi, L. De Stefano, I. Rea, L. Moretti, M. De Stefano, I. Rendina, "Light micro-lensing effect in biosilica shells of diatoms microalgae", Proc. SPIE 6992, 69920F (2008).

P23. L. Rotiroti, P. Arcari, A. Lamberti, C. Sanges, E. De Tommasi, I. Rea, I. Rendina, L. De Stefano, "Optical detection of PNA/DNA hybridization in resonant porous silicon-based devices", Proc. SPIE 6991, 699120 (2008).

TABLE OF CONTENTS

CHAPTER 1 INTRODUCTION

1.1 Optical Biochemical Sensors

Fast, simple and cheap sensing of chemical and biological molecules is of great significance for environmental monitoring, food safety, and diagnostic applications. In recent years, different sensor platforms with remarkable detection properties, based on potentiometric, amperometric, magnetic and optical transducers have been developed. Among others, photonic sensing devices offer specific features which make them very attractive when not unique. Optical measurements are not invasive and can be used in harsh environments: they do not require electrical contacts that can cause explosions or fire. Opto-instrumentation is immune to electromagnetic interferences so that they are highly requested for applications where electrical currents could be harmful such as *in vivo* monitoring inside a patient body. Moreover, optical sensors are generally characterized by very short time analysis, compared to other measurements methods, and high sensitivity. The optical detection principles are based either on fluorescence-labelled systems or on direct optical monitoring. Fluorescence detection has been the main approach in medical diagnostic, biotechnology and drug discovery for a long time. Recently, a new class of optical label-free sensors has been proposed, which uses direct optical methods (photoluminescence [1], surface plasmon resonance (SPR) [2, 3], reflectivity [4], interference [5]) and nonlabelled natural probes such as DNA sequences and proteins.

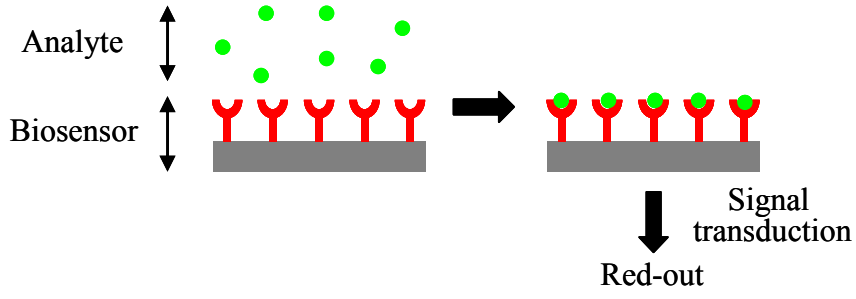

Figure 1.1. Scheme of the read-out method for a biosensor. The biosensor is constituted by a biological recognition element (specific to the target analyte) combinated with a physical transducer. The bio-recognition induces a change on the properties of the transducer, measurable in an event such as an electrical signal, an optical emission or a mechanical motion.

In this case the detection signal is directly originated from probe target binding that causes a change in the optical properties of the transducer. In Figure 1.1 a scheme of the read-out method for a label-free biosensor is reported. The quality of the sensors depends on the sensitive material, the read-out electronics and also the data elaboration software. All these functions determine the main features of the sensing platform, i. e. the selectivity, the sensitivity and the limit of detection.

1.2 Porous Silicon Optical Transducers

The porous silicon (PSi) is an ideal material as optical transducer due to its sponge-like morpholgy characterized by a specific surface area of about 500 m^2 cm^{-3} that assures an efficient and rapid interaction with the species to detect. It can be simply described as a network of air holes in a silicon matrix: the dielectric properties, and in particular the refractive index, of a PSi layer depend on the content of voids in the silicon and can be calculated by using an Effective Medium Approximation such as the Bruggemann model. Several good quality optical structures (Fabry Perot interferometer, Bragg mirror, optical microcavity, aperiodic multilayered sequences, optical waveguide) can be obtained by means the PSi technology. The fabrication process and the optical properties of these structures are described in the Chapter 2.

The main application of the PSi optical structures is in the field of the biochemical sensing. The sensing mechanism is based on the change of the PSi refractive index on exposure to the substances to be detected, due to their infiltration or capillary condensation in the pores; the consequence of the refractive index variation is a change in the reflectivity/transmittivity spectrum of the devices. The first measurement so far has been reported by Lin *et al*. who measured the shift of PSi Fabry-Perot fringes to detect the DNA hybridization [6]. Since then, there has been a rapid growth of research activities in this area. In Chapter 3 several experiments of biochemical sensing based on PSi optical structures are reported. A key step in the fabrication of the PSi biosensor is the functionalization of its surface in order to make this material compatible with the organic molecules which act as highly specific bioprobe for some target analytes. Different techniques of PSi surface chemical modification have been exploited. A different way to modify the surface properties of the PSi structures has been investigated in Chapter 4: a biological passivation with amphiphilic proteins has been used. This technique allows to control, in particular, the wettability of the material with very interesting implications in microfluidic systems.

1.3 Porous Silicon Micromachining

Another advange of the PSi is its complete compatibility with the standard integrated circuit fabrication process, circumstance which makes it an important material in microelectronics applications. It was for the first time investigated as insulating layer in 1969 by the Nippon Telegraph and Thelephone Public Corporation (NTT) [7] and the Sony Corporation [8]. Subsequently, it was widely exploited as sacrificial material in micromachining technology to realize, for example, suspended membranes [9] and cantilevers [10] on silicon substrate. In Figure 1.2 examples of free-standing Si microstructures realized by using PSi technology are shown. In Chapter 5 some techniques of PSi micromachining for its integration into a Lab-on-Chip are reported. In particular, the Direct-Laser-Writing process is exploited as alternative approach to the traditional photolithography, since standard masking material, typically a polymeric photoresist, withstands the PSi fabrication process for only few minutes.

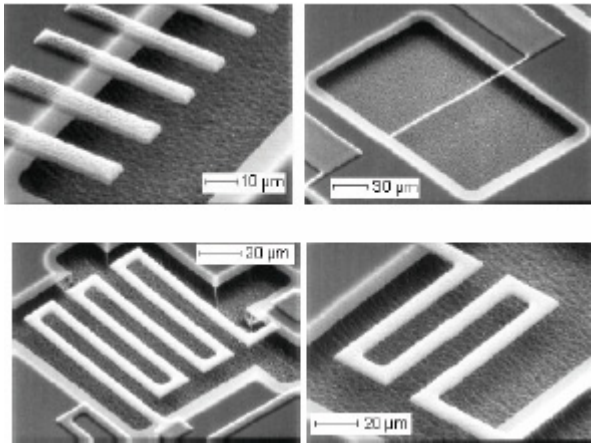

Figure 1.2. SEM images of free-standing structures realized by PSi technology [7].

1.4 Bioinspired Micro-optical Devices

The diatoms are unicellular microalgae made of amorphus silica. More than 100000 species of diatoms have been discovered and classified for the shape, morphology and size. One of the most interesting property of these natural structures is the morphological similarity with some man-made optical structures such as photonic crystals, realized by an expensive and complicated technological approach. In Figure

1.3, SEM images of a man-made PSi photonic crystal and a marine diatom are reported and compared; close analogies between the two structures can be easily recognized.

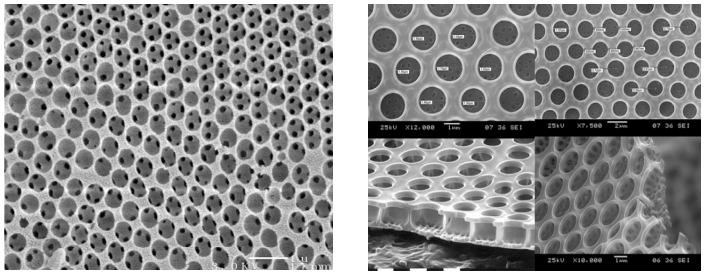

(a) (b)

Figure 1.3. Comparison between the SEM images of a man-made PSi photonic crystal (a) and a marine diatom (b).

The optical properties of the porous silica wall of a centric diatom, the *Coscinodiscus walesii*, are investigated in the Appendix.

Finally, the conclusions are presented in Chapter 6.

References

[1] S. Chan, S. R. Horner, P. M. Fauchet, B. L. Miller, "Identification of Crom Negative Bacteria using nanoscale silicon microcavities", *J. Am. Chem. Soc.* **123**, 11797-11798 (2001).

[2] J. Homola, J. Ctyroky, M. Skalsky, J. Hradilova, P. Kolarova, "A surface plasmon resonance based integrated optical sensor", *Sensors and Actuators B* **38-39**, 286-290 (1997).

[3] L. S. Jung, C. T. Campbell, T. M. Chinowsky, M. N. Mar, S. S. Yee, "Quantitative interpretation of the response of surface plasmon resonance sensors to adsorbed films", *Langmuir* **14**, 5636-5648 (1998).

[4] C. R. Mace, C. C. Striemer, B. L. Miller, "Theoretical and experimental analysis of arrayed imaging reflectometry as a sensitive proteomics technique", *Anal. Chem.* **78**, 5578-5583 (2006).

[5] A. Brandenburg, R. Henninger, "Integrated optical Young interferometer", *Applied Optics* **33**, 5941-5947 (1994).

[6] V. S. –Y. Lin, K. Motesharei, K. -P. S. Dancil, M. J. Sailor, M. R. Ghadiri, "A porous silicon based optical interferometric biosensor", *Science* **270**, 840 (1997).

[7] Japan Patent 49-19090 (1974); USA Patent 3-640-806 (1972).

[8] Japan Patent 49-19019 (1974).

[9] G. Kaltsas, A. G. Nassiopoulou, "Frontside bulk silicon micromachining using porous silicon technology", *Sensors and Actuators A* **65**, 175 (1998).

[10] S. Stolyarova, S. Chervan, R. Raiteri, J. Zeravik, P. Skladal, Y. Nemirovsky, "Composite porous silicon-crystalline silicon cantilevers for enhanced biosensing", *Sensors and Actuators B* **131**, 509-515 (2008).

CHAPTER 2 POROUS SILICON OPTICAL DEVICES

(Papers J5, J8, P4, P14, P15)

Porous silicon (PSi) is really a very versatile material due to its peculiar morphological, physical, and chemical properties: evidence of this is the huge number of papers about PSi features and devices based on this nanostructured material, costituted by voids into a silicon matrix, that appear in the literature every year. One reason for this clear success is the easy fabrication of sophisticated optical multilayers, such as one-dimensional photonic crystals, by a simple, but not trivial, computer-controlled electrochemical etching process.

2.1 Porous Silicon Fabrication by Electrochemical Etching

Porous silicon was discovered in 1956 by Uhlirs at Bell Labs, USA, during a study on the electropolishing of crystalline silicon in an HF-based solution. He observed the formation of a deposit "tentatively supposed to be a Si suboxide" [1]. The scientific community was not much interested in porous silicon until to 1990 when Leigh Canham, working at the Defence Research Energy in England, demonstrated an efficient tunable room temperature light output from the material [2]. In the years later, thousands of papers were published on porous silicon and its potential applications in microelectronics, optoelectronic devices, chemical and biological sensing. In most cases, the porous silicon structure is formed by electrochemical dissolution of crystalline silicon wafers in hydrofluoric acid (HF) based solution. The cell used for the electrochemical etching is shown in Figure 2.1. The silicon wafer is the anode; it is placed in back-side contact on an aluminum plate while the frontside is sealed with an O-ring and exposed to the anodising electrolyte. The chatode is made of platinum or any HF-resistant and conductive material. The electrolization cell is made of a highly-acid resistant polymer such as polyvinylidene fluoride (PVDF) or polytetrafluoroethylene (PTFE). For highly resistive silicon substrate (> few mΩ/cm) an evaporated metal backside contact is necessary to ensure the Schottky contact between the aluminum plate and the semiconductor.

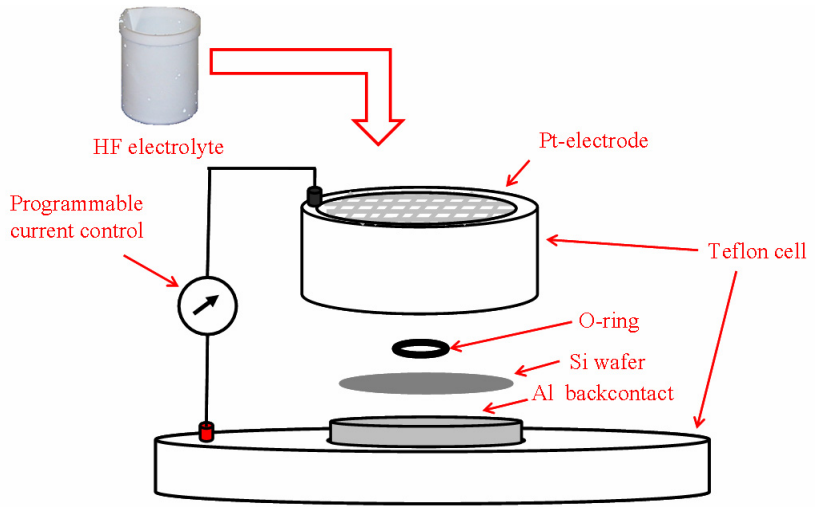

Figure 2.1. Electrochemical etching setup

Figure 2.2 shows the tipical I-V curves for *n*- and *p*-type silicon in aqueous HF in dark and under illumination [3]. The I-V curves show some basic similarities to the normal Schottky diode behavior expected from a semiconductor/electrolyte interface, including photogenerated currents at reverse bias, but there are some important anomalies. The I-V curves can be divided into four distinct regions depending on the sign of the applied potential and whether *n*- or *p*-type material is used. When a potential is applied to silicon in an aqueous environment, a measurable external current is induced to flow through the system.

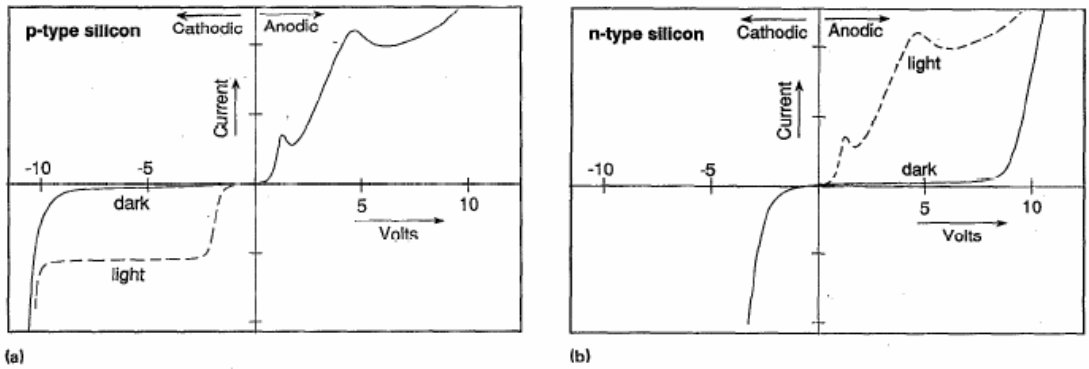

Figure 2.2. Tipical I-V curves for n- and p-type silicon. The solid line is the dark response while the dashed line is the response under illumination [3].

However, for any current to pass the silicon/electrolyte interface it must first change from electronic to ionic charge carriers. This conversion is always accomplished by means of a specific chemical redox reaction at the silicon interface. Application of a

potential then induces a precise interfacial reaction, the nature of which is fundamental to the formation of porous silicon. Under cathodic polarizations for both *n*- and *p*-type material, silicon is normally stable, i.e., silicon does not dissolve.

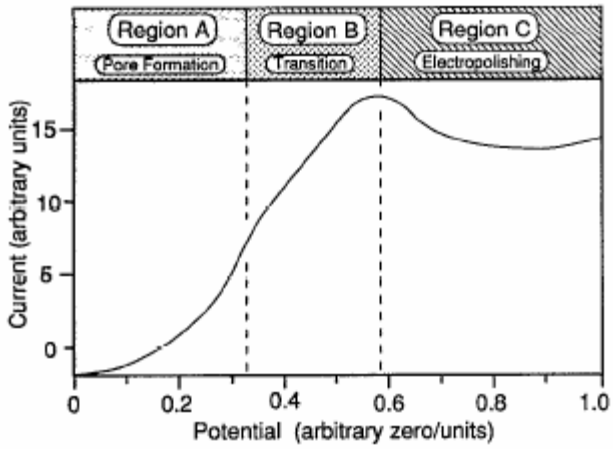

Figure 2.3. Anodic I-V curve for silicon in HF. In the region A pore formation occurs. In region C there is the silicon electropolishing. The region B is a transition zone where pore formation and electropolishing compete [3].

The only important cathodic charge transfer reaction in the silicon/HF system is the reduction of water with the subsequent liberation of hydrogen gas. It is only under anodic polarizations that silicon dissolution occurs. Figure 2.3 shows the anodic dissolution portion of a "typical" silicon I-V curve where the different dissolution regions are labeled A-C. Pore formation takes place in region A. At anodic overpotentials in excess of the current "peak," region C, silicon electropolishes. At intermediate overpotentials, region B, a "transition" zone exists where pore formation and electropolishing compete for control over the surface morphology. The resulting structure within this region is generally porous in nature but the pore diameters increase rapidly as the electropolishing potential is approached.

The exact dissolution chemistries of silicon are still in question, although it is generally accepted that holes are required in the initial steps for both electropolishing and pore formation. The Figure 2.4 illustrates the chemical dissolution mechanism suggested by Lehmann and Gösele [4], that has received great attention. If a hole of the silicon substrate has the sufficient energy to reach the surface, a nucleophilic attack on Si-H bond by fluoride ion can occur and a Si-F bond is formed (step 1 in Figure 2.4).

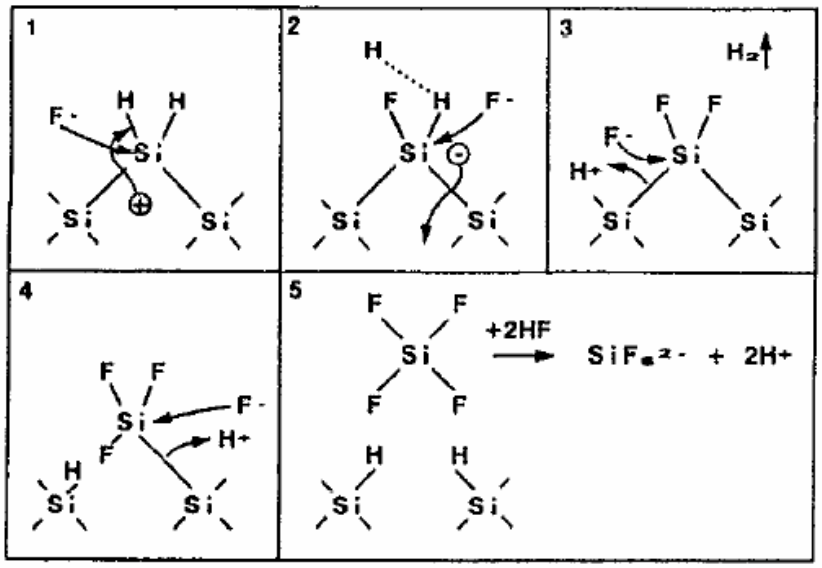

Figure 2.4. Dissolution mechanism of silicon in hydrofluoridric acid (HF) [4].

Due to the polarizing influence of the Si-F bond, another F^- ion can attack and bond under generation of an H_2 molecule and injection of one electron into the substrate (steps 2 and 3). The polarization induced by the Si-F groups reduces the electron density of the Si-Si backbonds; these weakened bonds will now be attacked by HF or H_2O (step 4) in a way that the silicon surface atoms remain bonded to hydrogen atoms (step 5). The silicon tetrafluoride molecule reacts with the HF to form the highly stable H_2SiF_6.

In the case of *n*-type silicon, where holes are minority carriers, the electrochemical dissolution of the material strongly depends on the hole/electron pair generation by illumination. In fact, when lightly doped (majority carrier concentration below ~10^{18} cm^{-3}) *n*-type silicon is anodised in the dark, the formation of PSi is observed only at high voltages (>5 V). If the anodisation is perform under illumination, PSi is formed at lower potentials (<1 V).

2.2 Porous Silicon Morphology

The PSi is a versatile material that shows a great variety of morphologies dependent on the doping type and level of the silicon substrate and the electrochemical etching parameters. Usually for a given substrate and electrolyte, only one type of pore structure can be obtained.

The IUPAC (International Union of Pure and Applied Chemistry) guidelines define ranges of pore sizes that exhibit characteristic absorption properties [5]: pores

characterized by a diameter ≤ 2nm define microporous silicon; for sizes in the range 2-50 nm the PSi is mesoporous; pores diameters > 50 nm are typical of macroporous silicon.

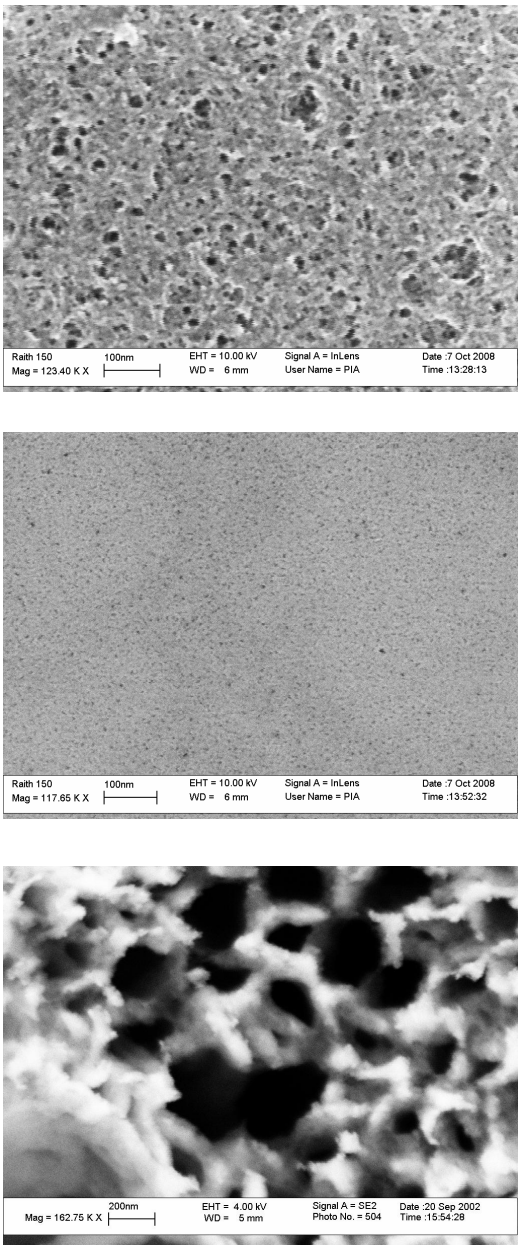

Figure 2.5. SEM images illustrating different PSi morphologies. A) p^+ <100> silicon; the pores have an average width of 30 nm. B) p <100> silicon; the pores size is about 2 nm. C) n <100> silicon; the material consists of two parts, micro an macropores are found.

Highly doped (10^{19} cm^{-3}) *p*- or *n*- silicon anodized in aqueous HF solution usually forms mesoporos with pore sizes from 20 nm to 50 nm (Figure 2.5 (a)). Several groups have

demonstrated that complex optical devices can be designed with mesoporous silicon [6]. In the case of lightly doped (below ~10^{18} cm^{-3}) *p*-type silicon, the porous size distribution is normally found in the range 1 – 5 nm, in the lower limit for mesopores (Figure 2.5 (b)). The influence of the HF concentration has been studied [7]: it is found that the pore size distribution broadens and the mean pore radius increases when the HF concentration in the etching solution is decreased from 55 to 37 %, but no significant changes are observed for lower HF concentrations. The electrochemical etching of lightly doped *n*-type substrates in the dark results in the formation of a macroporous material with radii in the micrometer range. Under sample illumination mesopores and/or micropores are formed, whereas macropores are still found (Figure 2.5 (c)).

2.3 Porosity and Refractive Index Determination

The most important parameter of the PSi is the porosity, defined as the fraction of void within the porous layer. The easiest way to determine the porosity is by weight measurements. The wafer is weighed before the anodic reaction (m_1), after the anodic reaction (m_2) and finally after dissolution of the porous material in a molar NaOH aqueous solution (m_3). The porosity is given by the equation:

$$P = \frac{m_1 - m_2}{m_1 - m_3} \tag{2.1}$$

After the removal of the porous layer, it is also possible to determine its thickness by profilometric analysis. Another interesting technique, that allows to determine simultaneously both the thickness and the porosity of a PSi layer without destroying the material is the spectroscopic ellipsometry (SE) [8]. The method is based on the measurement of the change in the polarization state of the light over the spectral range after the reflection from the sample surface. Ellipsometry measures the complex reflectance ratio (ρ) defined by:

$$\rho = \frac{R_p}{R_s} = \tan\psi e^{i\Delta} \tag{2.2}$$

where R_p and R_s are the complex reflection coefficients of the light polarized parallel and perpendicular to the plane of incidence. Thus, ψ and Δ are, respectively, the amplitude ratio and the phase shift between *s* and *p* components of polarized light. From experimentally determined ρ, it is possible to obtain informations about the properties of the material by performing proper model calculations. The use of SE in the near IR-UV spectral range for studying PSi has been largely reported in literature [9, 10]. The PSi

can be modeled using a sequence of sublayers, each one constituted by air and crystalline silicon, in order to take into account the inhomogeneity along the layer normal [11] and adopting the Bruggeman effective medium approximation (EMA) [12] given in the Eq. 2.3

$$(1-P)\left(\frac{\varepsilon_{Si}-\varepsilon_{PSi}}{\varepsilon_{Si}+2\varepsilon_{PSi}}\right)+P\left(\frac{\varepsilon_{void}-\varepsilon_{PSi}}{\varepsilon_{void}+2\varepsilon_{PSi}}\right)=0 \qquad (2.3)$$

where P, ε_{si}, ε_{PSi}, *and* ε_{void} are the layer porosity, the dielectric constants of silicon, porous silicon and void, respectively. This approximation is acceptable because the size of the PSi pores is much smaller than the wavelengths of incidence light in the near IR-UV regions; in this range, the electromagnetic radiation does not distinguish between silicon and void, and it is possible to treat the PSi as a homogeneous medium. The root square of the dielectric constant is the complex refractive index, $\bar{n} = n + ik$. The Figure 2.6 shows the dependence of the real part of the complex refractive index of the PSi on porosity given by the Bruggeman model.

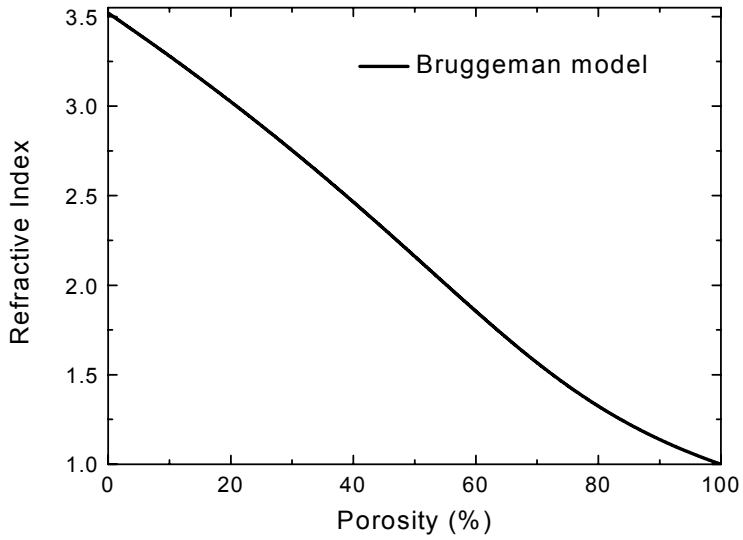

Figure 2.6. Dependence of real part of the PSi refractive index (real part) on the porosity given by the Bruggeman effective medium approximation.

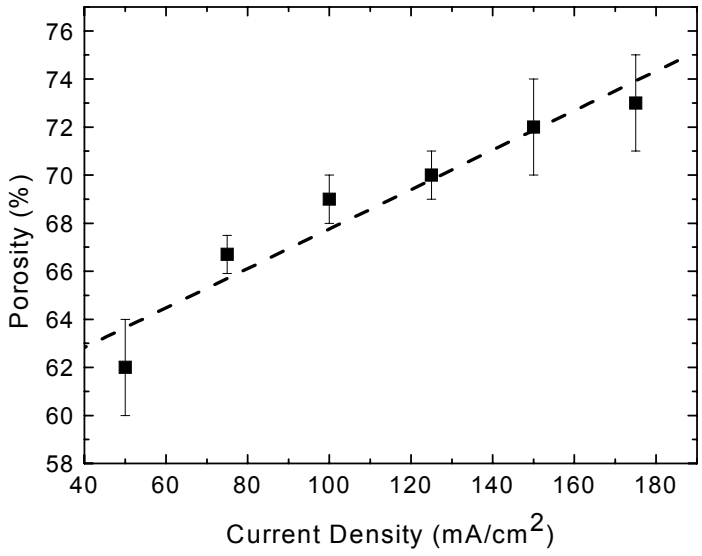

Figure 2.7. Dependence of the porosity on the current density for p^+ <100> silicon using a solution of 15% hydrofluoric acid in ethanol.

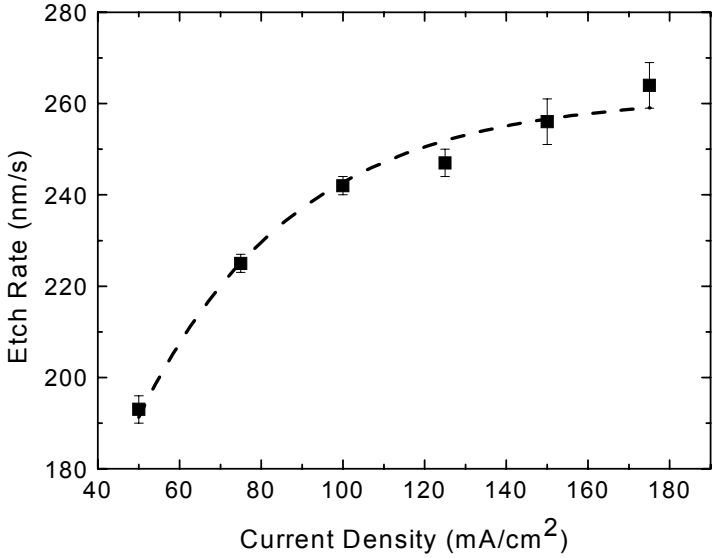

Figure 2.8. Dependence of the etch rate on the current density for p^+ <100> silicon using a solution of 15% hydrofluoric acid in ethanol.

In this work, highly doped p^+-silicon, <100> oriented, 0.01 Ω·cm resistivity, 400 μm thick was used as substrate in the PSi structures fabrication. The electrochemical etching of crystalline silicon was performed in dark and at room temperature using a solution of 15% hydrofluoric acid in ethanol. This electrolyte concentration has been

chosen because it allows the fabrication of PSi with porosities in a large range. Several PSi samples have been realized so to determine the dependence of the porosity and the etch rate of a layer on the etching current density. In Figure 2.7 and 2.8 are reported the porosity and the etch rate as function of the current density, respectively. The values have been estimated by variable angle spectroscopic ellipsometry (UVISEL, Horiba, Jobin–Yvon). The SE spectra were recorded at three angles of incidence, 60, 65 and 70° in the wavelengths range 260-1600 nm with a step of 5 nm.

2.4 Thermal Oxidation of Porous Silicon

The PSi is a material characterized by a high chemical reactivity; if stored in ambient air, the texture becomes partially oxidized and both the refractive index and the extinction coefficient change. To stabilize the PSi and to eliminate the problem of aging, the thermal oxidation of the structure is used. Usually, this treatment is also applied to PSi waveguides to extend the analysis range into the visible spectrum [13]. The oxidation reduces or completely removes the Si from the skeleton substituting it with SiO_2, that isotropically grows also into the pores. The Figure 2.9 shows the SEM images of PSi layer (a) and oxidized PSi layer (b).

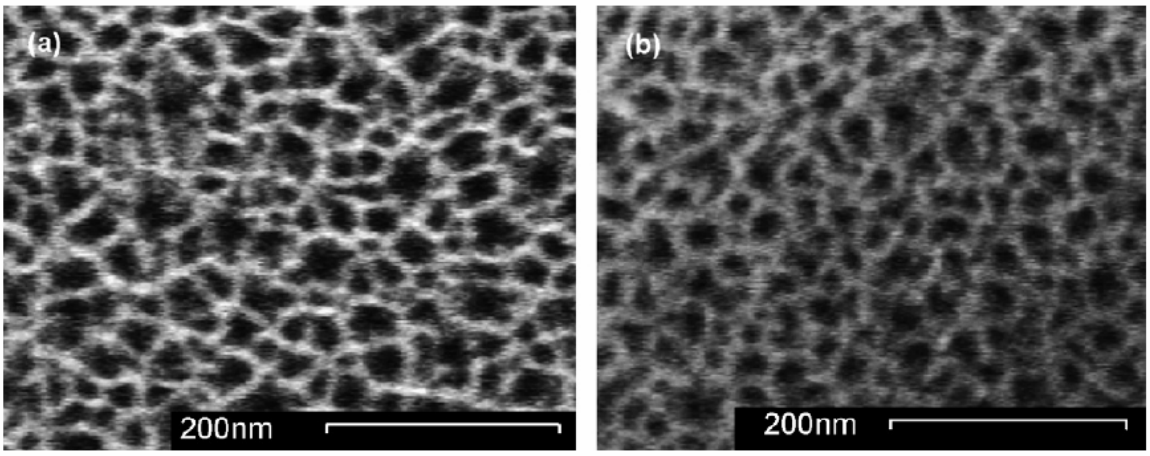

Figure 2.9. SEM images of p^+ PSi layer (a) and p^+ PSi layer pre-oxidized at 300°C for one hour following by an oxidation step at 900 °C in wet O_2 for 1 hour (b) [14].

It is possible to observe that after the oxidation the pore shape is conserved but the size is reduced. In particular, the mean value of the pores width from 18 nm becomes 13 nm. Since the pores density is the same and the pore size decreased, the porosity after oxidation is lower than the porosity before oxidation [14]. The relationship between the

porosities of a PSi layer before and after the thermal oxidation is expressed by the equation:

$$(1-P_{ox}) = (1+1.27x)(1-P) \tag{2.4}$$

where P is the porosity before oxidation, P_{ox} the porosity after the oxidation and x is the oxidation extent which is a function of the temperature T and the duration t of the process:

$$x(T,t) = 0.44\left(\frac{SiO_{2\,final}}{Si_{initial}}\right) \tag{2.5}$$

PSi is generally oxidized in a pure O_2 atmosphere by a two step thermal treatment. The first oxidation step, defined as pre-oxidation, at low temperature (300 - 400 °C) is required in order to selectively oxidise the silicon backbonds thus assuring an easy propagation of the oxidant into the silicon structure [15]. Moreover, the pre-oxidation reduces the damage of the material texture in the second oxidation step at higher temperatures between 800 and 900 °C [16].

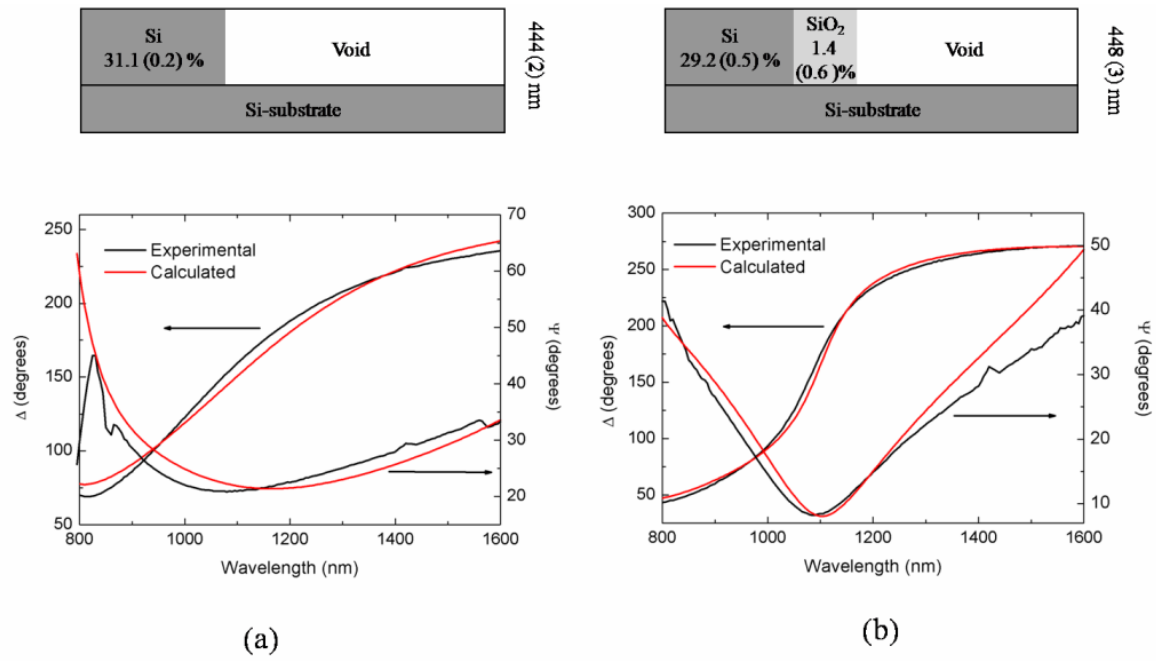

Figure 2.10. Schematic diagram of the model layer used in the ellipsometric analysis and calculated ψ, Δ spectra compared with the experimental ones before (a) and after (b) the pre-oxidation at 400° C for 30 min of the p^+ PSi layer.

A p^+ PSi layer pre-oxidised at 400° C for 30 min has been characterized by spectroscopic ellipsometry before and after the thermal process. In Figure 2.10 are

reported the schematic diagrams of the models used in the analysis and the calculated ψ and Δ spectra compared with the experimental ones before (a) and after (b) the pre-oxidation of the material. The value of the variable x has been estimated to be about 0.02; the oxidation interests only the surface of the material. A short (3-5 min) thermal treatment at 900°C completely oxidized the structure; in this case x=1 and the Eq. 2.4 becomes $(1-P_{ox}) = 2.27(1-P)$.

2.5 Porous Silicon Photonic Structures

In the last few years, PSi resonant photonic structures as Fabry-Perot interferometers [17], Bragg reflectors [18], optical microcavities [6, 19], Thue-Morse sequences and optical waveguides [20] have been intensively studied by several research groups in particular for their photonic properties as interference filters.

The refractive index profile of a PSi multilayered structure can be realized by choosing the proper current density profile during the electrochemical etching of crystalline silicon. This is possible because the PSi fabrication process is self-stopping, the already formed PSi layer is depleted of holes and any further etching only occurs at the pores tips [21]. In this section the PSi optical structures, fabricated for experimental purposes, are described.

2.5.1 Fabry Perot Interferometer

A single layer of PSi optically acts as a Fabry-Perot interferometer. In Figure 2.11 the reflectivity spectrum of a PSi layer under white light illumination is reported. The maxima in the reflectivity spectrum appear at wavelengths λ_m which satisfy:

$$m = 2nd / \lambda_m \qquad (2.6)$$

where m is an integer, d is the film thickness and n is the average refractive index of the layer [22, 23]. Assuming that the refractive index is independent on the wavelength over the considered range, the maxima are equally spaced in the wavenumber ($1/\lambda_m$). When m maxima are plotted as a function of the wavenumber, each point lies on a straight line which slope is two times the optical path of the interferometer, as it is shown in the Figure 2.12

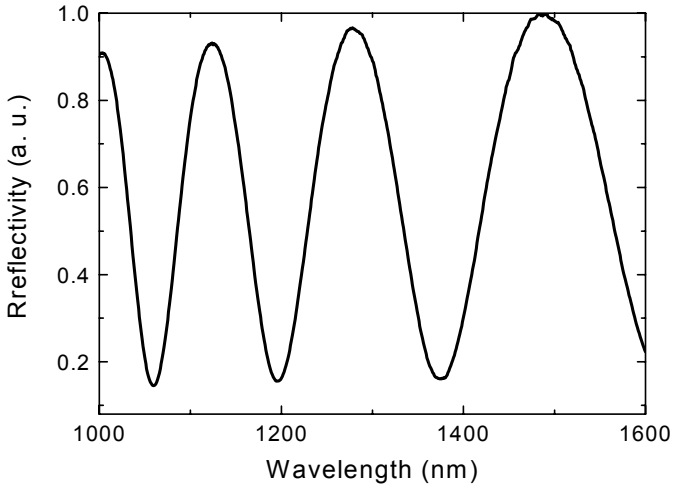

Figure 2.11. Reflectivity spectrum of a PSi layer realized by the electrochemical etching of p^+ crystalline silicon in a solution of 15 % hydrofluoric acid applying a current density of 115 mA/cm^2 for 11 s (P=69 %; n=1.593 @1.2 μm; d=2.9 μm).

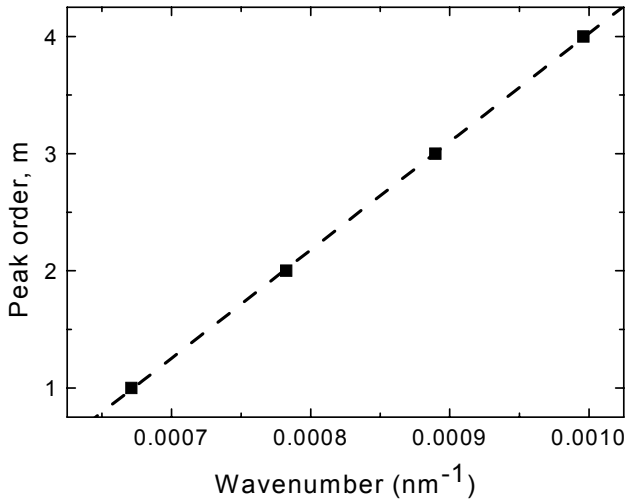

Figure 2.12. m-order peaks are plotted as function of the wavenumber. The optical path of the interferometer has been estimated to be (4620±40) nm.

2.5.2 Bragg Mirror and Optical Microcavity

The Bragg mirror is a periodic structure made alternating layers of high (n_H) and low (n_L) refractive index, whose thicknesses satisfy the relation $2(n_H\, d_H + n_L\, d_L) = m\lambda_B$, where m is the order of the Bragg condition (Figure 2.13 (a)). The layer stack is usually

denoted as $[HL]^N$, where N is the number of periods. The periodicity gives to the structure a photonic band gap (PBG) behavior characterized by the property to forbid the propagation of the light at fixed wavelengths. The reflectivity spectrum of a Bragg mirror is characterized by the presence of a stop band centered around the Bragg wavelength λ_B (Figure 2.13 (b)). For a given number of periods, the height and width of the reflectivity stop band increases by increasing the index ratio H/L. A low index contranst can be compensated by a higher number of periods.

An optical microcavity is a $\lambda/2$ layer sandwiched between two distributed Bragg mirrors (Figure 2.14 (a)). The reflectivity spectrum of a microcavity is characterized by a transmittance peak in the photonic stop band (Figure 2.14 (b)). The Q factor of the microcavity is defined as $Q=\lambda/\Delta\lambda$, where λ is the wavelength of the resonance peak and $\Delta\lambda$ is the full width half maximum (FWHM) of the resonance. This parameter is used to evaluate how the light is confined in the PBG structure.

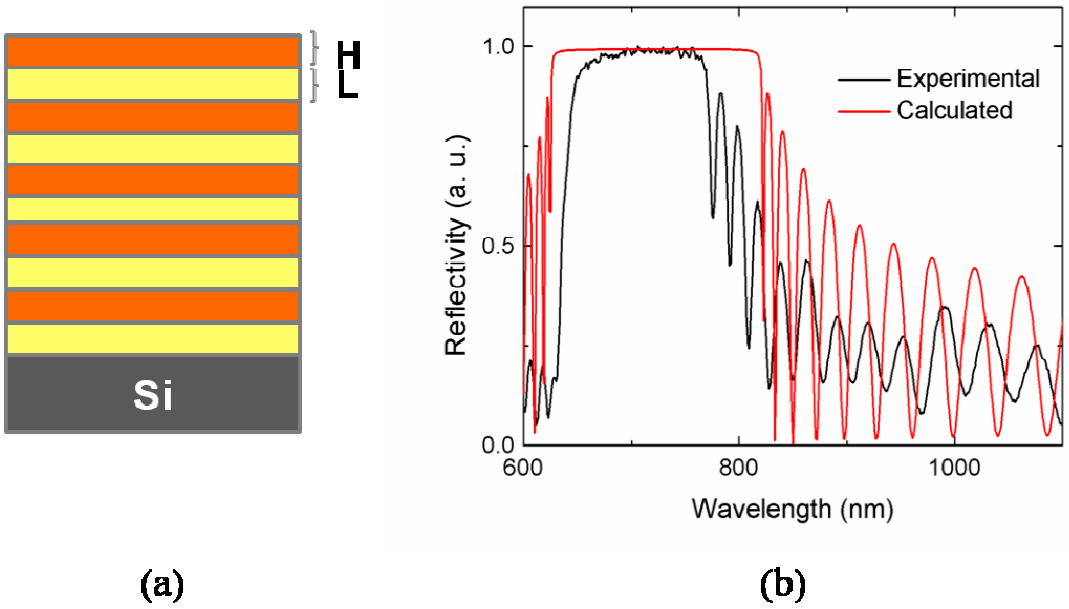

Figure 2.13. (a) Schematic of a Bragg mirror. (b) Experimental normal incidence reflectivity spectrum from a Bragg mirror (black line) compared with the calculated one (red line).

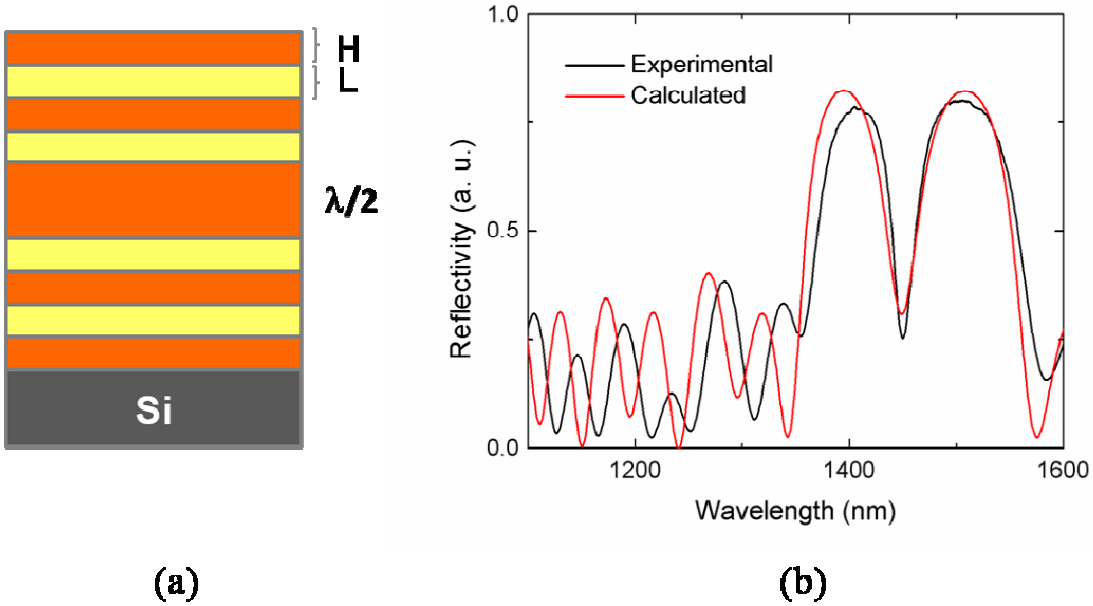

Figure 2.14. (a) Schematic of an optical microcavity. (b) Experimental normal incidence reflectivity spectrum of a microcavity (black line) compared with the calculated one (red line).

The calculated reflectivity spectra of the structures reported in Figure 2.13 e 2.14 have been reproduced by a transfer matrix method [24], also taking into account the wavelength dispersion of silicon.

2.5.3 Thue-Morse Sequence

A quasi-crystal (QC) does not have a geometrical periodicity but is still deterministically generated. Even if these structures do not have a translational symmetry, they show several interesting physical properties such as the photonic band gaps, some resonance frequencies, and some high localized states [25]. Thue-Morse (T-M) [26] sequence is one of the most common examples of one dimensional QC. The T-M one dimensional structure is constituted by the sequence of two layers A and B with refractive index n_A (n_B) and thickness d_A (d_B). Applying the substitution rules A→AB and B→BA [26] all subsequent orders can be deduced, as follow: S_0=A, S_1=AB, S_2=ABBA, S_3=ABBABAAB, S_4=ABBABAABBAABABBA, and so on.

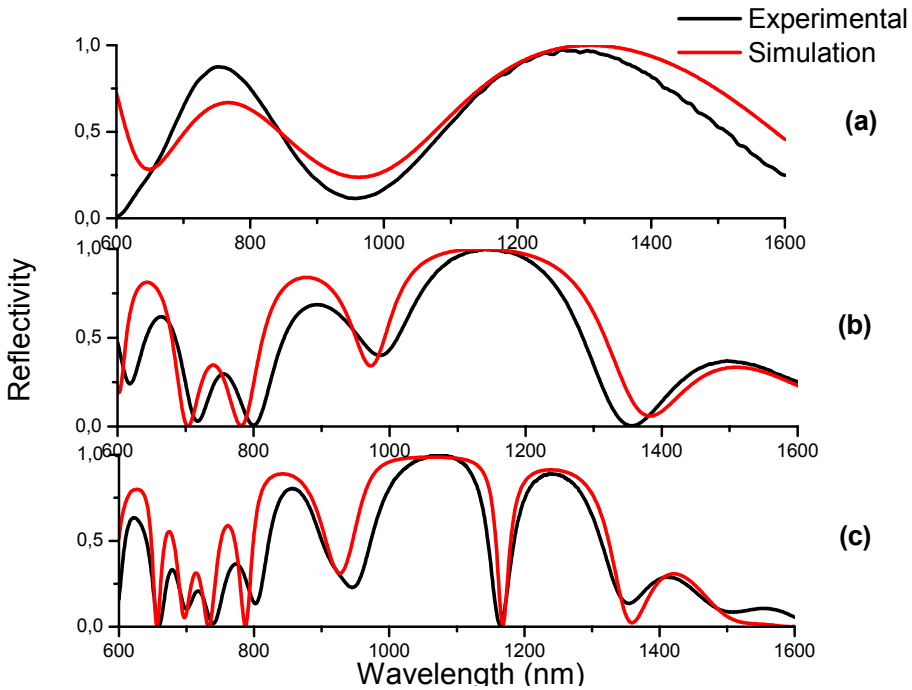

Figure 2.15. Experimental (black line) and calculate (red line) reflectivity for S_3 T-M structure (a), S_4 T-M structure (b) and S_5 T-M structure (c). The measurements have been taken at normal incidence.

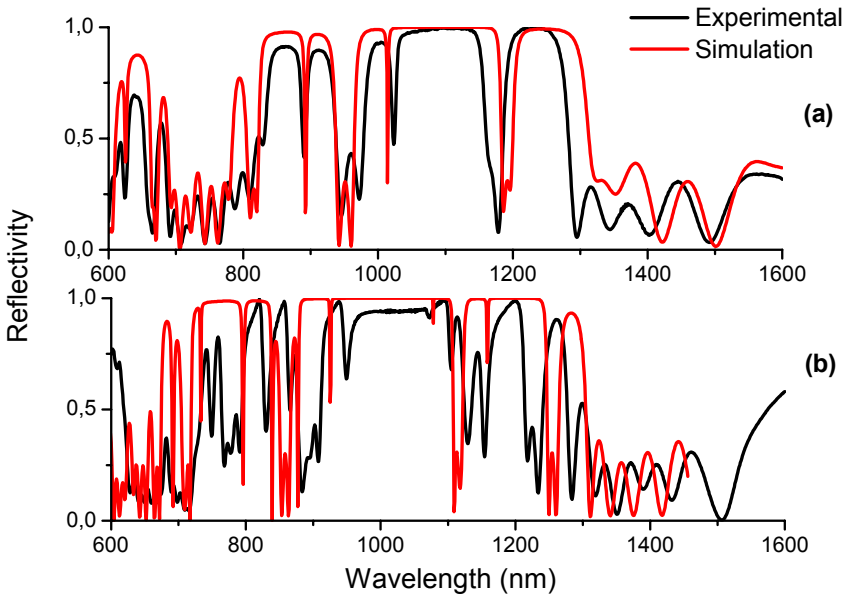

Figure 2.16. Experimental (black line) and calculate (red line) reflectivity for S_6 T-M structure (a) and S_7 T-M structure (b). The measurements have been taken at normal incidence.

The layers number of S_N is 2N, where N is the T-M order. Dielectric T-M structures up to 128 layers have been fabricated by using PSi technology. The high porosity layers are

characterized by a porosity p_A=81%, with an average refractive index n_A≅1.3 and a thickness d_A≅135 nm.

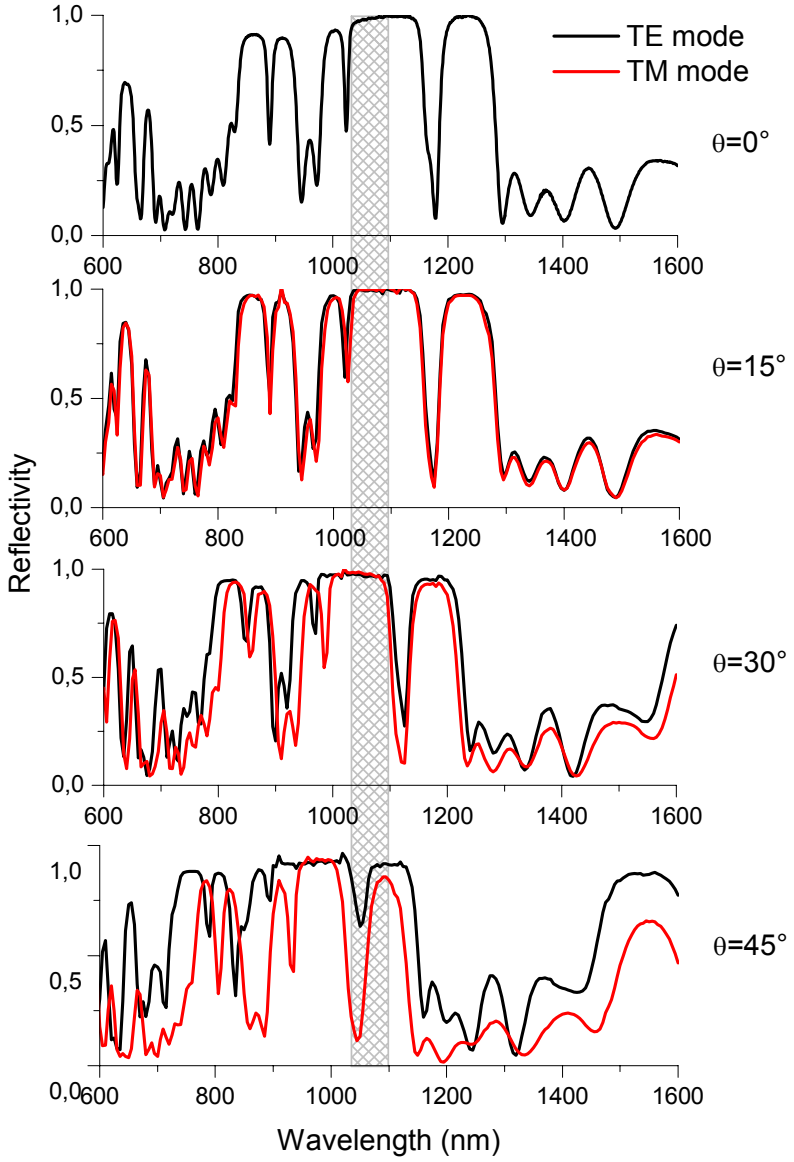

Figure 2.17. Experimental reflectivity spectra of S6 T-M structure for the transverse electric (TE) mode (black line) and the transverse magnetic (TM) mode (red line) for different incident angles.

The low porosity layers are characterized by a porosity p_B=56%, with a effective refractive index n_B≅1.96 and a thickness d_B≅90 nm. The thickness d_i of each layer was designed to satisfy the Bragg condition $n_i d_i = \lambda_0/4$ where n_i is the average refractive index and λ_0=700 nm. In Figures 2.15 e 2.16 the experimental (black line) and calculated (red line) reflectivity spectra are shown in case of S_3 (2.15-a), S_4 (2.15-b), S_5

(2.15-c), S_6 (2.16-a), and S_7 (2.16-b) T-M structures. The good control in the fabrication process of the devices is demonstrated by the agreement between the measured and calculated spectra. The not perfect matching can be ascribed to non-uniformities of thickness and porosities of layers along the etching direction. The spectrum of the S_3 T-M multilayer is characterized by two band gaps separated by a large transmission peak at 1000 nm. On increasing the order of T-M sequence, the PBG splits and very narrow transmission peaks appear (FWHM about 6 nm). The Figure 2.17 reports the experimental reflectivity spectra of the S_6 T-M structure for both the TE (black line) and the TM (red line) polarization for different incident angles up to 30°. The grey area highlights a PBG region of 70 nm, centered at 1100 nm which exists in the incident angle range between -30° and 30°.

2.5.4 Optical Waveguide

An optical waveguide is a structure used to confine and guide the light by total internal relection. The simplest waveguide is the planar slab guide shown in Figure 2.18 consisting of three media with refractive indices $n_1 < n_2 > n_3$ and a waveguide layer thickness d. Light propagation along z-axis and electromagnetic field distribution independent of y coordinate are assumed. Solution of Maxwell's equations for this structure can be assumed in the form:

$$\vec{U}(x,z) = \vec{u}(x)\exp(i(\omega t - \beta z)) \qquad (2.7)$$

where $\vec{U}(x,z)$ denotes the vector of electromagnetic field intensity, $\vec{u}(x)$ field amplitude, ω angular frequency, t time, and β propagation constant.

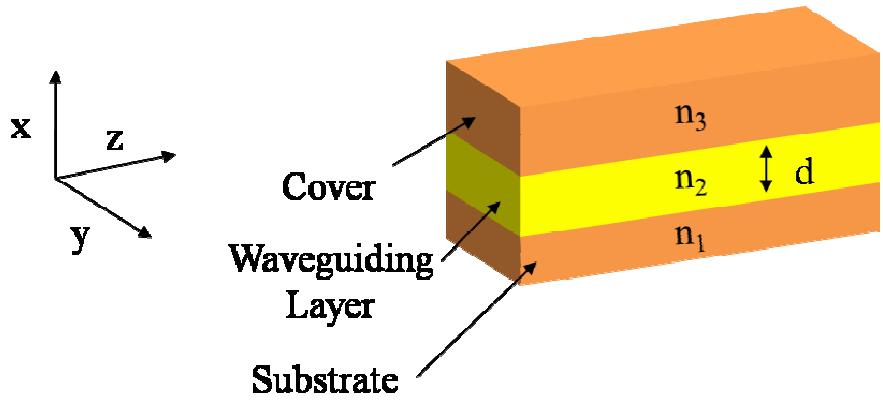

Figure 2.18. Planar optical waveguide

The solution can be decomposed into two types of waves – transverse electric (TE) modes $E_z=0$ and transverse magnetic (TM) modes $H_z=0$. For these waves, the wave equations can be written as:

$$\frac{\delta^2 U_y(x)}{\delta x^2} + (\omega^2 \varepsilon\mu - \beta^2) U_y(x) = 0 \qquad (2.8)$$

where U_y denotes the y-component of the vector of electric (for TE modes) or magnetic (for TM modes) field intensity. In each medium the solution of wave equation can be expressed as a linear combination of $exp(ik_ix)$ and $exp(-ik_ix)$, where $k_i^2=\omega^2\mu\varepsilon_i-\beta$ and ε_i are dielectric constants of the involved media (i=1, 2, 3).

In order to describe a light wave confined in the waveguide, parameters k_1 e k_2 must fulfill the condition $k^2<0$ and the electromagnetic field exponentially decreases outside the waveguide. Continuity of tangential components of electric and magnetic field vectors yields to dispersion equations in the form:

TE modes: $$\tan(kd) = \frac{\gamma_1/k + \gamma_3/k}{1-(\gamma_1/k)(\gamma_3/k)} \quad , \qquad (2.9)$$

TM modes: $$\tan(kd) = \frac{\gamma_1\varepsilon_2/k\varepsilon_1 + \gamma_3\varepsilon_2/k\varepsilon_3}{1-(\gamma_1\varepsilon_2/k\varepsilon_1)(\gamma_3\varepsilon_2/k\varepsilon_3)} \qquad (2.10)$$

where $k_2^2=\omega^2\mu\varepsilon_2-\beta$ and $\gamma_{1,3}^2=\beta-\omega^2\mu\varepsilon_{1,3}$. The solutions of these equation are the propagation constants of the guided modes. Dependence of the propagation constant of the first three TE and TM modes as a function of the normalized frequency, $V = kd\sqrt{n_2^2 - n_1^2}$ is shown in Figure 2.19. A PSi slab waveguide was realized with a core layer of thickness 2.5 μm and porosity 65 %, and a cladding layer with thickness 2.5 μm and porosity 78 %. These porosities correspond to a core and cladding refractive indexes of 1.65 and 1.52, respectively, calculated by the Bruggeman model [12] at a wavelength of 1.5 μm. The device was then fully oxidized in pure O_2 by a two step thermal treatment (400 °C for 30 min and 900 °C for 15 min). The core and cladding refractive indices of the oxidized PSi waveguide were measured by the standard m-line technique [28] at 1.55 μm in TE polarization. A value of 1.361±0.001 for the core refractive index and of 1.18±0.01 for the cladding was obtained. From these values, the effective refractive indices $n_{eff,m}$ of the fundamental (m=0) and first mode (m=1), supported by the slab waveguide, were estimated to be 1.341 and 1.282, respectively [29].

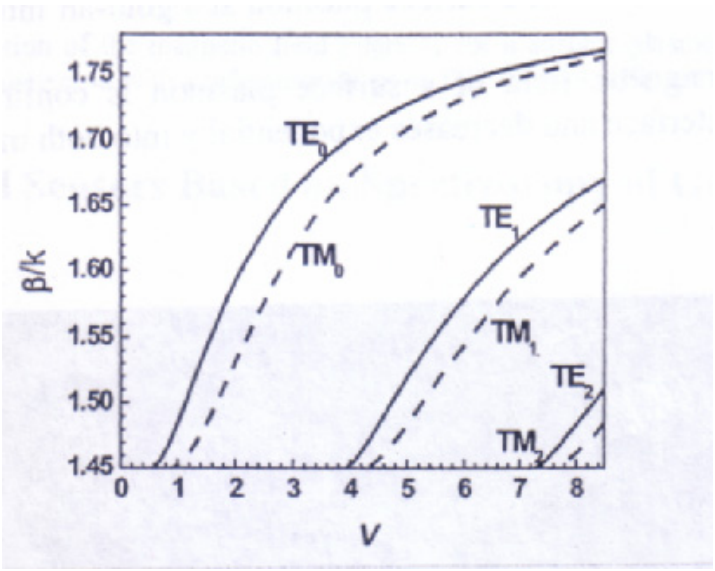

Figure 2.19. Normalized propagation constant as a function of normalized frequency for three low-order TE and TM modes; n_1=1.45, n_2=1.8 , n_3= 1.32 [27].

The PSi waveguide optical losses were characterized by measuring the light scattered from the top surface. In fact, assuming a constant scattering mechanism along the structure, the scattered intensity in the vertical direction is proportional to the intensity of the guided light [30].

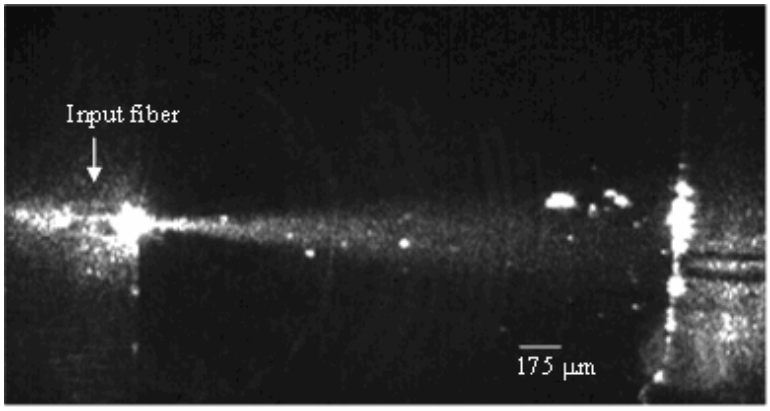

Figure 2.20. Top view of the scattered light from the surface of the oxidized PSi waveguide at 1.55 μm.

To this aim, a laser beam at 1.55 μm was coupled into the waveguide by a single mode lensed fiber and the upper out-of-plane scattered light intensity was recorded by an infrared CCD camera (Xenics Xeva) placed above the structure. The Figure 2.20 shows a top view image of the scattered light from the device registered by an infrared camera:

it is very clear that the beam diverges and its intensity decreases along the propagation direction. The losses are measured along the light propagation direction in a region containing the luminous streak but excluding the defect scattering centers: an exponential decreasing behavior of the light intensity was observed. If the optical signal registered as a function of the propagation distance is reported in logarithmic scale, as it can be seen in Figure 2.21, the light attenuation can be estimated by the slope of the this curve. The conversion in dB/cm of this number gives an estimated value of the losses equal to 22.3±0.9 dB/cm, in agreement with those reported in literature [13, 21].

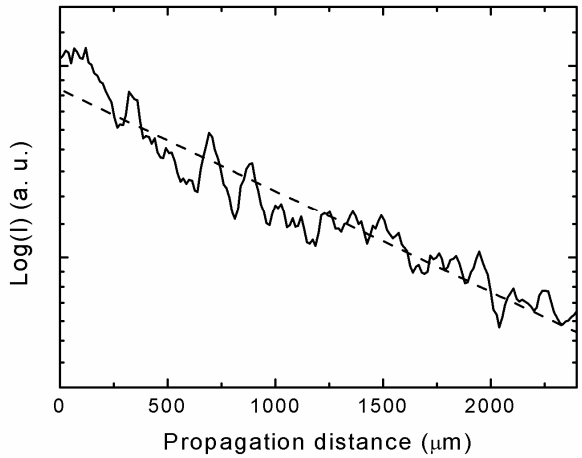

Figure 2.21. Logarithmic of the scattered light intensity versus the propagation distance at λ=1.55 μm.

References

[1] A. Uhlir, "Electrolytic Shaping of Germanium and Silicon", *The Bell System Technical Journal* **35**, 333-347 (1956).

[2] L. T. Canham, "Silicon quantum wire array fabrication by electrochemical and chemical dissolution of wafers", *Appl. Phys. Lett.* **57**, 1046-1048 (1990).

[3] R. L. Smith, S. D. Collins, "Porous silicon formation mechanisms", *J. Appl. Phys.* **71**, R1 (1992).

[4] V. Lehmann, U. Gösele, "Porous silicon formation: a quantum wire effect", *Appl. Phys. Lett.* **58**, 856 (1991).

[5] K. S. W. Sing, D. H. Everett, R. A. W. Haul, L. Moscou, R. A. Pierotti, J. Rouquerol, T. Siemieniewska, "Reporting physisorption data for gas solid systems with special reference to the determination of surface-area and porosity", *Pure Appl. Chem.* **57**, 603-619 (1985).

[6] V. Mulloni, L. Pavesi, "Porous silicon microcavities as optical chemical sensors", *Appl. Phys. Lett.* **76**, 2523 (2000).

[7] M. Ruike, M. Houzouji, A. Motohashi, N. Murase, A. Kinoshita, K. Kaneko, "Pore structure of porous silicon formed on a lightly doped crystal silicon", *Langmuir* **12**, 4828-4831 (1996).

[8] H. G. Tompkins, W. A. McGaham, "Spectroscopic Ellipsometry and Reflectometry", Ed. John Wiley & Sons.

[9] S. Zangooie, R. Jansson, H. Arwin, "Ellipsometric characterization of anisotropic porous silicon Fabry-Perot filters and investigation of temperature effects on capillary condensation efficiency", *J. Appl. Phys.* **86**, 850-858 (1999).

[10] C. Pickering, L. T. Canham, D. Brumhead, "Spectroscopic ellipsometry characterization of light-emitting porous silicon structures", *Appl. Sur. Sci.* **63**, 22-26 (1993).

[11] S. Zangooie, R. Bjorklung, H. Arwin, "Protein adsorption in thermally oxidized porous silicon layers", *Thin Solid Films* **313**, 825-830 (1998).

[12] D. E. Aspnes, "Investigation of effective-medium models of microscopic surface-roughness by spectroscopic ellipsometry", *Physical Review B* **20**, 3292-3302 (1979).

[13] P. Pirasteh, J. Charrier, Y. Dumeige, S. Haesaert, P. Joubert, "Optical loss study of porous silicon and oxidized porous silicon planar waveguides", *J. Appl. Phys.* **101**, 083110 (2007).

[14] P. Pirasteh, J. Charrier, A. Soltani, S. Haesaert, L. Haji, C. Godon, N. Errien, "The effect of oxidation on physical properties of porous silicon layers for optical applications", *Applied Surface Science* **253**, 1999-2002 (2006).

[15] J. J. Yon, K. Barla, R. Herino, G. Bomchil, "The kinetics and mechanism of oxide layer formation from porous silicon formed on p-Si substrates", *J. Appl. Phys.* **62**, 1042-1048 (1987).

[16] E. Pap, K. Kordás, G. Tóth, J. Levoska, A. Uusimäki, J. Vähäkangas, S. Leppävuori, T. F. George, "Thermal oxidation of porous silicon: study on structure", *Appl. Phys. Lett.* **86**, 041501 (2005).

[17] K. P. S. Dancil, D. P. Greiner, M. J. Sailor, "A porous silicon optical biosensor: Detection of reversible binding of IgG to a protein A-modified surface", *J. Am. Chem. Soc.* **121**, 7925-7930 (1999).

[18] P. A. Snow, E. K. Squire, P. S. J. Russell, L. T. Canham, "Vapor sensing using the optical properties of porous silicon Bragg mirrors", *J. Appl. Phys.* **86**, 1781 (1999).

[19] L. De Stefano, I. Rendina, L. Moretti, A. M. Rossi, "Optical sensing of flammable substances using porous silicon microcavities", *Mater. Sci. Eng. B* **100**, 271-274 (2003).

[20] H. F. Arrand, T.M. Benson, A. Loni, R. Arens-Fischer, M. Kruger, M. Thonissen, H. Luth, S. Kershaw, "Novel liquid sensor based on porous silicon optical waveguides", *IEEE Phot. Techn. Lett.* **10**, 1467-1469 (1998).

[21] V. Lehman, Electrochemistry of Silicon, Wiley-VCH Verlag GmbH & Co, 17–20, (2002).

[22] V. S. –Y. Lin, K. Motesharei, K. -P. S. Dancil, M. J. Sailor, M. R. Ghadiri, "A porous silicon based optical interferometric biosensor", *Science* **270**, 840 (1997).

[23] M. A. Anderson, A.Tinsley-Brown, P. Allcock, E. A. Perkins, P. Snow, M. Hollings, R. G. Smith, C. Reeves, D. J. Squirrell, S. Nicklin, T. I. Cox, "Sensitivity of the optical properties of porous silicon layers to the refractive index of liquid in the pores", *Phys. Stat. Sol. A* **197**, 528-533 (2003).

[24] M. A. Muriel, A. Carballar, "Internal field distributions in fiber Bragg gratings", *IEEE Photonics Technol. Lett.* **9**, 955-957 (1997).

[25] C. M. Soukoulis, E. N. Economou, "Localization in one-dimensional lattices in the presence of incommensurate potentials", *Phys. Rev. Lett.* **48**, 1043-1046 (1982).

[26] N. H. Liu, "Propagation of light waves in Thue-Morse dielectric multilayers", *Phys. Rev. B* **55**, 3543-3547 (1997).

[27] F. Baldini, A. N. Chester, J. Homola, S. Martellucci, eds., Optical Chemical Sensors, Springer, printed in the Netherlands, 179-192 (2006).

[28] T. N. Ding, E. Garmire, "Measuring refractive index and thickness of thin-films - a new technique", *Appl. Opt.* **22**, 3177-3181 (1983).

[29] H. Kogelnik, Integrated Optics, II ed., T. Tamir Ed., New York: Springer-Verlag (1979).

[30] D. J. Channin, J. M. Hammer, M. T. Duffy, "Scattering in ZnO-sapphire optical-waveguides", *Appl. Opt.* **14**, 923-930 (1975).

CHAPTER 3 OPTICAL SENSING OF CHEMICAL AND BIOLOGICAL MOLECULES BASED ON POROUS SILICON

(Papers J1, J2, J3, J6, J7, J9, J13, J14, J17, J20, J24, P1, P6, P9, P10, P12, P16, P17, P18, P23)

Lot of experimental work, exploiting the worth noting properties of PSi in chemical and biological sensing, has been recently reported in literature [1, 2]. PSi is an almost ideal material as transducer due to its porous structure, like a natural sponge, having a specific surface of the order of 200–500 m^2 cm^{-3} [3], so that a very effective interaction with several adsorbates is assured. Moreover, PSi is an available and low cost material, completely compatible with standard integrated circuit processes so that it could usefully be employed in the so-called smart sensors [4]. Several different transducer schemes have been proposed, based on changes in capacitance, resistence, reflectivity and photoluminescence properties of the material when biochemical molecules adsorb to its surface. The electric measurements are relatively straightforward and the control electronics for the device can be easily integrated on a silicon chip. On the other side, optical measurements can be less straightforward than electric ones but safer in case of flammable vapors. The performances of different PSi structures as optical transducers of chemical and biological substances are analyzed in this chapter.

3.1 Monitoring of Chemical Substances

The sensing mechanism in monitoring of chemical substances is based on the refractive index changes of PSi due to the partial substitution of the air in the pores by the chemicals to be detected. The pores can be filled by the liquid phase of vapors, due to the capillary condensation in the sponge-like PSi matrix, or by the chemical solutions which penetrate in the pores due to the surface tension. The condensation conditions depend not only on the average pore size, distribution, and shape but also on the strength of the interaction between the fluid and the pore walls [5]. Once the pores shape and the surface chemistry are fixed, a one-to-one correspondence exists between the condensation conditions and the pore diameters given by the Kelvin equation:

$$k_B T \rho_l \ln\left(\frac{p_{sat}}{p}\right) = 2\gamma_{\mathrm{lg}} \cos\frac{\theta}{R} \tag{3.1}$$

where ρ_l is the density of the liquid phase, γ_{lg} is the liquid-gas surface tension at temperature T, R is the radius of the pores, p/p_{sat} is the relative vapor pressure into the pore, and θ is the contact angle. From the Eq. 3.1 it is easy to see that the relative pressure increases with the average radius of pores R.

The sensitivity is a key issue of a sensor, so that several experimental works investigating the sensitivity of the different PSi structures have been reported in literature [6-8]. Ouyang et al. [9] focused their research on the sensitivity of PSi microcavities as function of the material properties, such as pore size, porosity, and number of layers. However, a general scheme to determine the performances of PSi optical sensors have not been proposed yet. In this paragraph, the sensitivities to the pore refractive index changes of two different PSi photonic structures are compared. In particular, a simple model to study the behavior of PSi multilayered structures on exposure to different compounds and to determine their response curve is proposed. The two multilayered structures analyzed are a one-dimensional periodic multilayer, the Bragg Mirror (BM), and an aperiodic multilayer, the Thue-Morse Sequence (TMS). Both the PSi structures are composed by 64 layers, 32 with high (H) refractive index (low-porosity), and 32 with low (L) refractive index (high-porosity). The layers thicknesses are $d_H=\lambda_0/4n_H$, and $d_L=\lambda_0/4n_L$, respectively. The different spatial order of the layers is the only difference between the two structures.

The interaction of PSi sensors with the chemical species induces a variation of effective refractive index of PSi layers, thus a shift of the multilayer reflectivity spectrum. The average refractive index of the PSi layer, n_p, can be determined in the near infrared range by using the Bruggemann effective medium approximation for a heterogeneous mixture of components (nanocrystalline silicon and pore contents):

$$(1-p)\frac{n_{Si}^2 - n_p^2}{n_{Si}^2 + 2n_p^2} + (1-p-\Lambda)\frac{n_{air}^2 - n_p^2}{n_{air}^2 + 2n_p^2} + \Lambda\frac{n_{ch}^2 - n_p^2}{n_{ch}^2 + 2n_p^2} = 0 \tag{3.2}$$

where Λ is the layer liquid fraction (LLF), i.e. the volume filled by the chemical species with refractive index n_{ch}, p is the porosity of layer, n_{Si}, and n_{air} are the refractive indices of silicon and air. From Eq. (3.2) the relative variation of the refractive index, $\Delta n_p/n_p$ as function of p, Λ, and n_{ch} can be numerically determined. In Figure 3.1 (a) e (b) the behavior of $\Delta n_p/n_p$ as function of Λ and n_{ch} for a PSi layer with p=0.5 is reported: the

relative change of the average refractive index of the layer has a linear dependence on the filling factor and the refractive index of the chemical species:

$$\frac{\Delta n_p}{n_p} = c_p (n_{ch} - 1)\Lambda \tag{3.3}$$

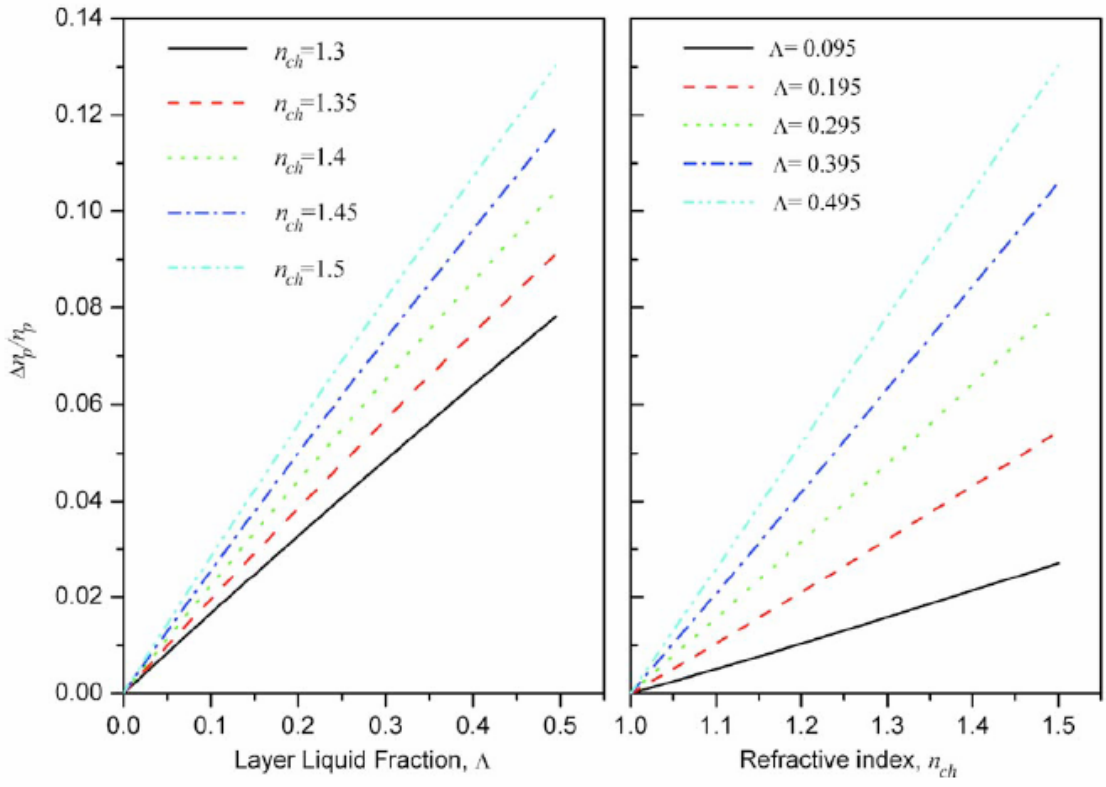

(a) (b)

Figure 3.1. Relative variation of PSi refractive index layer with p=0.5 as a function of layer liquid fraction for different refractive indices n_{ch} (a); as a function of n_{ch} for different layer liquid fractions (b).

The constant c_p depends on the layer porosity. It is well known that the refractive index change, due to the interaction of the PSi multilayers with external agents, preserves the shape of the reflectivity spectrum, so that it is still possible to individuate the resonant characteristics, i.e. the transmittance peaks of the TMS or the high reflectivity stop band of the BM. The shape of reflectivity spectrum depends on the phase modulation of each layer $\phi_i = 2\pi n_i d_i/\lambda$; for a couple of layers, the phase modulation is $\phi = \phi_L + \phi_H$. The reflectivity can be factorized as a product of two contributions:

$$R = A\left(\frac{n_L}{n_H}\right)\cdot \Re(\phi) \tag{3.4}$$

where the function A takes into account the value of the reflectivity due to the refractive index contrast, and $\Re$ is a shape factor due to the different optical paths of the light into the layers. If the reflectivity is simply shifted on a wavelength range without changing of the shape during the measurements process, it is possible to write that:

$$\Re[\phi(\lambda_r, n_i, d_i)] \cong \Re[\phi(\lambda_r + \Delta\lambda_r n_i + \Delta n_i d_i)] \quad (3.5)$$

where λ_r is the characteristic wavelength used as a reference to measure the spectral shift, Δn_i is the variation of the layer refractive index due to the interaction of the devices with the chemical species.

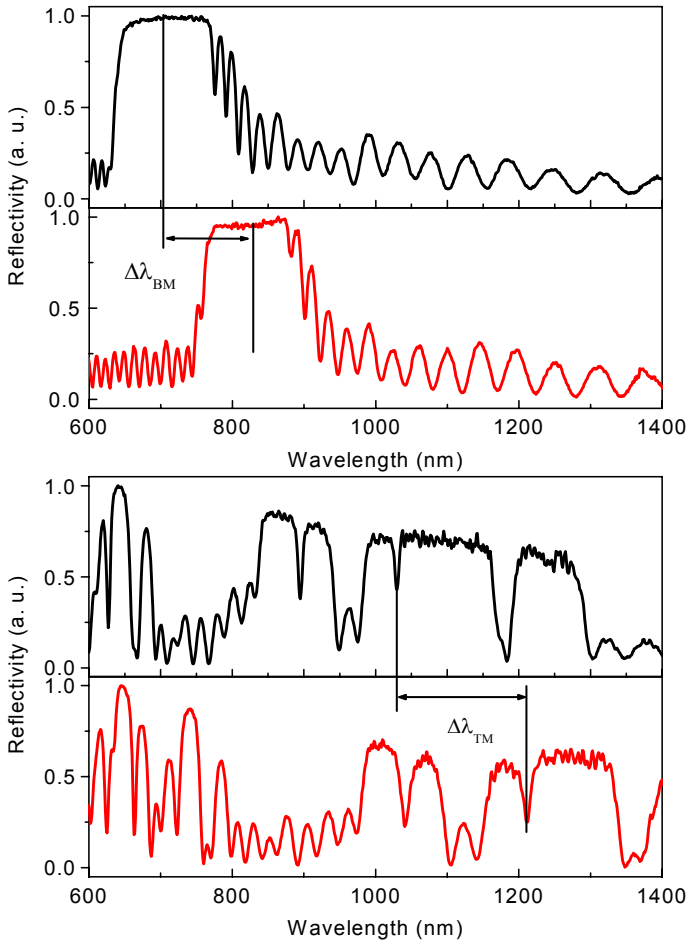

Figure 3.2. Experimental reflectivity spectra of Bragg multilayer (a, black line) and Thue-Morse multilayer (b, black line) composed by 64 layers. In red line are reported the reflectivity spectra after exposure to methanol. λ_{BM} and λ_{TMS} are the monitor wavelength for Bragg and Thue-Morse multilayer respectively.

The equality $\phi(\lambda_r,n_i,d_i)=\phi(\lambda_r+\Delta\lambda_r,n_i+\Delta n_i,d_i)$ can be deduced by the Eq. 3.4. By evaluating the variation of ϕ, an expression for $\Delta\lambda_r$ as function of layer refractive index variations, Δn_L, and Δn_H, can be deduced:

$$\Delta\lambda_r = 2\frac{\lambda_r}{\lambda_0}\left(d_L\,\Delta n_L + d_H\,\Delta n_H\right)=\frac{\lambda_r}{2}\left(\frac{\Delta n_L}{n_L}+\frac{\Delta n_H}{n_H}\right) \tag{3.6}$$

This formula is a powerful tool in the design of all resonant optical sensors, based on the average refractive index change. Combining the Eq. (3.6) with Eq. (3.3) it is possible to completely characterize the optical response of whatever PSi multilayer,

$$\frac{\Delta\lambda_r}{\lambda_r}=\frac{\left(n_{ch}-1\right)}{2}\left(c_L\Lambda_L + c_H\Lambda_H\right) \tag{3.7}$$

It is clear that the sensitivity of PSi multilayer depends strictly on the filling capability of the layers. The BM and the TMS have the same response as a function of the layer liquid fraction. In Figure 3.2 are shown the reflectivity spectra of BM (a) and TMS (b) when unperturbed, and on exposure to a methanol (n_{ch}=1.328) saturated atmosphere.

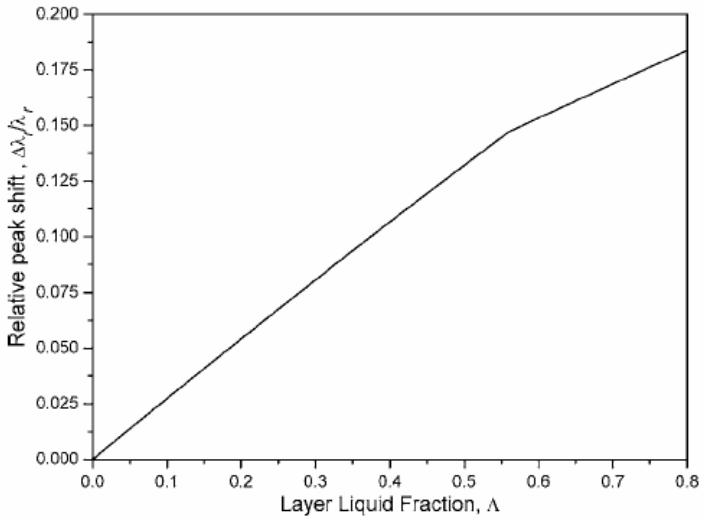

Figure 3.3. Calculated relative wavelength shift $\Delta\lambda_r/\lambda_r$ for BM and TMS as a function of layer liquid fraction Λ after exposure of methanol (n_{ch}=1.328). The two curves coincide.

The BM reflectivity shows a classic photonic band gap centered at the Bragg wavelength 2 ($n_L\,d_L+n_H\,d_H$)=712 nm. This wavelength is a natural candidate as monitor wavelength λ^{BM}_r, since it is simply recognizable after the interaction process. On the other side, the TMS spectrum shows a more complex photonic band gap structure due to the aperiodic sequence of the layers: three photonic band gaps can be observed in

wavelength intervals centered at 640 nm, 890 nm, and 1120 nm, and three resonant transmittance peaks at 894 nm, 1030 nm and 1184 nm. In this case, it is possible to choose λ_r among the one of the resonant transmittance peaks. In particular, the spectral shift of the resonance transmittance peak at 1030 nm (λ_r^{TMS}=1030 nm) is monitored. In Figure 3.3, using the Eq. (3.7), the relative wavelength shift, $\Delta\lambda_r/\lambda_r$ as a function of Λ on exposure to methanol obtained in the case of TMS and BM is reported. The filling can be assumed to proceed uniformly into the entire multilayer stack until the low porosity layers are completely filled ($\Lambda_L=\Lambda_H=\Lambda$ for $\Lambda<p_L$), then the filling process proceed only in high porosity layers [10, 11]: the filling curves in Figure 3.3 shows a slope change when $\Lambda= p_L$; the values of c_L and c_H are 0.927 and 0.677, respectively. In Table 3.1 are reported the experimental wavelength shifts and the layer liquid fractions extrapolated from the curve of Figure 3.3 for several compounds. First of all, it is worth noting that the pores filling is a characteristic parameter of the multilayer sequence, and is almost invariant respect to compound investigated, in agreement with Gurvitsch's rule which states that the volume of liquid adsorbed should be the same for all adsorptives on a given porous solid.

Table 3.1. Chemical orgainc substances and its refractive index used in sensing experiment. $\Delta\lambda_r^{TMS}$ ($\Delta\lambda_r^{BM}$) and Λ^{TMS} (Λ^{BM}) is the wavelength shift and the layer liquid fraction for Thue-Morse (Bragg) structures. The reference wavelength λ_r is 1030 nm for TMS and 712 nm for BM.

Solvent	n_{ch}	$\Delta\lambda_r^{TMS}$(nm)	Λ^{TMS}	$\Delta\lambda_r^{BM}$(nm)	Λ^{BM}
Methanol	1.328	180	0.745	108	0.599
Pentane	1.358	199	0.761	118	0.599
Isopropanol	1.377	209	0.761	125	0.599
Isobutanol	1.396	215	0.745	127	0.467

In Figure 3.4 is reported the response curve of both structures, the sensitivities, normalized to the reference wavelengths, are respectively, S^{TMS}=0.51(0.05) RIU^{-1} (Refractive Index Units) and S^{BM}=0.41(0.05) RIU^{-1}; the TMS higher sensitivity can be ascribed to higher filling capability. This effect can be explained by considering the number of *L-H* interfaces in the different multilayers. The different spatial order of layers between BM and TMS can be observed,

TMS: *LHHLHLLHHLLHLHHL…*

BM: *LHLHLHLHLHLHLHLH…*

It is possible to conclude that the periodic arrangement of the BM induces a greater number of porosity gradients, due to the presence of a greater number of *L-H* interfaces (63), than in TMS (42). These interfaces produce an inhomogeneity in the pore network which obstacles the propagation of the liquid phase and thus reduces the filling capability of structures. Therefore, after the condensation process or the capillary penetration, the liquid phase finds a more homogeneous pore network in TMS respect to BM.

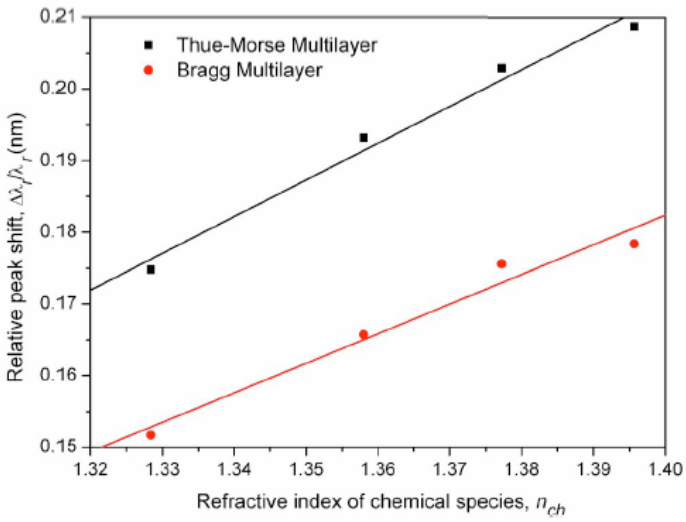

Figure 3.4. Experimental response curves of TMS and BM.

3.2 Surface Chemical Modification of "As-Etched" Porous Silicon

Unfortunately, a PSi sensor cannot discriminate the components of a complex mixture because the sensing mechanism is not selective. Some researchers have chemically or physically modified the Si–H surface sites in order to enhance the sensor selectivity through specific interactions. The common approach is to create a covalent bond between the PSi surface and the biomolecules which specifically recognize the target analytes [12, 13]. The reliability of a biosensor strongly depends on the functionalization process: how fast, simple, homogenous and repeatable it is. This step is also very important for the stability of the sensor: it is well known that 'as-etched' PSi has a Si–H terminated surface due to the Si dissolution process which is very reactive [14]. The substitution of the Si–H bonds with Si–C ones guarantees a much

more stable surface from the thermodynamic point of view. Three different PSi surface modification strategies in order to realize an optical biosensor are here reported: the target is the fabrication of sensitive label-free biosensors, which are highly requested for applications in high throughput drug monitoring and disease diagnostics; unlabelled analytes require in fact easier and faster analytical procedures.

FT-IR spectroscopy (Thermo - Nicholet NEXUS) has been used to compare the different passivation procedures: a pure chemical process based on Grignard Reactives; a photoinduced chemical modification based on the undecenoic organic acid and a passivation method simultaneous to the etching process. In each case the carboxyl-terminated monolayer covering the PSi surface acts as a substrate for the chemistry of the subsequent attachment of the DNA sequences.

Before the functionalization process the PSi substrate has been immersed in an aqueous ethanol solution, containing millimolar concentration of KOH, for 15 min. This alkaline treatment produces an increase in the porosity of about 15-20% [15] so improving the infiltration of the biomolecular probes into the pores. The process removes also most of the Si-H bonds from the PSi surface that can be restored by rinsing the PSi device in a low concentration HF-based solution (5 mM) for 30 s.

3.2.1 Chemical Functionalization by Grignard Reactives

The chemical functionalization is based on the Ethyl magnesium bromide (CH_3CH_2MgBr) as a nucleophilic agent which substitutes the Si-H bonds with the Si-C. The reaction was made at 85°C in an inert atmosphere (Argon) to avoid the deactivation of the reactive, for 8 hours. The chip was thus washed with a 1% solution of CF_3COOH in Diethyl Ether, and then with deionised water and pure Diethyl Ether. The modified surface chip was characterized by infrared spectroscopy to verify the efficiency of the method. The FT-IR spectrum is reported in Figure 3.5. The characteristic absorption peaks which identify the presence of organic species are well evident after the functionalization.

3.2.2 Photochemical Functionalization

The photo-activated chemical modification of PSi surface was based on the UV exposure of a solution of alkenes which bring some carboxylic acid groups. The PSi chip has been pre-cleaned in an ultrasonic acetone bath for 10 min then washed in deionized water. After dried in N_2 stream, it has been immediately covered with 10 %

N-hydroxysuccinimide ester (UANHS) solution in CH_2Cl_2. The UANHS was synthesised in house as described in ref. 12.

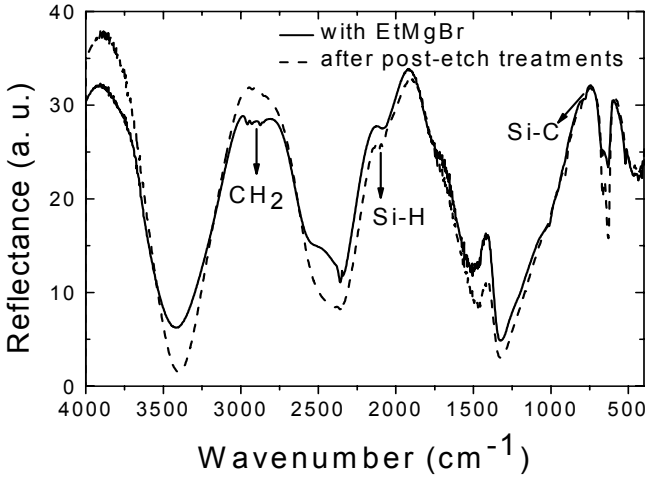

Figure 3.5. FT-IR spectra of the porous silicon monolayer before and after the pure chemical functionalization process based on EtMgBr.

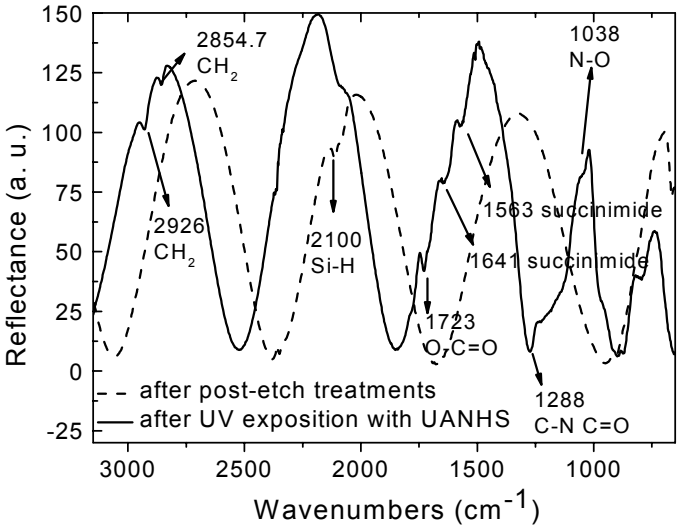

Figure 3.6. FT-IR spectra of the porous silicon monolayer before and after the photoinduced functionalization process based on UV exposure.

This treatment results in covalent attachment of UANHS to the PSi surface clearly shown in the FT-IR spectrum, reported in Figure 3.6. The chip was then washed in dichloromethane in an ultrasonic bath for 10 min and rinsed in acetone to remove any adsorbed alkene from the surface.

3.2.3 Functionalization During the Etch Process

The chemical modification of the PSi surface by directly using a functionalizing agent during the etching process has been studied. Some organic acids (eptinoic and pentenoic acid with concentrations ranging from 0.4 up to 3M) have been introduced in the electrochemical cell in presence of a diluted HF solution (HF:EtOH=1:2). In this case a current density of 60 mA/cm^2 was applied to etch an area of 0.07 cm^2. The FT-IR spectrum is reported in Figure 3.7.

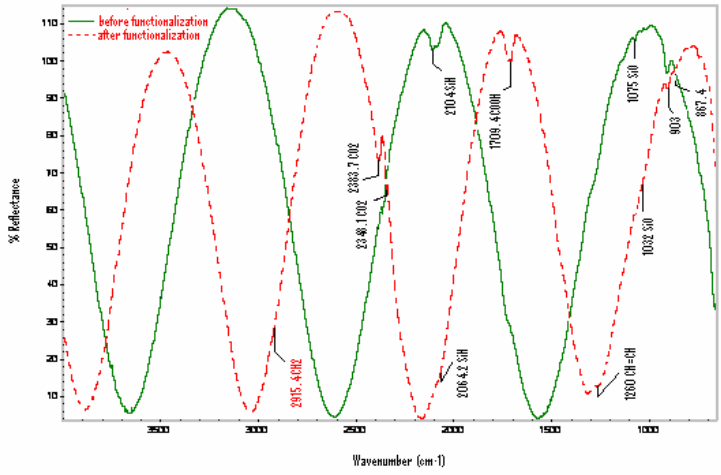

Figure 3.7. FT-IR spectra of the porous silicon monolayer before and after the functionalization during the etching process.

3.3 Optical Detection of DNA-DNA Hybridization

Among the three procedures experimented, the photoinduced method is the best one due to several reasons: the relaxed reaction conditions (atmospheric pressure and room temperature); the shorter reaction time and the best reaction yield (largest peaks recorded in FT-IR measurements). This last result is somewhat expected because the reactive considered has a so called “outgoing group”, the succinimide, which promotes its substitution with the ammine group of the DNA probe.

In view of these considerations, each chip with a photochemical modified surface has been incubated, over night, with fluorescent DNA single strand. After the chemical bonding of the labelled *ss*DNA, the chip was observed by the fluorescence macroscopy system. Under the light of the 100W high-pressure mercury lamp, a high and homogeneous fluorescence on the whole chip surface has been found; the fluorescence

still remains bright even after two overnight dialysis washings in a HEPES solution and in deionised water, as it can be seen in Figures 3.8 (a), (b), and (c).

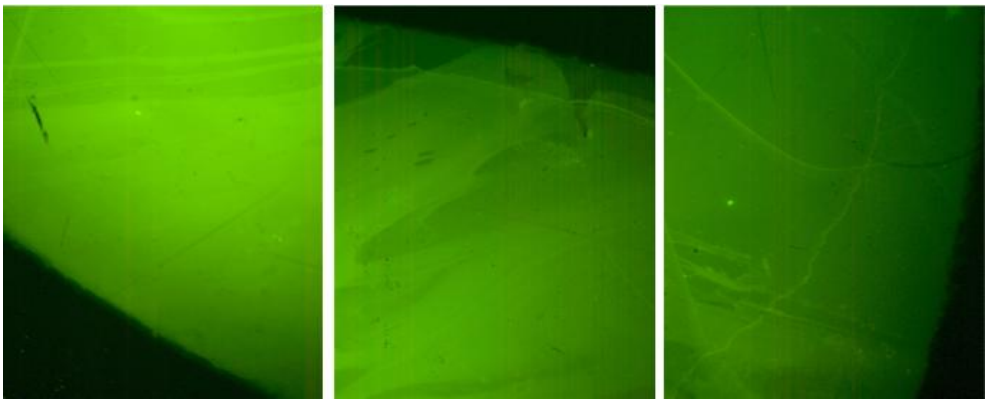

(a) (b) (c)

Figure 3.8. (a) Fluorescence of the chip surface after the binding of the labelled *ss*DNA; (b) after the overnight dialysis in HEPES solution; (c) after the overnight dialysis in deionised water.

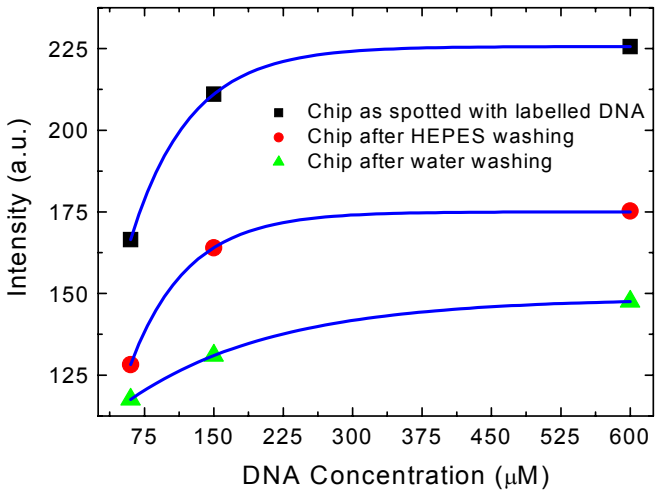

Figure 3.9. Fluorescence intensities of the chip surface after the binding of the labelled *ss*DNA and the two overnight dialysis as a function of the *c*DNA concentration.

The yield of the chemical functionalization has been studied by spotting different concentrations of the fluorescent *ss*DNA and measuring the fluorescence intensities of the images before and after the washings. The results reported in Figure 3.9 confirm the qualitative findings of Figure 3.8: the fluorescent intensities decrease but remain of the same order of magnitude. From this graph it is also possible to estimate the

concentration of the DNA probe which saturates the binding sites available (≈ 300 μM). The PSi optical biosensors measure the change in the average refractive index of the device: when a bio-recognition event takes place, the refractive index of the molecular complex changes and the interference pattern on output is thus modified.

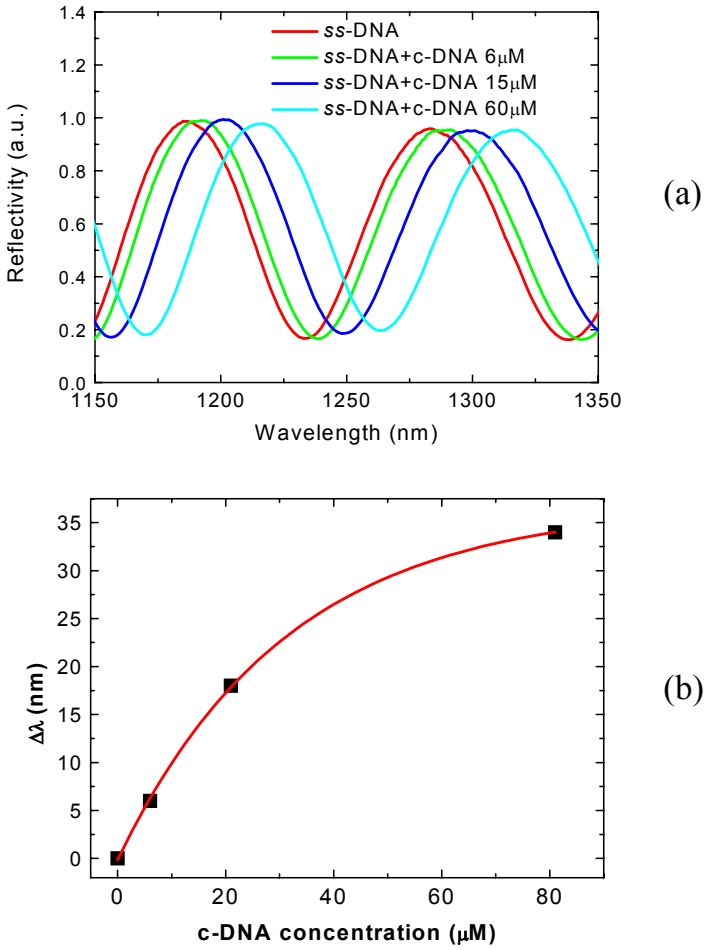

Figure 3.10. (a) Fringes shifts due to *ss*DNA-*c*DNA interaction. (b) Dose-response curve as a function of the *c*DNA concentration.

The label free optical monitoring of the *ss*DNA-*c*DNA hybridization is simply the comparison between the optical spectra of the porous silicon layer after the UANHS and probe immobilization on the chip surface and after its hybridization with the *c*DNA. Each step of the chip preparation increases the optical path in the reflectivity spectrum recorded, due to the substitution of the air into the pores by the organic and biological compounds. The interaction of the *ss*DNA with its complementary sequence has been detected as a fringes shift in the wavelengths, which corresponds to a change in the optical path. Since the thickness *d* is fixed by the physical dimension of the PSi matrix,

the variation is clearly due to changes in the average refractive index. In Figure 3.10 (a) the reflectivity spectra of the PSi layer for different *c*DNA concentration are reported, while in Figure 3.10 (b) a dose-response curve is reported. A control measurement has been made using a *nc*DNA sequence: a very small shift (less than 2 nm) has been recorded in the reflectivity spectrum respect to the one obtained after the probe linking. The sensor response has been fitted by a monoexponential growth model, $y=A(1-e^{-Bx})$, where A is the amplitude and B is the rate constant. The limiting sensitivity, i.e. the sensitivity in the limit of zero ligand concentration, $S=AB$, has been calculated obtaining the value 1.16 (0.04) nm/μM, which corresponds to a limit of detection (LOD) of 0.26 μM for a system able to detect a wavelength shift of 0.1 nm. The LOD is defined as three times the ratio between the standard deviation and the sensitivity according to IUPAC definition [16].

3.4 Protein Probes in Nanotechnology for Sugar Monitoring

The D-trehalose/D-maltose-binding protein (TMBP) from *T. litoralis* is a monomeric 48 kDa two-domain macromolecule containing 12 tryptophan residues [17]. It was found that TMBP is also able to bind glucose molecules [18]. Since human blood does not contain trehalose and maltose, it is not outrageous to envisage the use of the TMBP as a probe for the design of a minimally invasive biochip for glucose detection. The surface of a PSi Bragg mirror (BM) has been functionalized with TMBP by a three-step process, based on the chemical passivation of the PSi after the oxidation. Firstly, the PSi BM was thermally treated in O_2 atmosphere, at 1000°C for 30 min, to remove all the Si-H bonds and create an oxide layer on the pores surface to assure the covalent attachment with a proper chemical linker, the aminopropyltriethoxysilane (APTES). To this aim, the BM was rinsed by immersion in a 5% solution of APTES and an hydroalcoholic mixture of water and methanol (1:1), for 20 min at room temperature. After the reaction time, the chip was washed with DI-water and methanol and dried in N_2 stream. The silanized device was then baked at 100°C for 10 min.

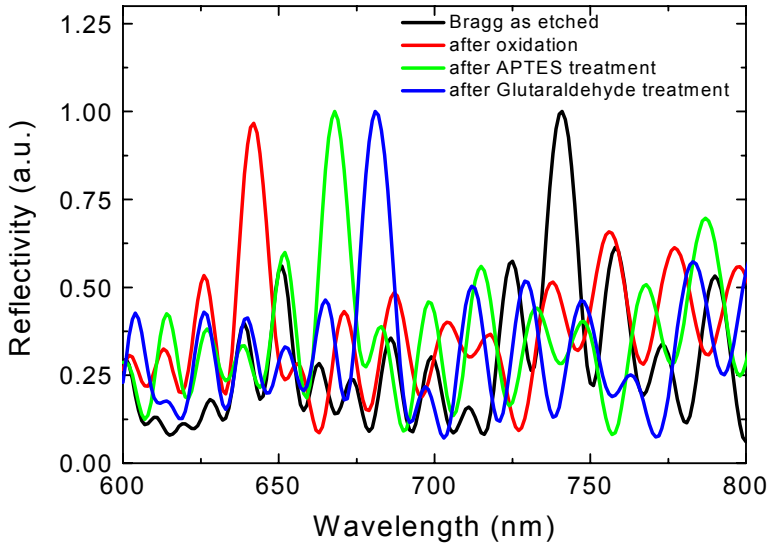

Figure 3.11. Optical reflectivity spectrum of the Bragg mirror as-etched (black curve), after oxidation (red curve), after APTES treatment (green curve) and after glutaraldehyde treatment (blue curve) .

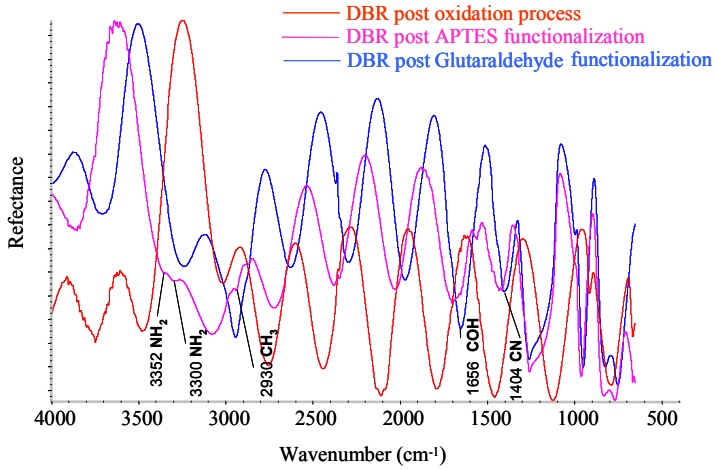

Figure 3.12. FT-IR spectra of the Bragg mirror after oxidation and APTES/glutaraldehyde treatment.

The next step consists in create a surface able to link the carboxylic group of the proteins: thus, the BM was immersed in a 2.5% glutaraldehyde solution in 20 mM HEPES buffer (pH 7,4) for 30 min, and then rinsed it in DI-water and finally dried in N_2 stream. The glutaraldehyde reacts with the amino groups on the silanized surface and coats the internal surface of the pores with another thin layer of molecules. All the

reaction steps were monitored by FT-IR spectroscopy and the consequent modification of the optical response of the PSi device by reflectivity spectroscopy. The modified surface binds the protein: 20 μl of 7.5 μM sodium bicarbonate buffer (pH 7.35) containing a rhodamine labelled TMBP were spotted on the PSi chip, then the system was incubated at -4°C over night. Even if the aim is the realisation of a label-free optical biosensor based on the PSi nanotechnology, a fluorescence protein was used to control the distribution of the biological matter on the chip surface and to test the chemical stability of the covalent link between the TMBP and the PSi surface. After this assessment phase, the ligand binding interaction was also optically detected by following the wavelength shift of the reflectivity spectrum.

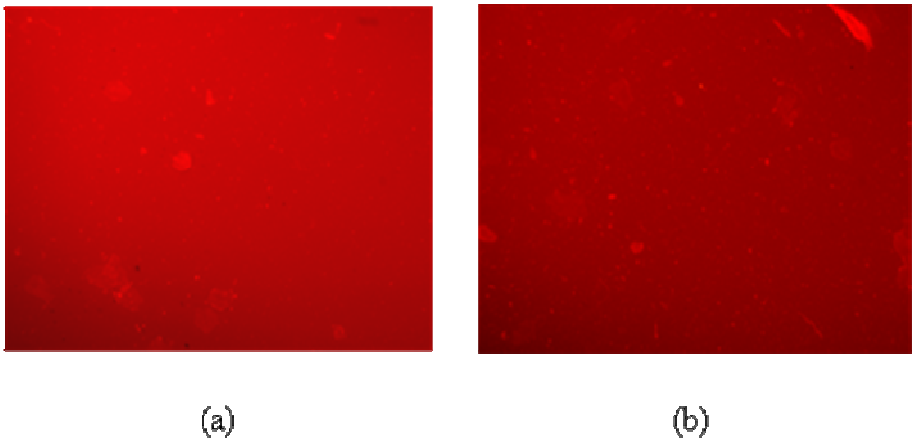

Figure 3.13. (a) Porous silicon chip after incubation with the labelled-TMBP. (b) Porous silicon chip after washings in demi-water

The experimental measurement of the TMBP-Glucose binding is a two step procedure: firstly, the optical spectrum of the porous silicon after the TMBP immobilization on the BM surface and after the Glucose solution has been spotted on it was registered. The Figure 3.11 shows the optical spectra of the device as etched and after each steps of the chemical treatment in the range 600-800 nm where the $m=5$ Bragg resonance peak at about *720 nm* is present. The oxidation process causes a blue shift of the reflectivity spectrum of 99.5 nm due to the lower value of the SiO_2 refractive index ($n_{oxi} \cong 1.5$) respect to the Si refractive index ($n_{Si} \cong 3.5$). On the contrary, the silanisation steps by APTES and glutaraldehyde produce red shifts of the reflectivity spectrum of 28 and 17 nm, respectively, corresponding to an increasing of the average refractive index of the layers due to a filling of the pores by the organic layers. Since the protein distributes

uniformly on the pores surface, the TMBP attachment causes a new detectable red shift of only 9 nm in the reflectivity spectrum. The FT-IR spectra of the oxide PSi sample and after the silanization process are reported in Figure 3.12: the main characteristic peaks of silicon dioxide (at 1124 cm^{-1}), of the APTES amino groups (at 3300 and 3352 cm^{-1}) and of gluteraldehyde cyano group (at 1404 cm^{-1}) are easily recognized. In Figure 3.13 (a) is shown the BM observed by a Leica Z16 APO fluorescence macroscopy system after incubation. By illuminating the chip spotted with the labeled protein, it was found that the fluorescence is very high and homogeneous on the whole surface. It was also qualitatively tested the strength of covalent bond between the protein and the PSi surface by washing the device in a dialysis membrane overnight in DI-water (Figure 3.13 (b)).

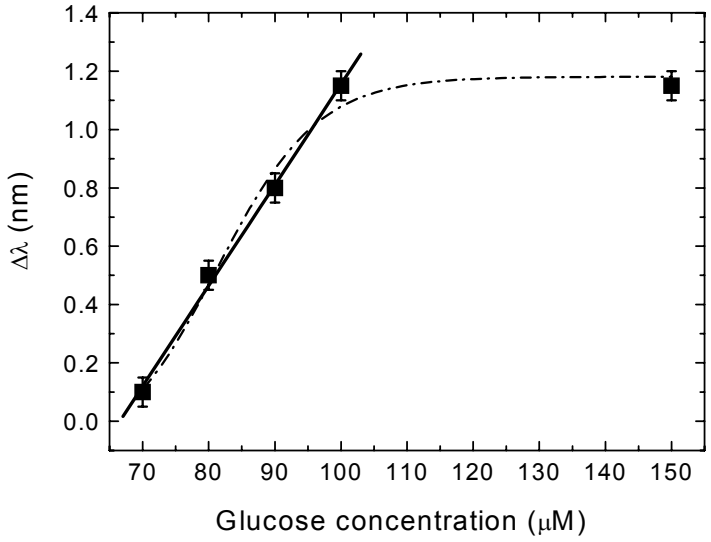

Figure 3.14. Dose-response curve for PSi BM optical sensor exposed to several concentration of glucose

Since the fluorescent intensities differ of only few counts, the PSi-TMBP double layer is very stable. The signal response to the glucose concentration was also measured after the interaction with the protein in a range between 70 and 150 μM. The maximum shift of the Bragg wavelength is 1.2 nm. Figure 3.14 shows the dose-response curve to glucose additions. The estimated sensitivity of the TMBP-Chip is 0.034 (0.001) nm/μM corresponding to a LOD of 9 μM. Interestingly, the concentration of glucose that induces a optical response of the protein is very close to the amount of the sugar present in the human interstitial fluids. This result suggests the use of this protein in designing

of a non-consuming and minimally invasive biosensor for the continuous detection of the level of glucose in diabetic patients.

References

[1] K. P. S. Dancil, D. P. Greiner, M. J. Sailor, "A porous silicon optical biosensor: Detection of reversible binding of IgG to a protein A-modified surface", *J. Am. Chem. Soc.* **121**, 7925-7930 (1999).

[2] L. De Stefano, L. Moretti, A. M. Rossi, M. Rocchia, A. Lamberti, O. Longo, P. Arcari, I. Rendina, "Optical sensors for vapors, liquids, and biological molecules based on porous silicon technology", *IEEE Trans. Nanotech.* **3**, 49 (2004).

[3] R. Herino, G. Bomchil, K. Barla, C. Bertrand, J. L. Ginoux, "Porosity and pore-size distributions of porous silicon layers", *J. Electrochem. Soc.* **134**, 1994-2000 (1987).

[4] L. De Stefano, L. Moretti, I. Rendina, A. M. Rossi, S. Tundo, "Smart optical sensors for chemical substances based on porous silicon technology", *Appl. Opt.* **43**, 167 (2004).

[5] V. Neimark, P. I. Ravikovitch, "Capillary condensation in MMS and pore structure characterization", *Microporous Mesoporous Mater.* **44-45**, 697-707 (2001).

[6] H. Ouyang, P. Fauchet, "Biosensing using porous silicon photonic bandgap structures", Proc. SPIE 6005, 600508-1 (2005).

[7] H. Ouyang, C. Striemer, P. M. Fauchet, "Quantitative analysis of the sensitivity of porous silicon optical biosensors", *Applied Physics Letters* **88**, 163108 (2006).

[8] J. Volk, T. Le Grand, I. Barsony, J. Gombkoto, J. J. Ramsden, "Porous silicon multilayer stack for sensitive refractive index determination of pure solvents", *J. Phys. D* **38**, 1313-1317 (2005).

[9] H. Ouyang, M. Christophersen, R. Viard, B. L. Miller, P. M. Fauchet, "Macroporous silicon microcavities for macromolecule detection", *Adv. Funct. Mater.* **15**, 1851-1859 (2005).

[10] P. A. Snow, E. K. Squire, P. S. J. Russell, L. T. Canham, "Vapor sensing using the optical properties of porous silicon Bragg mirrors", *J. Appl. Phys.* **86**, 1781 (1999).

[11] P. Allcock, P. A. Snow, "Time-resolved sensing of organic vapors in low modulating porous silicon dielectric mirrors", *J. Appl. Phys.* **90**, 5052-5057 (2001).

[12] H. B. Yin, T. Brown, R. Gref, J. S. Wilkinson, T. Melvin, "Chemical modification and micropatterning of Si(100) with oligonucleotides", *Microelectron. Eng.* **73/74**, 830–6 (2004).

[13] B. R. Hart, S. E. Letant, S. R. Kane, M. Z. Hadi, S. J. Shields, J. G. Reynolds, "New method for attachment of biomolecules to porous silicon", *Chem. Commun.* (3), 322–323 (2003).

[14] L. Canham, ed., Properties of Porous Silicon, INSPEC, London, UK (1997).

[15] L. A. DeLouise, B. L. Miller, "Optimization of Mesoporous Silicon Microcavities for Proteomic Sensing", *Mat. Res. Soc. Symp. Proc.* **782**, A5.3.1-A5.3.7 (2004).

[16] IUPAC Compendium of Analytical Nomenclature, Definitive Rules, 3d Edition, Section 10.3.3.3.14 "Limit of Detection" (1997).

[17] J. Diez, K. Diederichs, G. Greller, R. Horlacher, W. Boos, W. Welte, "The crystal structure of a liganded trehalose/maltose-binding protein from the hyperthermophilic archaeon Thermococcus litoralis at 1.85 A", *J. Mol. Biol.* **305,** 905-915 (2001).

[18] P. Herman, I. Barvik, M. Staiano, A. Vitale, J. Vecer, M Rossi, S. D'Auria, "Temperature modulates selectivity and affinity binding properties of the D-trehalose/D-maltose-binding protein from the hyperthermophilic archaeon Thermococcus litoralis", *BBA-Proteins and Proteomics* **1774**, 540-544 (2006).

CHAPTER 4 BIOLOGICAL PASSIVATION OF POROUS SILICON

(Papers J15, J18, J23, P19)

Recently, in the microelectronic and nano-device fabrication field, an increasing interest has been devoted to the utilization of nanostructured biological molecules purified by living organisms or synthesized in laboratory. Hybrid organic-inorganic devices which exploit the best features of both worlds can be designed and realized. Among all the biological molecules that nature has optimized during life's history on earth, *Hydrophobins* are particularly attractive because of their biophysical features. In this chapter, the technological applications of the hydrophobins in the silicon micromachining and PSi surface passivation are discussed.

4.1 Selfassembled Biofilm on Silicon

Hydrophobins (HFBs) are small proteins, constituted by 100-125 amino acids residues, which can be purified by filamentous fungi. These amphiphilic proteins can strongly adhere to hydrophobic or hydrophilic surfaces, have high surface activity and self-assemble in membranes or biofilms [1]. Due to their very peculiar characteristics, hydrophobins have been recently proposed for lot of practical applications, ranging from anti-fouling to the fabrication of new biomaterials [2]. Hydrophobins are divided in two classes on the basis of the stability of the assembled biofilm: the class I hydrophobins form high insoluble assemblies, which can be dissolved in strong acids, whereas class II biofilms can be dissolved in ethanol or in sodium dodecyl sulphate. The most studied hydrophobins are the SC3 hydrophobins from *Schizophyllum commune* (class I) and the HFBI and HFBII (class II) from *Trichoderma reesei* [3].

In this study, a class I hydrophobin from the fungus *Pleurotus ostreatus* has been purified.

Ethanol-deionized water (80%-20% V/V) solutions containing 0.11 mg/ml of hydrophobins have been deposited on two different surfaces, crystalline silicon and silicon dioxide (72 nm thick), by drop covering. The first surface, after rinsing in pure hydrofluoridic acid, shows a hydrophobic behaviour, whereas the second one is completely hydrophilic. Each sample has been incubated for 1h, then dried for 10 min

on the hot plate (80°C) and washed by the same solution used for the deposition. The optical parameters and the thickness of the self-assembled HFBs biofilm were determined by variable angle spectroscopic ellipsometry (VASE).

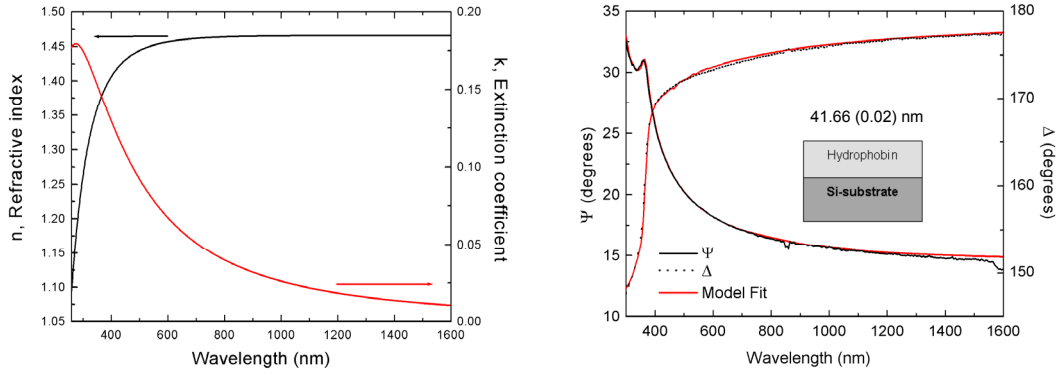

(a) (b)

Figure 4.1. (a) Refraction index and extinction coefficient of the hydrophobins as a function of wavelength. (b) Measured and fitted ellipsometric spectra of the biofilm deposited on crystalline silicon.

The Figure 4.1 (a) reports the refractive index and the extinction coefficient of the HFBs as a function of the wavelength calculated by means of the Cauchy dispersion model for absorption media [4]:

$$n(\lambda) = n_0 + \frac{n_1}{\lambda^2} + \frac{n_2}{\lambda^4}$$
$$k(\lambda) = k_0 + \frac{k_1}{\lambda^2} + \frac{k_2}{\lambda^4} \qquad (4.1)$$

where n_0, n_1 and n_2 are called the *Cauchy parameters* and k_0, k_1 and k_2 the *Cauchy extinction coefficients*. This gives a value of the refractive index of 1.459 at λ=633nm, which is typical for proteins. Using these dispersion models, the thickness of the biofilm assembled on crystalline silicon was estimated. After three consecutive depositions, for a total time of three hours, a value up to 40 nm has been obtained, as shown in the inset of Figure 4.1 (b). By optical characterization, it also been discovered that the same deposition procedure of hydrophobins on silicon oxide also produces an assembled biofilm which is thinner than in the case of crystalline silicon. In case of thermal silicon dioxide the biofilm reached a maximum thickness of about 20 nm. This different behaviour can be ascribed to the greater number of hydrophobic residues present on the outer of the protein which better promote the hydrophobic interaction. The self-

assembled protein biofilm changes the wettability of the substrate. The changing in silicon wettability has been monitored by water contact angle (WCA) measurements.

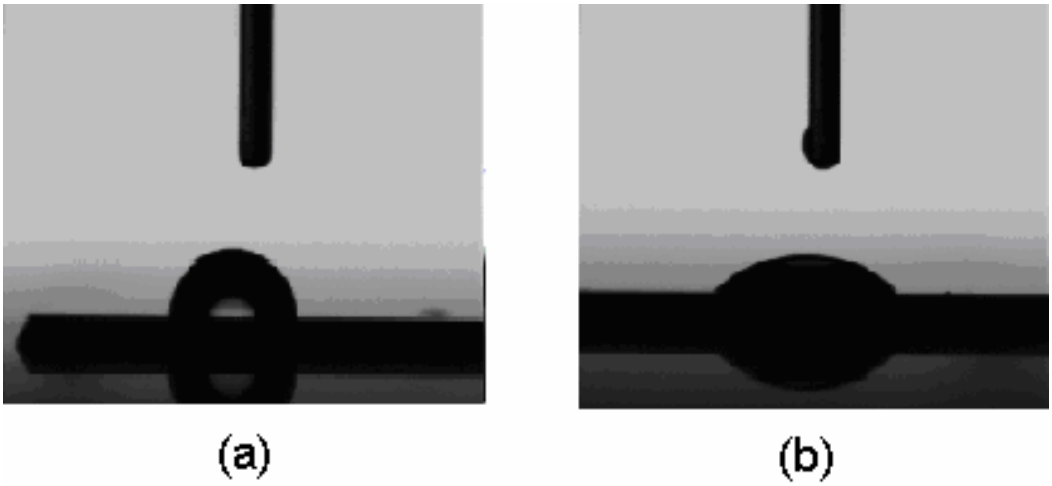

Figure 4.2. Changing the wettability of silicon and oxidized silicon: the hydrophobin nanolayer turns the hydrophobic surface of silicon in hydrophilic and the hydrophilic surface of oxidized silicon in hydrophobic. (a) A water drop on silicon forms a contact angle of 90°. (b) A water drop on silicon after HFBs deposition forms a contact angle of 38°.

In Figure 4.2 (a) and (b) the WCA results in case of the bare silicon and after the deposition of the HFBs biofilm are reported, respectively. The dramatic increase in wettability of the silicon surface is well evident: in the first case, the WCA results in 90°±1°, so that the surface can be classified as hydrophobic, while after the HFB deposition the WCA falls down to 38°±2° so that the surface is clearly hydrophilic. The adhesion characteristics of the hydrophobin biofilm on silicon have been studied by washing the sample in 2% sodium dodecyl sulphate (SDS) at 100 °C for 10 minutes and in sodium hydroxide (NaOH) solution 0.1 M, for 10 minutes [5]. The rinsing in the SDS solvent removes on average the 90 % of the biofilm, while the basic solution removes only the 42 % of the hydrophobin layer. HFBs film is formed via strong noncovalent interactions among these small proteins. Therefore peculiar properties of their assembly can be ascribed solely to hydrophobin amino acid sequences and consequently to their 3D structures. The high persistence of the hydrophobin film on the silicon surface is due to its characteristic assembly in a β-sheet structures, confirmed by the presence of the amide I band at 1636 cm^{-1} in the Fourier transformed infrared spectroscopy (FTIR) spectrum [5], reported in Figure 4.3. The sinusoidal modulation in the FTIR spectrum is

due to the reflections from the bottom of the intrinsic silicon wafer which is 400 μm thick.

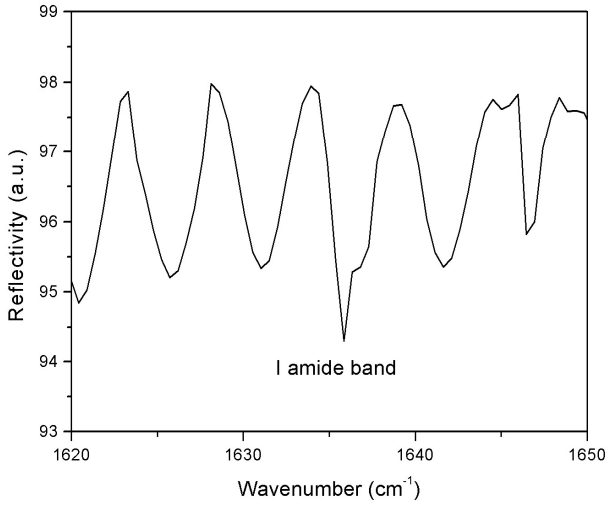

Figure 4.3. FTIR spectrum of the hydrophobins after assembling on intrinsic crystalline silicon surface.

4.2 Protein Masking in KOH Wet Etching of Silicon

Since the protein biofilm has not been removed from the silicon surface on exposure to the basic solution, the protection ability against the standard chemical etch solution for crystalline silicon, the potassium hydroxide (KOH) [6], has been studied. It was found that the hydrophobin biofilm, even if thinned, perfectly protects the silicon surface. To this aim, a silicon wafer was thermally oxidized since silicon dioxide is a good masking material for KOH wet etches. Then, the oxide (130 nm thick) was removed in a controlled area by highly concentrated HF and the wafer was exposed to KOH (water solution 1: 2 w/w) at 80 °C in a thermostatic bath, for 30 sec. In this condition the KOH etch rate is of 1400 nm/min. A twin sample, with the crystalline silicon area covered by the hydrophobins self-assembled biofilm, has been immersed in the KOH bath in the same conditions. In Figure 4.4 the optical photos of the two silicon samples after this treatment, are shown: on the left is clearly visible the etched surface whereas in the right image the surface is perfectly homogeneous. This qualitative result is quantitative confirmed by ellipsometric and profilometric measurements: an 8.40 (0.05) nm biofilm of hydrophobins is still optically detected by the ellipsometer and the profilometer

cannot detect any dig into the hydrophobins shielded sample, as it can be seen in Figure 4.5.

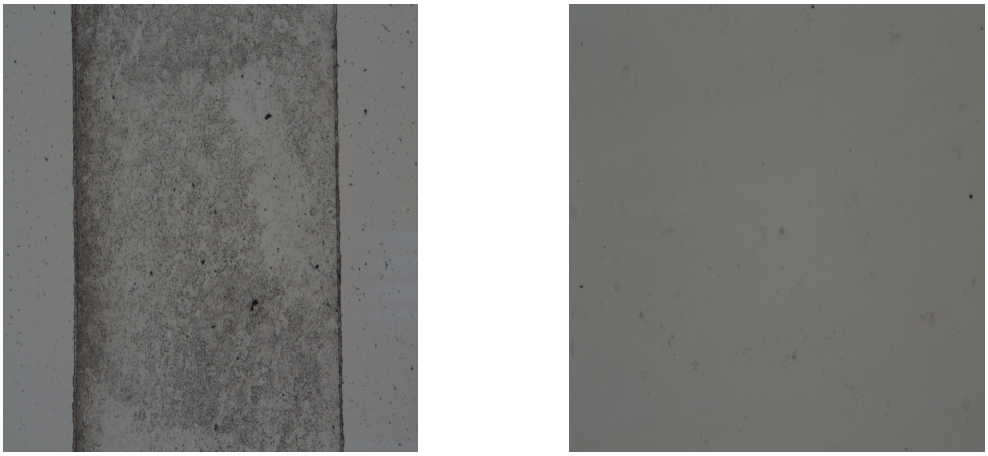

Figure 4.4. Optical photographs of the silicon chips after KOH wet etch: left, a 700 nm etched dig on unprotected crystalline silicon; right, unetched silicon surface protected by the hydrophobin biofilm.

It was also verified how long the self-assembled biofilm defends the silicon surface against the KOH wet etch: a prolonged exposition of the protein coated wafer decreases the biofilm thickness down to 5 nm, then the film is stable at least on a time scale of 20 minutes. This value is probably the one corresponding to a monolayer of proteins assembled as a film on the silicon surface. The homogeneity of the residual surface is also confirmed by AFM measurement, reported in Figure 4.6. In all the explored areas the protein layer appears compact and no hole in the layer can be observed. Due to the simplicity of the hydrophobin deposition, an effective shielding against prolonged expositions to KOH can be obtained by spotting the protein solution over the masked areas before continuing the etch process. Following the same experimental procedure, it was also studied if the hydrophobins film could protect the silicon dioxide against the HF wet etch. In this case, the proteins are only partially successful: a 72 nm layer of silicon dioxide is completely removed in 5 minutes by 1:10 HF-water solution at room temperature, while 21 nm of silicon dioxide are still present on a protein masked sample.

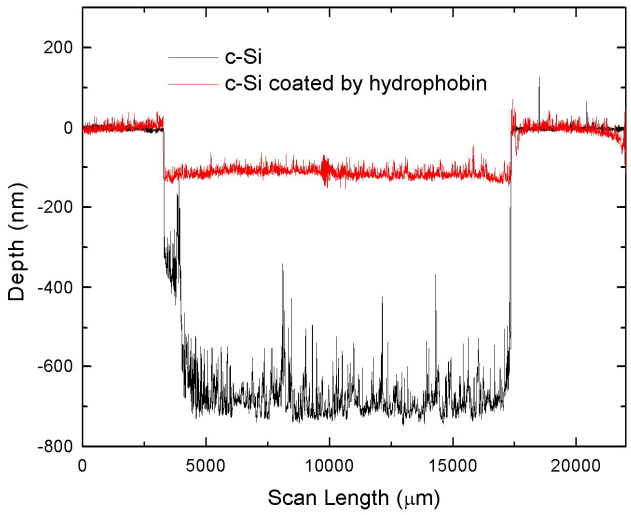

Figure 4.5. Thickness profiles measured by the profilometer for both the samples.

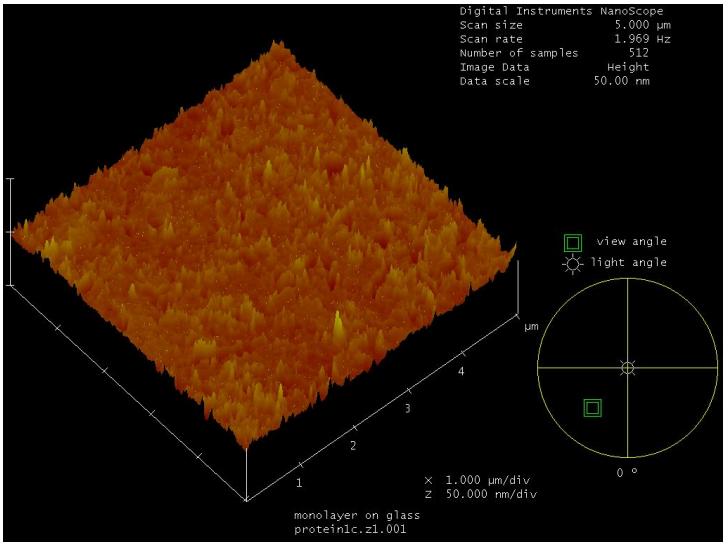

Figure 4.6. AFM height image of a hydrophobin coated sample.

4.3 Protein Modified Porous Silicon Surface

Once the HFBs biofilm was characterized on crystalline silicon substrate, the proteins were infiltrated by adsorption in PSi monolayers and multilayers. The protein coated surface of PSi takes advantages of the HFBs properties gaining chemical stability and variable wettability.

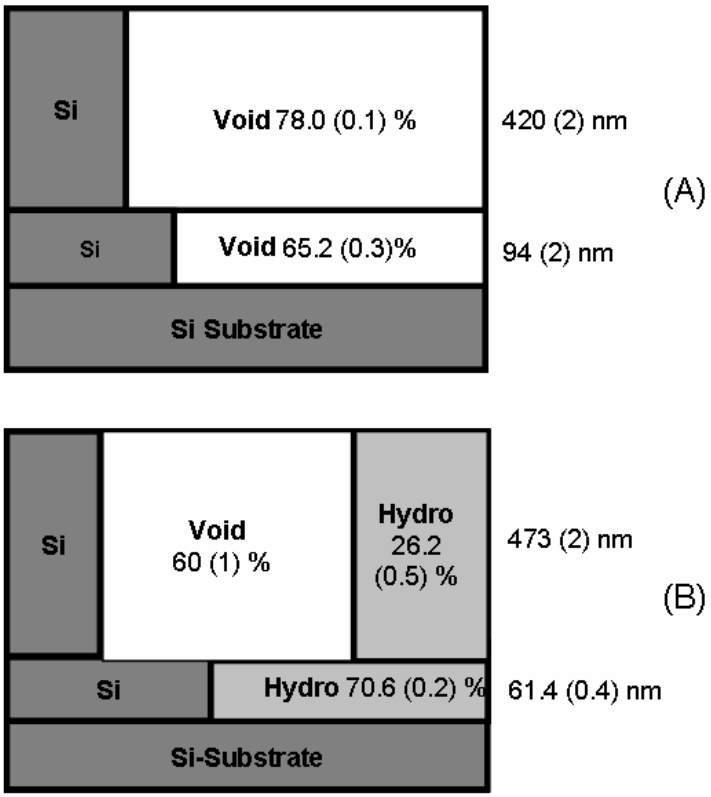

Figure 4.7. The ellipsometric model of the hydrophobin infiltration in a PSi monostrate. (a) The PSi monolayer as etched is characterised by a vertical voids distribution. (b) Also in the protein modified PSi monolayer the biological matter shows a not uniform distribution in the sample.

In Figure 4.7 is reported the VASE characterisation of a 514 nm PSi monolayer of about 76 % of porosity as etched (a) and after the HFB infiltration (b). Due to the hydrophobic interaction, the HFBs penetrate in the whole stack, cumulating at the bottom where the hydrogen concentration is higher since the hydrostatic pressure stops the air penetration. As observed in the paragraph 4.1, the HFB biofilm, when self-assembled on planar crystalline silicon, measures about 3 nm after the standard washing procedure with sodium hydroxide and sodium dodecyl sulphate.

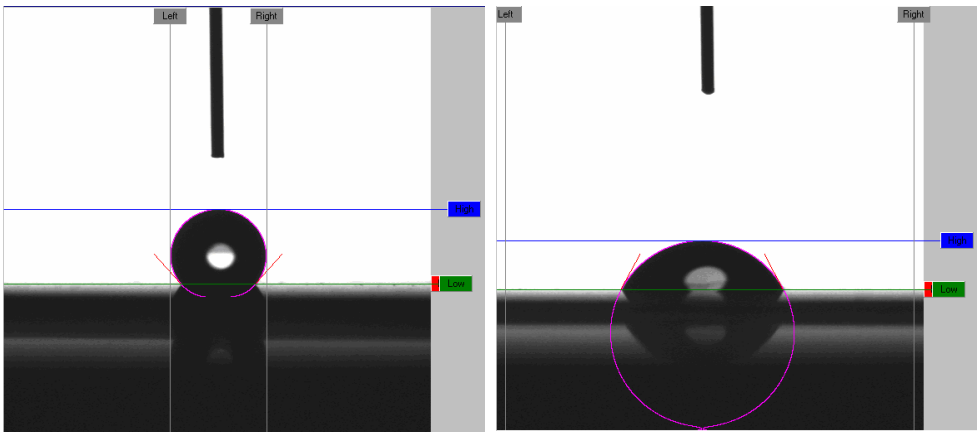

(a) (b)

Figure 4.8. Changing the wettability of PSi: the hydrophobin nanolayer turns the hydrophobic surface of PSi into a hydrophilic one. (a) A water drop on the PSi as etched forms a contact angle of 131°. (b) A water drop after the hydrophobin infiltration forms a contact angle of 62°.

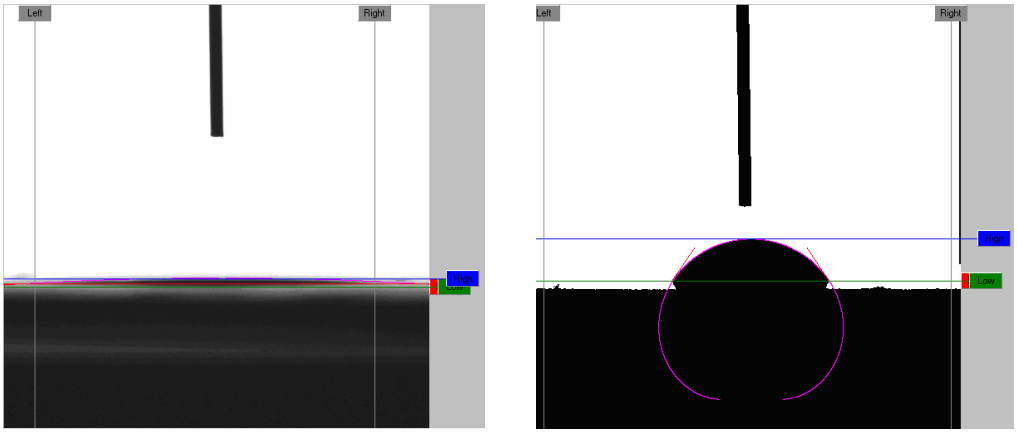

(a) (b)

Figure 4.9. Changing the wettability of the oxidised PSi: the hydrophobin nanolayer turns the hydrophilic surface of the oxidised PSi into a hydrophobic one. (a) A water drop on the oxidised PSi forms a contact angle of 6°. (b) A water drop after hydrophobin infiltration forms a contact angle of 57°.

These values are compatible with the size dimension of the mesoporous material, ranging from 5 to 30 nm [7]. This nanometric organic layer is able to strongly modify the wettability of the PSi surface: after the electrochemical etching process, the PSi is highly hydrophobic (see Fig. 4.8 (a)) resulting in a water contact angle value of 131°, while after HFB infiltration the same surface shows a hydrophilic behaviour and the

water contact angle is reduce to 62° (Fig. 4.8 (b)). Following the same procedure, it is possible to turn the highly hydrophilic surface of the oxidised PSi into a slightly hydrophobic one as demonstrated by the images reported in Figure 4.9 (a) and 4.9 (b). The ability to switch between two different wettability regimes could be a key feature in designing bioactive interfaces for miniaturization not only of biosensors, but also of medical devices [8].

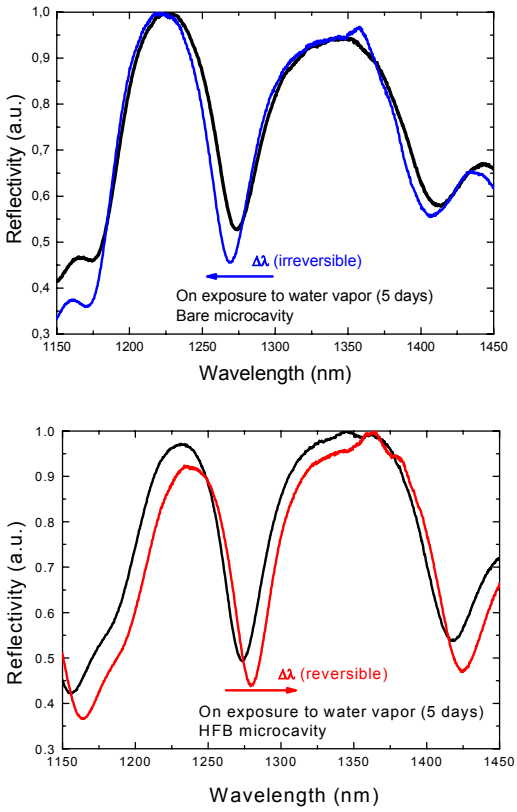

Figure 4.10. The protein infiltration into the PSi structure strongly modifies its behavior on exposure to water vapors. (a) PSi bare microcavity. (b) PSi protein infiltrated microcavity.

The different behaviors of two PSi optical microcavities, one bare and one infiltrated with HFB, were studied on exposure to water vapors. The bare microcavity is characterized by a hydrophobic surface. The water vapors can not condensate into the PSi pores and only an irreversible blue-shift in the reflectivity spectrum of the structure is observed due to a partial oxidation of its surface (Figure 4.10 (a)). In the case of HFB infiltrated microcavity a reversible red-shift is recorded, as shown in Figure 4.10 (b), due to the capillary condensation of the vapors into the pores. The condensation of the

water is now possible because the PSi surface has been made hydrophilic by the HFB infiltration.

4.4 Protection against NaOH Etching in Porous Silicon Structures

In the paragraph 4.2, it is demonstrated that a nanometric biofilm of HFB, self-assembled on planar crystalline silicon, perfectly acts as a mask material during a standard wet etch process based on the KOH. After these encouraging results, it was tested the shielding ability of the HFB biofilm against the etch ability of NaOH, when self-assembled on the internal surface of porous silicon monolayers and multilayers.

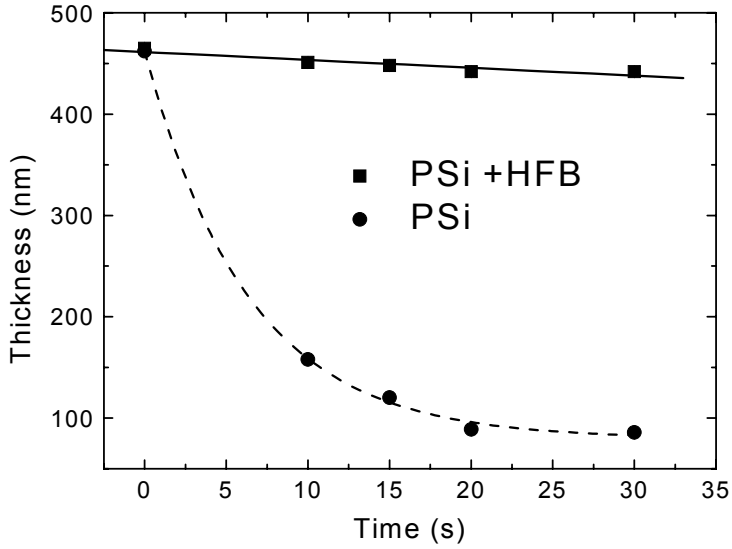

Figure 4.11. The hydrophobins protect the PSi against dissolution in basic solutions: a layer of a protein modified PSi sample is very slowly etched, while the PSi layer not infiltrated is heavily reduced on the same time scale.

The Figure 4.11 shows the results of the ellipsometric measurements to compare the dissolution rate of two PSi twins monolayers (thickness 465 nm, porosity = 72 %), one protein coated and the other bare, on exposure to a NaOH 0.1 M (pH = 12.5) water solution for equal times. Both the samples are VASE characterized at the same time intervals, so to directly assess the competition between the oxidation and the dissolution processes. It was never revealed the formation of an oxide layer on both the samples, but only a reduction of the films width together with the increasing of their porosity. In particular, the thickness of the coated sample changes of about 4 %, while in the case of

the bare sample of about the 81 %, in the same time interval. The chance of giving strong chemical stability to the porous silicon without modifying its intimate structure is even more intriguing in case of PSi based photonic crystals which are quite ideal transducers devices in chemical and biological sensing experiments. Furthermore, the protein nanobiofilm is completely transparent from ultraviolet to near infrared wavelengths so that it is perfectly compatible with optical applications. In Figure 4.12 the transmission curves of two different biofilms on silicon are reported. In both cases the self-assembled layer is transparent in a very large interval of wavelengths: the transmittance is still the 80% at 300 nm.

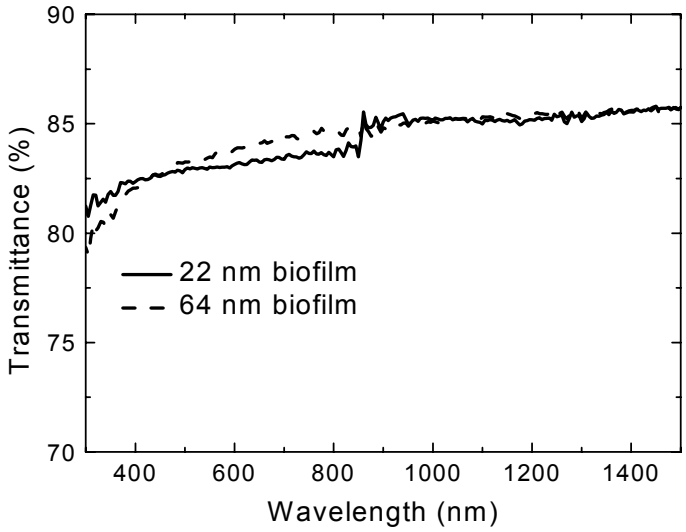

Figure 4.12. Transmission curves of two different samples of HFB self-assembled biofilm on silicon substrate.

Thus, a PSi optical microcavity (PSMC) was infiltrated by the HFB solution. In this case, the ellipsometry is not well suited to analyse such thick and multilayered samples [9], so that the spectroscopic reflectometry has been used [10]. The reflectivity spectra of two PSMCs, one coated by the HFB protein, and the other bare, have been recorded by an optical spectrum analyser. In Figure 4.13 the optical spectra of both samples for a rapid comparison are reported. On exposure to a 0.1 M aqueous solution of sodium hydroxide, the protein coated microcavity undergoes a blue-shift of about 329 nm, due to the removal by NaOH dissolution of some unprotected silicon nanocrystallites, while in the same time the uncoated sample is completely dissolved: the unmodulated continuous line at bottom of the (a) graph reproduces the source spectrum; on the

contrary, the (b) graph retains the starting characteristic shape of the microcavity. Even if blue-shifted, the optical spectrum yet shows a reflectivity stop band of about 50 nm with a well defined transmission defect inside. The coated PSMC has been also exposed to the sodium phosphate (20 mM, pH = 8) and Hepes (pH = 7.5) buffer solutions, which are often used in biological experiments, to test the chemical stability of the porous silicon structure in these standard environments.

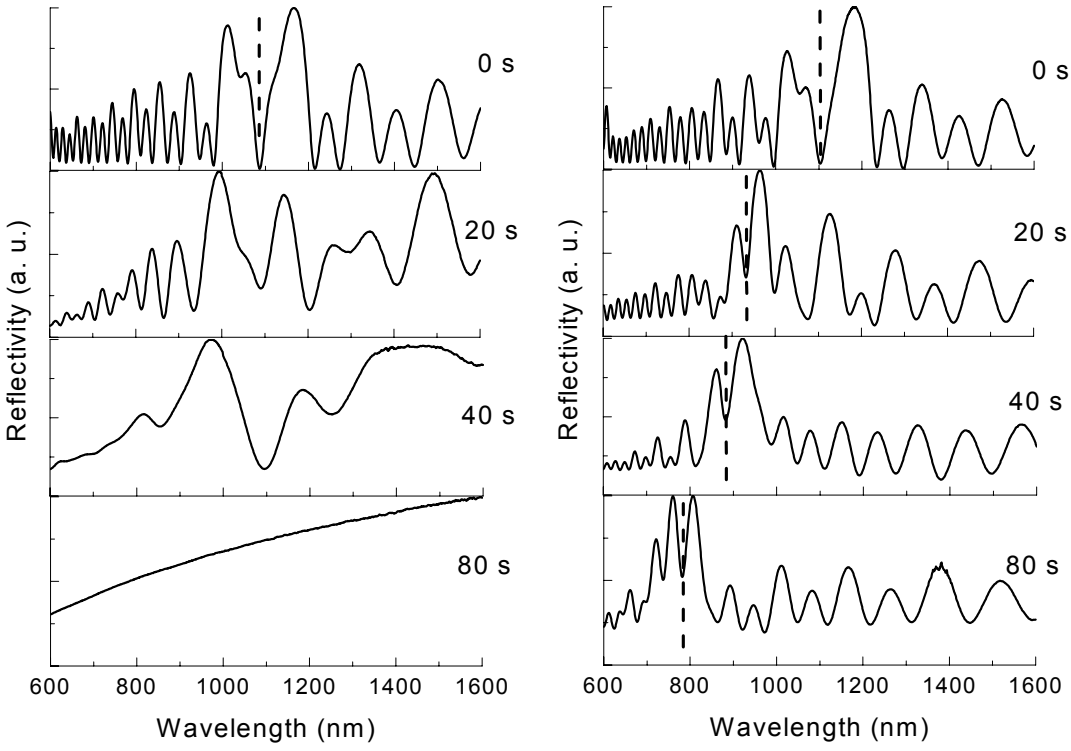

Figure 4.13. Due to the nanodimensions of the hydrophobin layer, these proteins can self-assemble also inside the pores of a thick porous silicon vertical structure such as a microcavity, which results unetchable by the NaOH solution. (a) PSi microcavity not infiltrated. (b) PSi proteins modified microcavity.

The PSMC has been immersed in the solutions for 1 hour and has been analysed each ten minutes: the optical spectrum of the PSMC remains unchanged in all tests. After the basic etch process the hybrid organic-inorganic device still works as a chemical optical transducer: its ability in sensing the vapours of different volatile substances has been proved. In Figure 4.14, the characteristic red-shifts due to the capillary condensation of the vapours inside the nanometric pores of the PSMC are reported. The red-shift, due to

the presence of a single gas, is completely reversible when the gas is replaced by air and the protein coated microcavity can be used after months with different substances giving high reproducible results. The sensitivity of this optical transducer to the refractive index changes has been also calculated by exposing it to substances having different refractive index. Assuming that the four solvents equally penetrates the nanostructured spongy multilayer, a sensitivity of 459 (3) nm expressed in refractive index units was estimated [11].

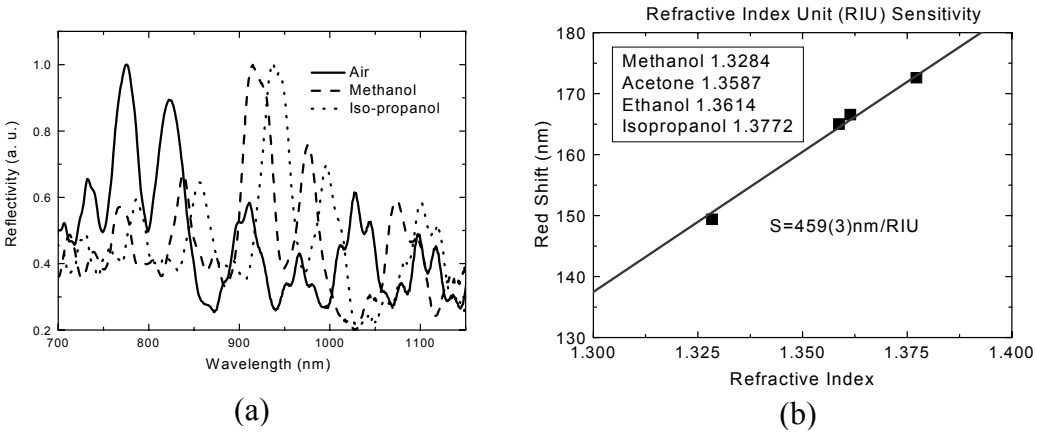

Figure 4.14. The PSi protein modified microcavity still works as optical transducer for vapour and liquid detection. (a) The characteristic red shifts of the optical spectrum on exposure to methanol and isopropanol. (b) Determination of the sensitivity to refractive index changes of the optical transducer.

References

[1] H. J. Hektor, K. Scholtmeijer, "Hydrophobins: proteins with potential", *Current Opinion in Biotechnology* **16**, 434-439 (2005).

[2] H. A. B. Wosten, M. L. de Vocht, "Hydrophobins, the fungal coat unravelled", *Biochimica and Biophysica Acta* **1469**, 79-86 (2000).

[3] G. R. Szilvay, A. Paananen, K. Laurikainen, E. Vuorimaa, H. Lemmetyinen, J. Peltonen, M.B. Linder, "Self-assembled hydrophobin protein films at the air-water interface: Structural analysis and molecular engineering", *Biochemistry* **46**, 2345-2354 (2007).

[4] G. Tompkins, W. A. McGahan, "Spectroscopic ellipsometry and reflectometry", Wiley, New York, 1999.

[5] M. L. de Vocht, K. Scholtmeijer, E. W. van der Vegte, O. M. H. de Vries, N. Sonveaux, H. A. B. Wösten, J. M. Ruysschaert, G. Hadziioannou, J. G. H. Wessels, G. T. Robillard, "Structural Characterization of the Hydrophobin SC3, as a Monomer and after Self-Assembly at Hydrophobic/Hydrophilic Interfaces" *Biophysical Journal* **74**, 2059-2068 (1998).

[6] K. R. Williams, R. S. Muller, "Etch rates for micromachinig processing", *Journal of Microelectromechanical Systems* **5**, 256 (1996).

[7] L. De Stefano, L. Moretti, I. Rendina, A. M. Rossi, S. Tundo, "Smart optical sensors for chemical substances based on porous silicon technology", *Appl. Opt.* **43**, 167 (2004).

[8] R. Wang, Y. Yang, M. Qin, L. Wang, L. Yu, B. Shao, M. Qiao, C. Wang, X. Feng, "Biocompatible Hydrophilic Modifications of Poly(dimethylsiloxane) Using Self-Assembled Hydrophobins", *Chem. Mater.* **19**, 3227-3231 (2007).

[9] R. M. A. Azzam, N. M. Bashara, Ellipsometry and Polarized Light, Elsevier Science Publ. Co., 1 edition (1986).

[10] L. De Stefano, I. Rendina, L. Moretti, A. M. Rossi, "Optical sensing of flammable substances using porous silicon microcavities", *Mater. Sci. Eng. B* **100**, 271-274 (2003).

[11] L. A. DeLouise, P. Meng Kou, B. L. Miller, "Cross-correlation of optical microcavity biosensor response with immobilized enzyme activity. Insights into biosensor sensitivity", *Anal. Chem.* **77**, 3222-3230 (2005).

CHAPTER 5 INTEGRATION INTO A LAB-ON-CHIP AND PATTERNING TECHNIQUES

(Papers J4, J10, J11, J12, J19, J21, J22, P3, P5, P7, P11, P20, P21)

The acronym MOEMS stands for Micro-Opto-Electro-Mechanical-System representing one of the most interesting example of new technologies already available, but applied on micrometric scale. More than a simple collection of micro-devices, the MOEMS science is a new research field that combines the properties and characteristics of different materials with scientific disciplines to find innovative and affordable solutions in fields such as sensing, biotechnology, analytical chemistry. The integration of micro-devices means not only lower costs through mass production, but also an improvement in terms of analysis time, simplicity of use and a decrease in consumption of materials (reagents and analytes, for example) [1]. Generally, a MOEMS includes a microfluidic system used to connect the different elements of the device such as biochemical reaction chambers and micropumps. Lab-on-Chip are the first MOEMS appeared on the market in the late 90's. Now they are expected to be at the basis of the new scientific revolution. Many materials are involved in the Lab-on-Chip fabrication each one with a specific function. The glass is one of the most used in chip sealing through some thermal or mechanical techniques. The anodic bonding is a standard IC fabrication technique which is widely used in microfluidic due to a wide spectrum of advantages among which the hermetic sealing [2-3]. Due to the good bonding quality, glass transparency, technological cleanness and high passivity to most of chemicals and biological substances, anodic bonding is commonly exploited in the fabrication of microsystems such as MOEMS or Lab-on-Chip. Another important fabrication process employed in most microsystems is the photolithography, used to transfer patterns of geometric shapes on the circuit.

In this chapter, different examples of integrated systems joining together typical microelectronic fabrication technologies with the PSi optical transducer features are reported. It is also exploited the Direct-Laser-Writing on PSi surface as alternative patterning process to the traditional photolithographic approach.

5.1 Silicon Glass Anodic Bonding

Anodic bonding (AB) [4-7] is widely used for bonding glass wafers to other conductive materials due to the good bond quality. The deterministic parameters for AB process include applied voltage, temperature, bonding time and nature of the surfaces to be bonded. Nevertheless, the AB conditions can cause electrical damages, when bonding wafers with integrated circuits on board, or mechanical damages when bonding silicon wafers with thermally mismatched materials like piezoelectric lithium niobate ($LiNbO_3$), especially important for MOEMS. In presence of PSi, the major problem can be a strong oxidation of the material causing a partial or complete pores filling by thermal oxide. This can cause an inactivation of the porous sensing region and a degradation of the optical response of the whole structure. For this reason a preliminary characterization of the typical silicon-glass AB parameters has been performed to investigate low temperature, low voltage and short time, taking into account the electrode type and thickness of glass wafers. In preliminary experiments, 2-in crystalline silicon wafers with no porous layer on their top were used. The glass wafers were 2-in, Borofloat 33 type, 1 mm and 2 mm thick. Silicon wafers were prepared by standard wet cleaning process based on RCA rule, referred in literature as good method for contact angle reduction [8].

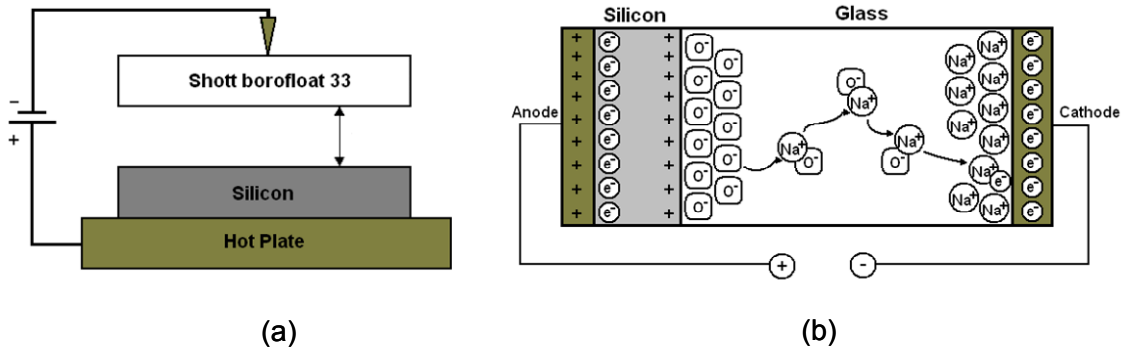

Figure 5.1. (a) Schematic of the system used for the silicon glass anodic bonding. (b) Reaction scheme between silicon and glass.

The glass wafers were prepared by using acetone, $K_2Cr_2O_7$ and isopropanol. A final treatment in H_2O_2 was performed for both silicon and glass wafers for hydrophilic surface formation. Two different electrodes were employed for applying voltage, single point (tip shaped) and planar electrode (circular shaped, 10 cm diameter). The first one

was placed approximately in the central region of the wafer while the planar electrode covered the whole wafer surface. AB of silicon and glass was investigated in the temperature and voltage range of 200-400 °C and 0.2-2.5 KV, respectively.

A scheme of the system used for the silicon-glass anodic bonding is reported in Figure 5.1 (a). The silicon was placed on a hot-plate connected to the anode of a voltage source. Then, the glass was positioned in close contact on the silicon wafer and connected to the cathode of the system. Due to the applied voltage, the sodium ions in the glass drifted toward the negative electrode leaving the oxygen ions free to react with the silicon (Figure 5.1 (b)) so to create Si-O bonds according to [9]:

$$Si\text{-}OH+HO\text{-}Si \rightarrow Si\text{-}O\text{-}Si+H_2O \qquad (5.1)$$

In the case of planar electrode, satisfactory strength and bond quality with high uniformity was obtained at temperatures as low as 200 °C, at voltage of 2500 V, with process times lower than 2 minutes (see Figure 5.2). This is an important and somehow unexpected result: normally AB temperatures are about 350 – 500 °C with times of several minutes.

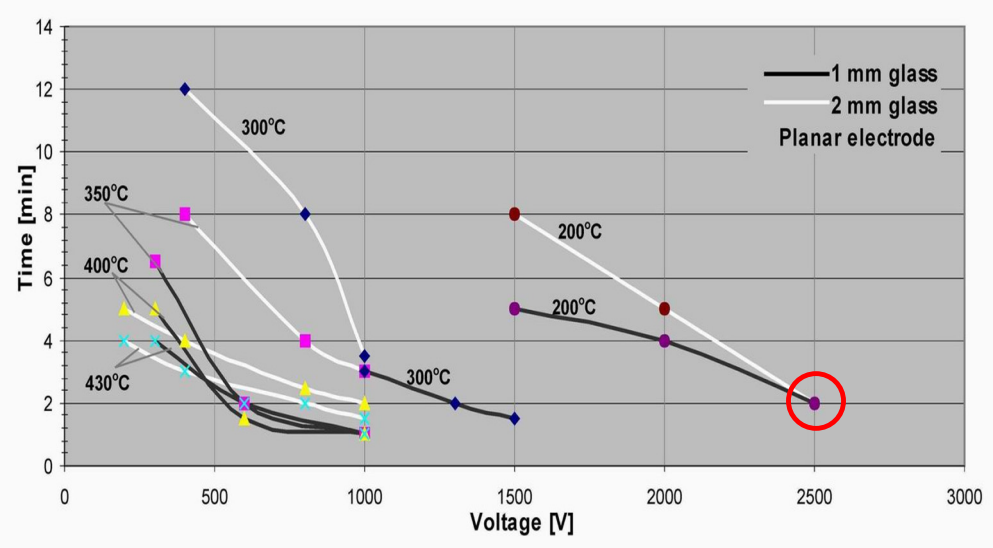

Figure 5.2. Time characteristics of AB versus voltage, with temperature and glass thickness as parameters, for planar electrode.

5.2 Lab-on-Chip based on Porous Silicon-Glass Anodic Bonding

A Lab-on-Chip (LOC) is a device integrating laboratory functions on a single chip of few square centimetres in size. In recent years, there was a fast and intensive interest

about LOC for sensing applications due to several factors such as very limited sample consumption and short analysis time. In this work, the basic element of a Lab-on-Chip, the sensor device, has been obtained integrating the PSi optical transducer and a glass slide, which ensures sealing and the interconnections for fluids inlet and outlet. The cross section of the chip structure is shown in Figure 5.3.

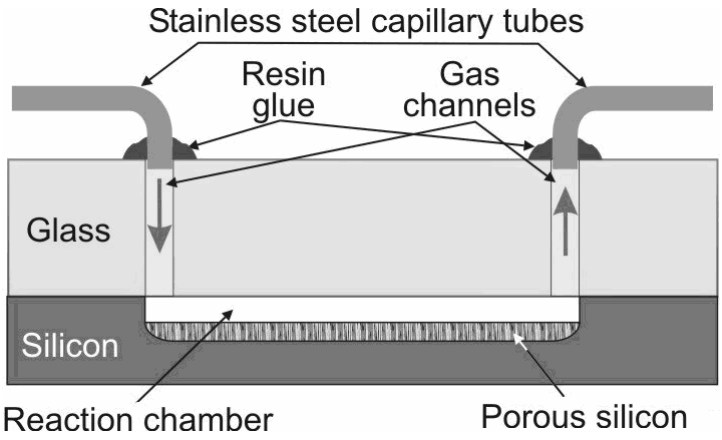

Figure 5.3. Schematic of the sensor device for Lab-on-Chip application.

The reaction microchamber has been realized by a two-step electrochemical etching of the silicon. The first step is the electropolishing of the material obtained by means a high current density electrochemical etch which creates a microwell. The second step is a consecutive electrochemical etch which is used to fabricate the PSi layer on the bottom of the microchamber. The thickness and porosity of the PSi layer were measured by variable angle spectroscopic ellipsometry; the values obtained were about 9.1 μm and 79 %, respectively. The refractive index of the layer has been calculated as 1.34 from the porosity, using the Bruggemann Eq. (2.3). After the mechanical drilling of the flow channels, the glass slide has been cleaned and activated for the AB process following standard RCA and H_2O_2 procedures. Due to the highly reactive PSi nature, the standard cleaning procedures had to be changed with a soft cleaning procedure based on trichloroethylene, acetone and ethanol. The silicon chip has also been carefully rinsed in deionised water for several minutes. Silicon etched wafer and glass top prefabricated components have been anodically bonded together with mutual alignment at a temperature of 200°C, voltage of 2.5 kV and with a process time of 2 minutes. The reflectivity spectra in the VIS-IR wavelength region have been recorded with a very simple experimental set-up: a white source illuminates, through an optical fiber and a

collimator, the porous silicon at nearly normal incidence. The reflected light is collected by an objective and coupled into a multimode fiber. The signal is sent to an optical spectrum analyzer (Ando, Mod. AQ-6315B) and measured with a 0.1 nm resolution. Time-resolved measurements have been also performed in order to characterize the sensor dynamic: using the laser beam from an IR source, the signal of a receiving photodetector before, during and after the exposure to acetone has been measured as a function of time. In Figure 5.4 the reflectivity spectra of the device, unperturbed and on exposure to vapors of different organic compounds, are reported. As it can be seen, on exposure to compounds, due to the phenomenon of capillary condensation, the average refractive index of the layer increases, and, as a consequence the optical thickness of the porous silicon layer also increases.

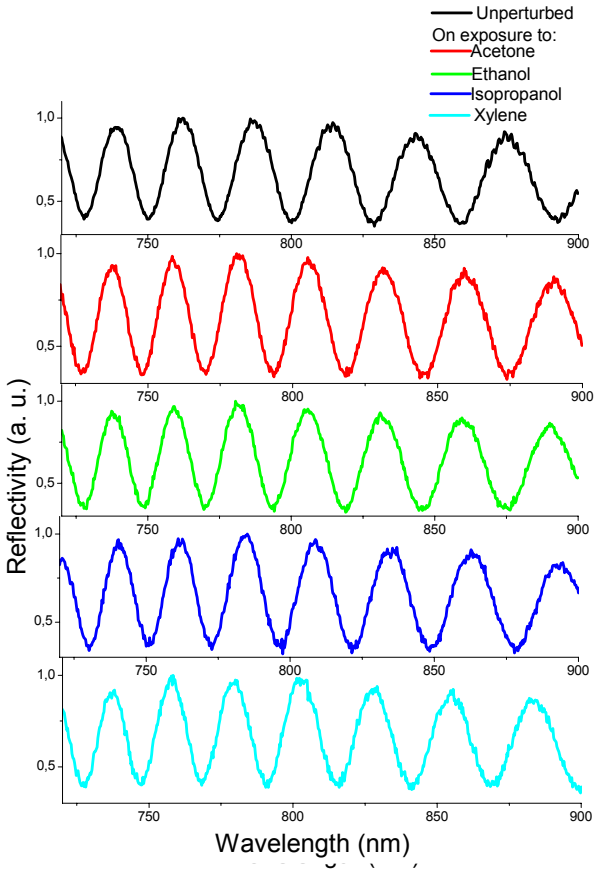

Figure 5.4. Reflectivity spectra of the unperturbed sensor and on exposure to vapors of several organic compounds.

In Figure 5.5 the maxima of order *m* as function of wavenumber are shown; the slopes of the lines give the optical thickness of the layer for each substance. In the wavelength range considered, the assumption of a refractive index independent on the wavelength is satisfied since the PSi refractive index changes less than 2 % in this interval.

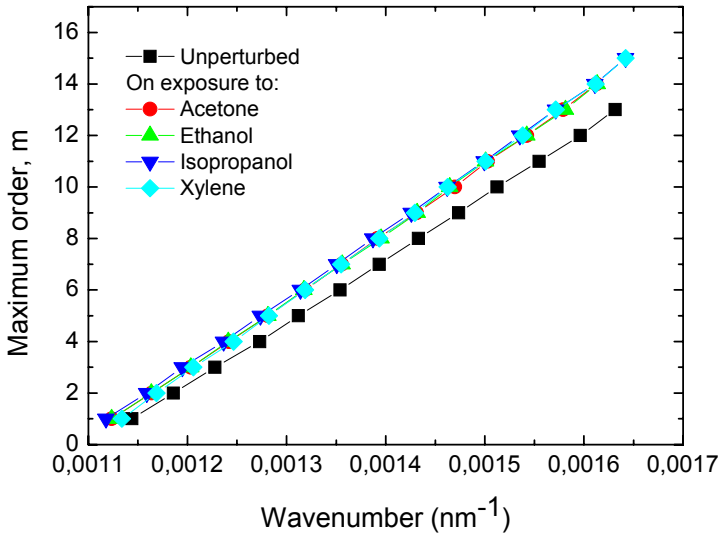

Figure 5.5. Maximum *m*-order as function of wavenumber ($1/\lambda_m$). The slopes of the straight lines are the optical thicknesses of the unperturbed layer and on exposure to the vapors.

Table 5.1. Chemical organics substances used in sensing experiments and some relevant physical-chemical properties [a].

Chemical compounds	*n*	*ρ* (g/cm^3)	STC (mN/m)	VP (kPa)	BP (°C)	*Δ<nd>* (nm)	LLF
Acetone	1.359	0.791	23.46	30.8	56	1000 (60)	0.23
Ethanol	1.360	0.785	22.8	5.8	78	1010 (70)	0.23
Iso-propanol	1.377	0.785	20.93	6.8	82.4	1040 (60)	0.22
Xylene	1.501	1.454	38.8	0.046	214	1400 (50)	0.22

[a] *n* is the liquid refractive index; *ρ* is the density (@ 25 °C); STC is the surface tension coefficient (@ 25 °C); VP is the vapor pressure; BP is the boiling point; Δ<*nd*> is the average optical path increase and LLF the layer liquid fraction.

In Table 5.1 the average optical path of the PSi layer and the layer liquid fraction (LLF), calculated by using the Eq. (3.2), are reported for each substance. The LLF values are about 30 % lower than ones obtained in the case of the PSi transducer before of the AB process [10]. These differences can be ascribed to a slight oxidation of the porous silicon layer due to the AB temperature process. The silicon oxide can fill or obstruct the very small pores of the sponge-like structure, preventing the liquid to condense into them. Moreover, due to the air present during the AB process, there probably exists an

extra pressure into the microchamber because some air has been entrapped in the PSi matrix. As a consequence, according to the Kelvin Eq. (3.1), the capillary condensation of the liquid phase decreases. The result of time-resolved measurement is compared in Figure 5.6 to the data acquired on the same PSi layer before the AB integration process: it is well evident that, due to chamber miniaturization, the response time (τ_{resp}=2 s), the time interval between the 10% and 90% of the maximum signal, is significantly shorter.

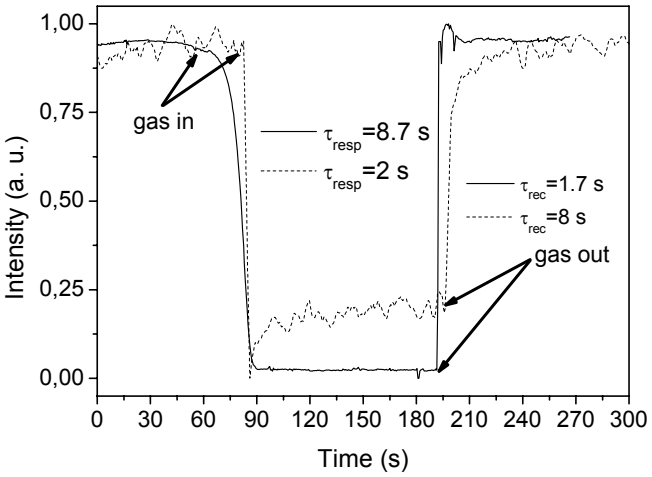

Figure 5.6. Time-resolved measurements of porous silicon layer during the monitoring of acetone in 0.4 l test chamber (solid line) and in the integrated 10 µl micro-chamber (dashed line).

The value of response time depends not only on the physical phenomena involved (i.e., equilibrium between adsorption and desorption in the PSi layer) but also on the geometry of the test chamber and on the measurement procedure, i.e. static or continuous flow mode. In static condition, the response time is mainly determined by the diffusion of the gas into the chamber volume: in fact, when vapor is in contact with the porous silicon surface, the capillary condensation takes place instantaneously [11-12]. For the same reason, the recovery time is longer (τ_{rec}=8 s): as soon as Nitrogen is introduced into the µ-chamber, the conditions for capillary condensation are not still valid so that the liquid phase disappears, depending on atmosphere rate exchange. As it is shown in this graphic, the sensor response is completely reversible.

5.3 Flow Injection Analysis

Flow Injection Analysis (FIA) is a versatile technique to perform quantitative chemical analysis. FIA was invented at Department of Chemistry at DTU in 1975 by Ruzicka and

Hansen [13-14]. Since then more than 15000 research papers appeared in the scientific literature. FIA is based on injecting by a valve of small and well-defined volume of sample into a continuously flowing carrier stream to which appropriate auxiliary reagent streams can be added. The sample disperses and reacts with the components of the carrier in a reactor, forming a species that is sensed by a detector and recorded. A schematic of the Flow Injection Analysis is reported in Figure 5.7.

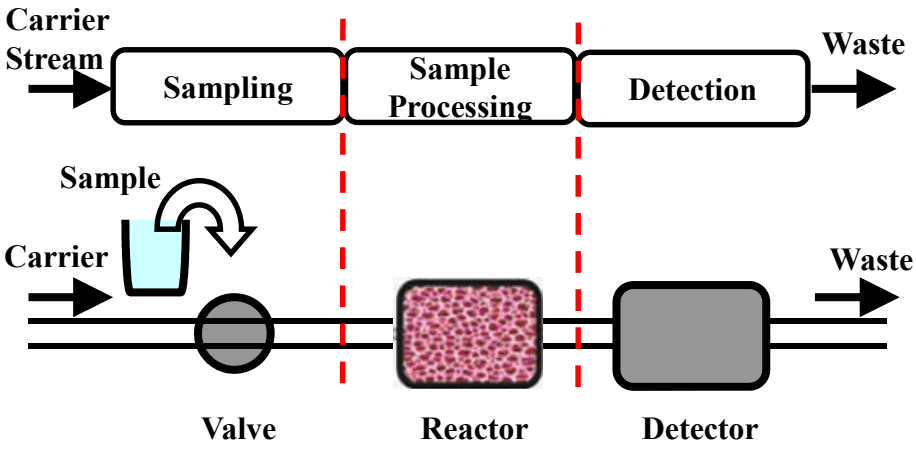

Figure 5.7. Schematic description of the Flow Injection Analysis.

Thus, in contrast to conventional continuous flow procedures, FIA does not rely on complete mixing of sample and reagent. Combined with the inherent exact timing of all events it is not necessary to wait until all chemical reactions are in equilibrium. These feats, which allow transient signals to be used as the readout, do not only permit the procedures to be accomplished in a very short time, but have opened new ways to perform an array of chemical analytical assays, which are very difficult and in many cases directly impossible to implement in a traditional way. Thus, in FIA it is possible to base the assay on the measurement of metastable compounds, which exhibit particularly interesting analytical characteristics. The concept of FIA depends on a combination of three factors: reproducible sample injection volumes, controllable sample dispersion, and reproducible timing of the injected sample through the flow system. The system is ready for instant operation as soon as the sample is introduced. FIA offers several advantages in term of: considerable decrease in sample (normally using 10 to 50 μL) and reagent consumption, high sample throughput (50 to 300 samples per hour), reduced residence times (reading time is about 1 to 40 s), shorter

Flow Injection Analysis reaction times (1 to 60 s), easy switching from one analysis to another (manifolds are easily assembled and/or exchanged), reproducibility, reliability, low carry over, high degree of flexibility, and ease of automation [15]. Perhaps the most compelling advantage of the FIA technique is the great reproducibility in the results obtained by this technique that can be set up without excessive difficulties and at very low cost of investment and maintenance. These advantages have led to an extraordinary development of FIA, unprecedented in comparison to any other technique.

5.4 Integrated Pressure-Driver Microsystem for Optical Sensing

The evolution of the system described in section 5.2 is schematized in Figure 5.8 together with the read-out experimental set-up. The main difference between this device and the previous one is the use of the FIA method, that largely improves the performances of the sensor.

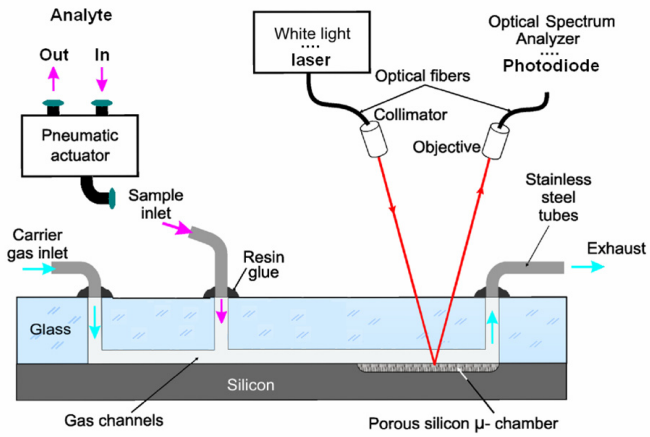

Figure 5.8. Schematic of the complete optical microsystem and of the read-out experimental set-up.

In this system the analyte is sent into the reaction chamber by a carrier stream after the valve opening. The interaction between the analyte and the PSi transducer is monitored by time-resolved optical measurements: a laser beam with 633 nm wavelength was used at nearly normal incidence; the signal of a receiving photodetector before, during and after the exposure to gaseous substances (Isopropanol, Ethanol and Methanol) has been measured as a function of the time. The fabrication of the integrated device was based on three steps as shown in the process flow reported in Figure 5.9. It started with the glass micromachining (Figure 5.9 (a)) in order to realize the channels for the FIA analysis; a glass slab has been patterned and etched by HF/ethanol (3:1) solution

characterized by an etch rate of 30 μm/min. Inlet and outlet channels for feeding gas or liquid substances have been mechanically drilled in the top glass wafer, on the opposite side of the porous region. The microchamber with the PSi on the bottom (Figure 5.9 (b)) has been realized by two steps electrochemical etching as already reported in the section 5.2.

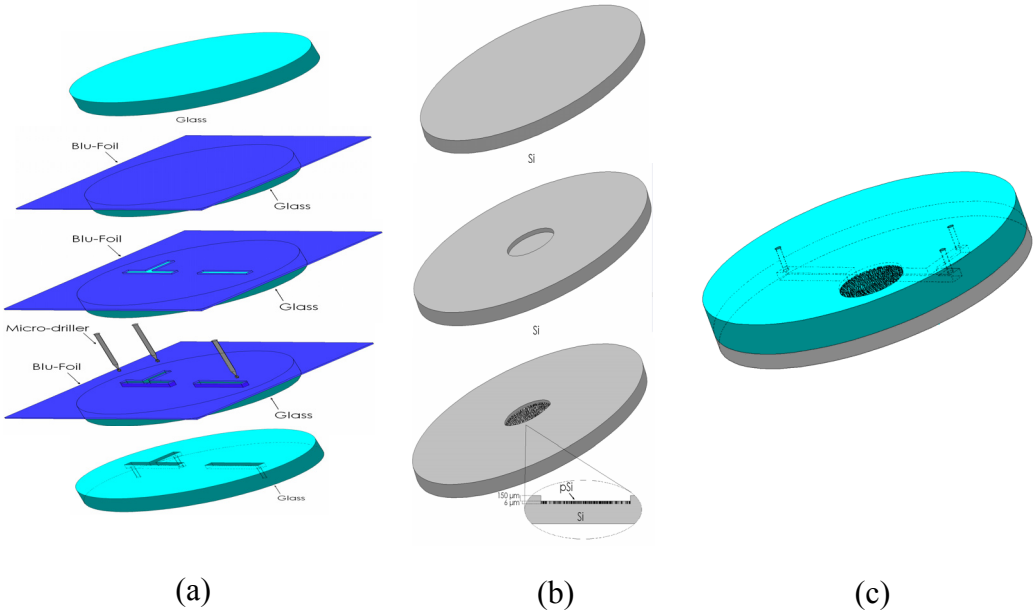

Figure 5.9. Fabrication process flow. (a) Glass micromaching. (b) Silicon micromachining based on two steps electrochemical etching. (c) Silicon-glass anodic bonding.

The last step was the anodic bonding process joining together silicon and glass (Figure 5.9 (c)). By monitoring the changes in the reflectivity spectrum, the valve opening frequency which allows a steady state of the optical response was found; this value was then fixed (100 mHz) for all the measurements. The pressure range for the analyte and the carrier was also investigated. The result of a time-resolved measurement is shown in Figure 5.10, in the case of Isopropanol: a response time, τ_{resp}, has been determined of only 156 ms. The signal returns to its original value in even faster time: τ_{rec} =24 ms. The similar optical microsystem reported in the section 5.2 but realized without using the FIA procedure is characterized by a response time of 2 sec, significantly longer respect to the present result. Using the same experimental conditions, the stability and repeatability of the sensor on several pulses of the gas analyte were also verified. The

response times obtained by exposing the device to other substances have been compared.

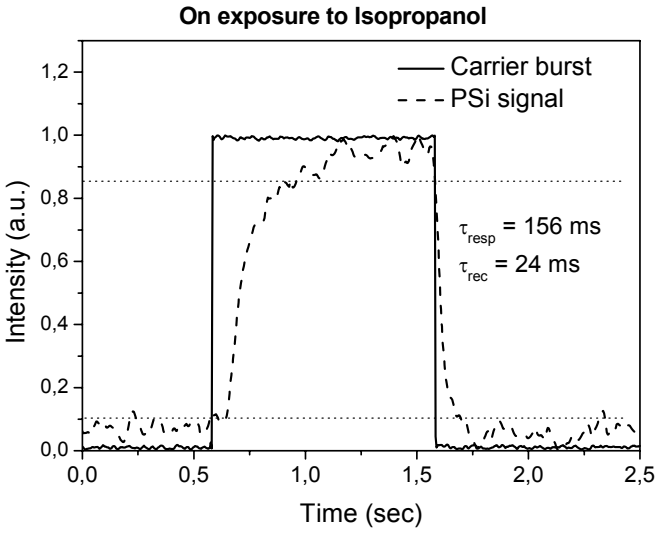

Figure 5.10. Time resolved measurement in case of Isopropanol. The optical response and the time reference of the carrier have been shifted for the sake of clarity. Dotted lines are eyes guide for the 10% and 90% of the PSi signal.

Table 5.2. Comparison between response times due to different substances

VOC	Isopropanol	Ethanol	Methanol
Response time	156 ms	104 ms	64 ms
Dipole	1.66 D	1.66 D	2.87 D

The carrier and analyte pressures have been set so that the microchamber atmosphere was vapor saturated in each case. In Table 5.2 a comparison among the obtained results is reported. The different response times can be attribute to the chemical-physical characteristic of each substance which determines their interaction with the PSi surface. In particular, Methanol has the higher dipole (as reported in Table 5.2) which probably assures its faster penetration and condensation into the pores.

5.5 Patterning technique: Direct Laser Writing

The formation of a porous area on a micro-machined silicon wafer generally requires the definition of a pre-patterned region through the standard photolithography. In this

case two problems could arise: the photoresist mask is effective only for 2-3 min. against the HF solution during the electrochemical process [16] and for longer etching times, a different masking material such as silicon nitride, is needed; then, the photoresist developer, being alkaline, can damage and dissolve the porous silicon. The first proposed alternative technique to the traditional photolithographic approach is direct photo structuring of porous silicon in HF [17]. A non-wet option to the direct patterning process is the Direct Laser Writing (DLW). This is an ablation-oxidation process already used on the PSi surface in order to define channel waveguides [18-19] or oxidized regions for the selective cells growth [20]. Due to the low thermal conductivity of the PSi, the high temperature required for the writing process (about 900° C) can be obtained by a low power laser [21].

5.5.1 Process Characterization

In order to characterize the DLW process, five p^+-PSi layers with different porosities in the range between 45 and 80 % were fabricated.

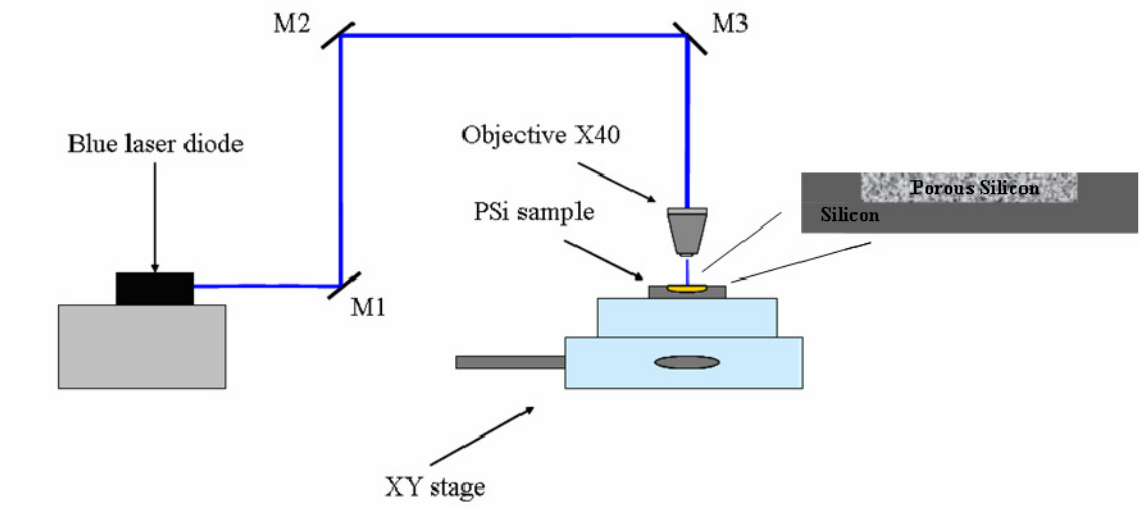

Figure 5.11. Scheme of the experimental set-up: the blue light of a diode laser beam is shaped by a 1 mm pinhole and carried by three mirrors (M1, M2, and M3) onto the sample of PSi placed on a micrometric stage (x-y, resolution 1 μm).

The local laser ablation-oxidation of the PSi layers is a room temperature process, obtained by using the experimental setup schematized in Figure 5.11. The samples, placed on a motorized x-y micrometric stage (x-y resolution 1 μm; scan speed 0.001-90 mm s^{-1}), have been exposed to a laser diode beam (48 mW @406 nm, spot diameter ≈ 1.5 mm) at normal incidence, focused by a 40 x microscope objective lens (NA=0.65).

A pinhole, 1 mm diameter, selected the centre of the laser spot. The focused beam had a quite homogenous spot with a 1 μm diameter and a power of 38 mW just before the surface to be oxidized. Changing the scanning speed of the beam, the laser energy densities ranged between 38 mJ/mm^2 and 3.8 J/mm^2.

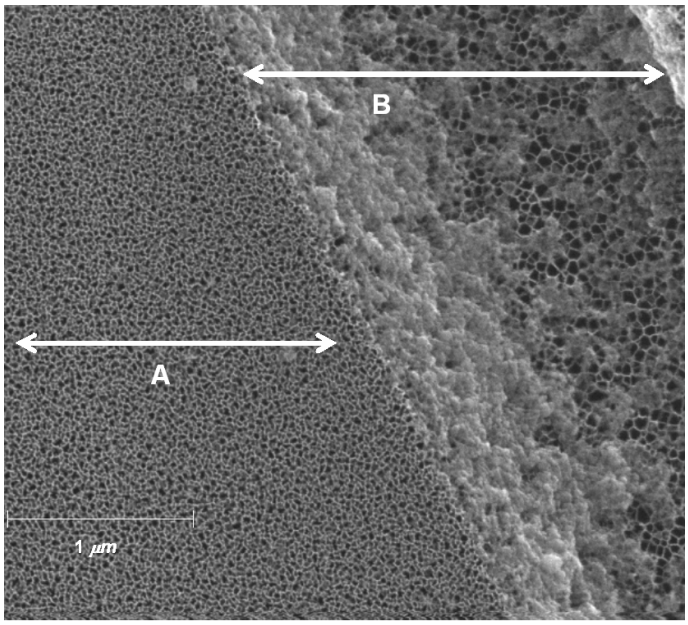

Figure 5.12. Scanning electron micrograph top view of the laser oxidized region on the PSi layer (P=72%): (A) almost oxidized porous silicon surface; (B) channel ablated by laser light at 3.8 J/mm^2.

The optical characterization of the oxidized area by variable angle spectroscopic ellipsometry required the fabrication of an oxidized area large enough to match the size of the ellipsometer micro-spot (about 150 μm). This zone has been obtained by multiple adjacent irradiations with equal laser energy density. Ellipsometric measurements were performed at an incidence angle of 65°, in the 370-850 nm wavelength region with 1 nm spectroscopic resolution. The morphology of the PSi layers was also investigated by scanning electron microscopy (SEM) (Tescan Mira). The presence of Si-O-Si bonds due to the oxidation process has been monitored by means of infrared spectroscopy with a Fourier transform spectrometric microscopy (FT-IR) (Nicolet Continuum). Spectra were obtained at a 4 cm^{-1} resolution averaging 200 scans.

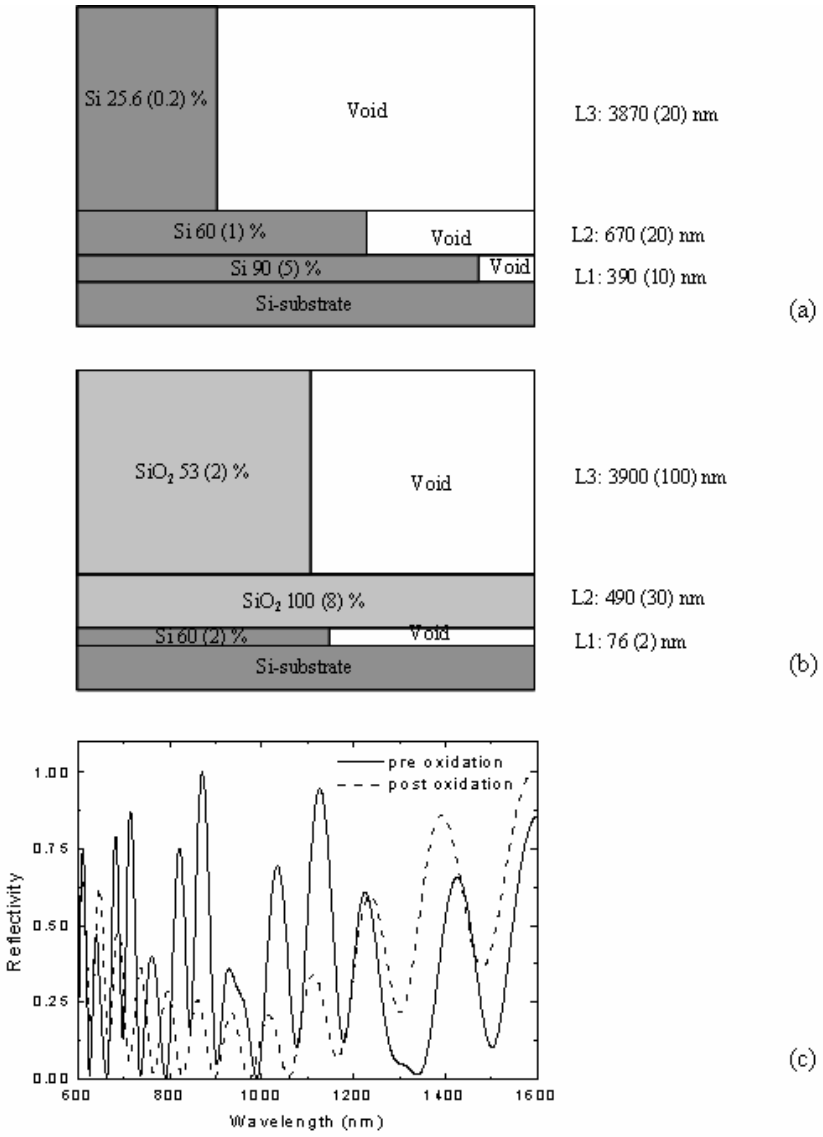

Figure 5.13. The three-layer model used in the ellipsometric analysis of the PSi sample (P=72%) before (a) and after (b) the local laser oxidation; (c) the reflectivity spectra of the two samples calculated from ellipsometric measurements.

On some samples, the oxidized regions were removed by rinsing the PSi layers in a low concentration HF-based solution for 10 sec. The depth of the grooves has been measured by a profilometer (KLA-TENCOR P15) with a vertical resolution of 1 nm and a horizontal resolution of 1 μm. Even if the optical power density used in this experiment was quite high with respect to the other values reported in literature [18, 22], any light sculpturing effect of the PSi surface was not found for scan speed faster than 10 mm/s, corresponding to a fluence lower than 3.8 mJ/mm^2. In Figure 5.12 the

SEM top view of the laser oxidized region at 3.8 J/mm^2 on the PSi layer with a porosity of 72 % is reported.

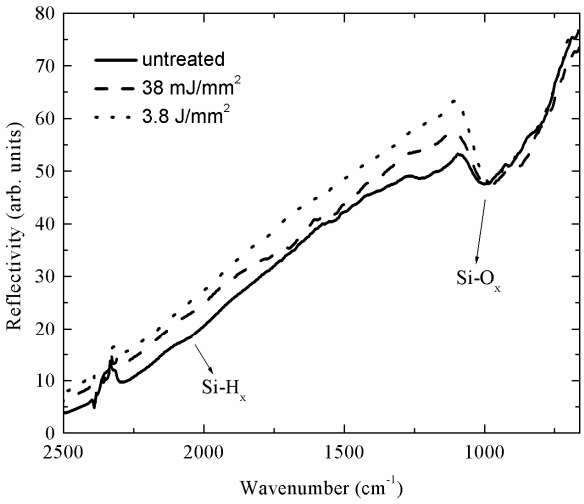

Figure 5.14. FT-IR spectra of the PSi layer (P=72%) before (solid line) and after laser irradiation with 38 mJ/mm2 (dash line) and 3.8 J/mm^2 (dot line).

Two distinct zones are shown: the oxidized surface (A) can be easily recognized by the presence of very small pores, due to volume expansion accompanying the oxidation process. The second one (B) is an ablated strip, 2 μm broad and approximatively 0.5 μm deep, observed in the superficial area where the temperature profile, induced by the beam shape, exceeds the melting point of the PSi. The presence of this ablation has been also revealed by profilometric measurements. In this region the vertical distribution of the silicon oxide down to the first porous silicon layer is visible too. The asymmetry of the laser induced effect in the (A) and (B) zones can be attributed to a slight distortion of the beam profile and – consequently – to the asymmetric temperature distribution on the PSi surface. Ellipsometric measurements confirm the bulk structuring of the PSi surface after the ablation-oxidation treatment. To fit the ellipsometric data, a three EMA (Effective Medium Approximation) layer model was used since the porosity of the PSi structure decreases towards the Si-substrate [23]. Figure 5.13 shows the three-layer model for the sample before (a) and after (b) the local ablation-oxidation together with the reflectivity spectra of both samples (c); the thickness (in nm) and the material content (%) of each layer are reported with the respective errors (in brackets) calculated by fitting the experimental data of the ellipsometric measurements. Before the oxidation, each EMA layer consists of silicon and void; the total thickness of the

structure is about 5 μm. After the oxidation, the silicon in the sample is almost completely replaced by SiO_2 (Figure 5.13 (b)), and the porosity is reduced on average to approx. 50%. The thermal oxide, due to the local irradiation by high optical density, not only grows in the silicon nanocrystals, but also in the pores with a volume ratio 2:1, so that the smaller pores can be completely filled by the oxide resulting in a homogeneous silica layer as evidenced by the ellipsometric results of Figure 5.13 (b).

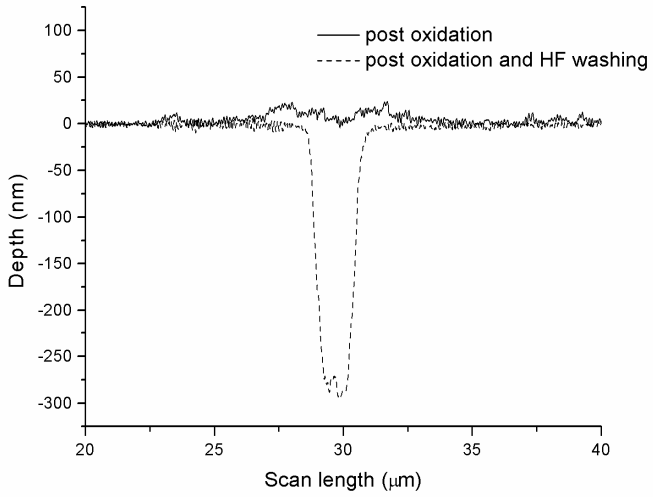

Figure 5.15. Profilometer analysis of the oxidized strip on the 60% porosity sample before (solid line) and post (dash line) the HF removal.

The reflectivity spectrum is calculated from the measurements of the standard ellipsometric parameters [24], the irradiated sample (dashed curve in Figure 5.13 (c)) is blue shifted with respect to the fresh sample (continuous curve in Figure 5.13 (c)): the optical path (*nd*, where *n* is the refractive index and *d* the layer thickness) in the fresh sample is 8455 nm, while it is 5687 nm in the irradiated sample. As soon as the superficial layer is irradiated, it becomes transparent to the laser light, thus avoiding any further heating so that the process is self-stopping. This effect is due to the very low thermal conductivity of the porous silica and also to the high reflectivity interface at the boundary between the porous silica and the porous silicon which causes the line width to be weakly dependent on the laser fluence, while it strongly depends on the layer porosity. The oxide growth has also been monitored by FT-IR measurements. The FT-IR spectra of the PSi layer, before and after the laser irradiations, at two different energy densities, are shown in Figure 5.14. It was verified, as already reported by Rocchia and co-workers [25], the decreasing of the Si-H_x bands intensity (at 2100 cm^{-1}) and the

presence of stronger Si-O_x peaks (1000-1100 cm^{-1}) in the PSi FT-IR spectra by increasing the laser energy densities. This effect has been measured by calculating the peak area of the silicon oxide grown on the surface of the sample with 72% of porosity at different laser fluences. In the case of PSi as-etched, a value of 3800 counts cm^{-1} was obtained, after irradiation by an energy density of 38 mJ/mm^2 the peak area becomes 4200 counts cm^{-1}, and for a 3.8 J/mm^2 laser fluence 5300 counts cm^{-1} were measured, thus confirming the expansion of the oxide in the PSi layer as the delivered light energy increases. In Figure 5.15, the vertical profile of the oxidized strip obtained on the 60 % porosity sample with a fluence of 3.8 J/mm^2 before (solid line) and after (dash line) HF removal was reported. Before the HF washing, the strip shows an irregular shape: a 4 nm large groove is confined between two margins 20 nm high, due to the mechanical and thermal strain, as observed in previous works about the laser oxidation of silicon on insulator [26, 27]. After the HF rinsing, the local oxide is completely removed, and a 3 μm large and 280 nm deep V groove appears. By repeating this measurement on the other samples, it was found that the oxidation depth t_{ox} increases with the porosity and the absorbed laser energy densities.

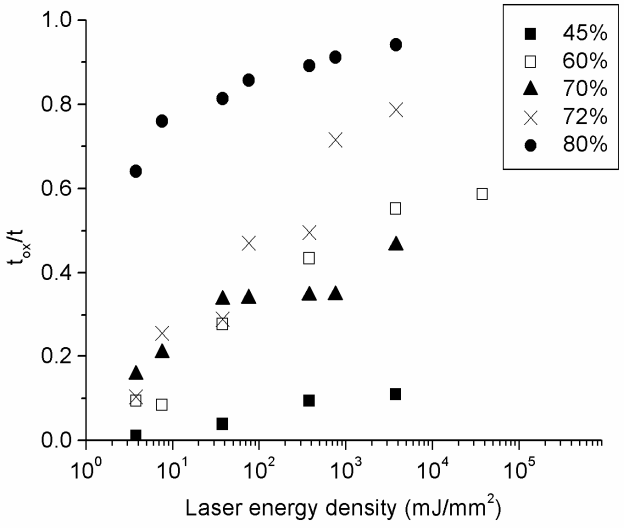

Figure 5.16. Ratio between the oxidized depth t_{ox} and the PSi thickness t vs the laser fluence for different starting porosities.

In particular, for the lowest porosities (45 and 60%) t_{ox} shows a rapid saturation with the laser fluence, reaching 0.3 μm for the deepest strip obtained. In this regime of porosity, there is probably a competition between thermal oxidation and photo oxidation. The behavior is different for the higher porosities, where t_{ox} continuously increases within

the explored laser fluence range. Figure 5.16 shows the ratio between the oxidation depth t_{ox} and the total film thickness t. The rate of this process increases with the porosity, so that the sample at 80% porosity is almost totally oxidized at the average energy density used. The penetration of the laser light in the PSi bulk is favored in high porosity structures. This is also confirmed by the value of $1/\alpha$ which is the light penetration depth, estimated by the ellipsometer measurement @ 406 nm on the fresh material. The $1/\alpha$ coefficient value increases with the porosity: a value of 200 nm for the sample at 45% was calculated, while the layer with 72% of porosity is characterized by a penetration depth of 2400 nm. The strong dependence of the laser induced ablation-oxidation at higher values of porosity suggests a thermal nature of this phenomenon rather than a pure photo-induced one. Another key factor is the oxygen penetration which is completely inhibited by the presence of the oxidized layer where pores have been filled by the oxide expansion. An important issue of a patterning process is represented by its repeatability: it was experimentally verified that for a given sample porosity and a fixed laser power the grooves obtained are perfectly identical, so that it's possible to predict the oxidation depth in the device design phase. Nevertheless, some substantial differences can arise if the process is used on aged samples: the spontaneous oxidation of the porous silicon surface makes the laser oxidation less effective and the geometrical features of the grooves could be different even on the same surface if light was etched on different days. There is also a good repeatability in twin samples on condition that they are processed on the same day.

5.5.2 Bragg Grating Waveguide

The DLW process has been used to etch a high order Bragg grating on a PSi waveguide, obtaining a resonant structure in the near infrared which has been characterized by end-fire coupling. Bragg grating optical filters photoinduced in waveguides are cost-effective devices for applications in optical networks, waveguide lasers, and optical sensors. Bragg gratings in silica planar waveguides increase the versatility of planar lightwave circuits which already have the advantage of being compatible with well-established semiconductor processing technologies. Lot of photonic devices — such as wavelength division multiplexers, photonic beam-formers, external-cavity lasers and optical sensors that measure surrounding refractive index — all benefit from the incorporation of Bragg grating technology [28]. One of the challenges for devices with integrated Bragg gratings is the easiness of their fabrication, but also the regularity of

their geometrical features. It is important to underline that even if some submicrometer gratings have been fabricated on PSi surfaces by electron beam (EB) lithography or direct writing, no one of these structures have been optically characterized [19]. Moreover, the DLW requires much simpler and less expensive equipment with respect to the EB.

The PSi-based Bragg grating waveguide (BGW) fabrication flow process is reported in Figure 5.17. The first step is the electrochemical etching of the crystalline silicon at two different current densities so to realize the PSi waveguide as shown in Figure 5.17 (a). More details on the PSi waveguide fabrication and modal behavior characterization are reported in the section 2.5.4.

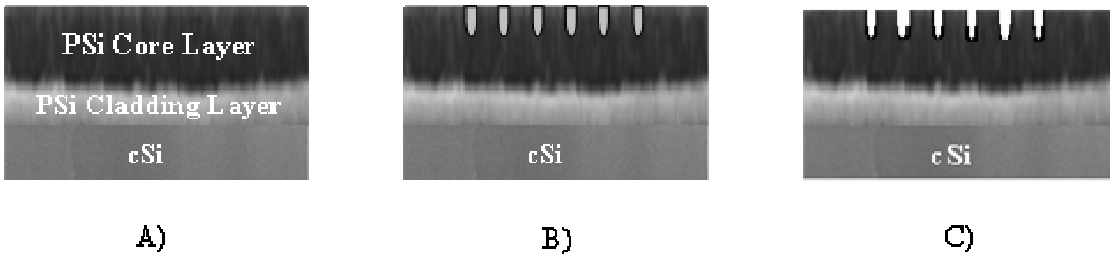

Figure 5.17. PSi based BGW fabrication process flow chart.

After the electrochemical etching, the sample was rinsed in ethanol and dried under a stream of N_2. A fifty periods BGW was written on the porous surface of the upper layer by laser ablation/oxidation (Figure 5.17 (b)). The sample was scanned with a speed of 0.01 mm/s. After the writing process, we removed the oxidized region by rinsing the PSi structure in a low concentration HF-based solution for 10 s, as it is shown in Figure 5.17 (c). The device was then fully oxidized in pure O_2 by a two step thermal treatment (400 °C for 30 min and 900 °C for 15 min). The oxidation strongly reduces the roughness of the interfaces and, as a consequence, the scattering losses of the waveguide [29]. The last fabrication step was the cleaving of the waveguide edges in a direction parallel to the grating in order to allow the measurement of the BGW transmission spectrum by end-fire fiber coupling.

The transmission spectral response of the BGW was registered by end-fire coupling. A sweeping tunable laser source (Ando AQ4321D) was launched into the waveguide by a single-mode lensed fiber; a second fiber collected the light at the end of the device, and sent the signal to an optical spectrum analyzer (Ando AQ6317C) synchronized with the tunable laser source. The spectrum was acquired in the wavelength range of 1520-1620

nm with a resolution of 0.1 nm. In Figure 5.18 (a) and (b) two electronic microscope images of the PSi Bragg grating waveguide after the HF rinsing and the thermal oxidation are reported: Figure 5.18 (a) shows very regular air trenches etched by laser light in the porous silicon surface: the grating pitch Λ is about 10 μm and the duty cycle about 0.7.

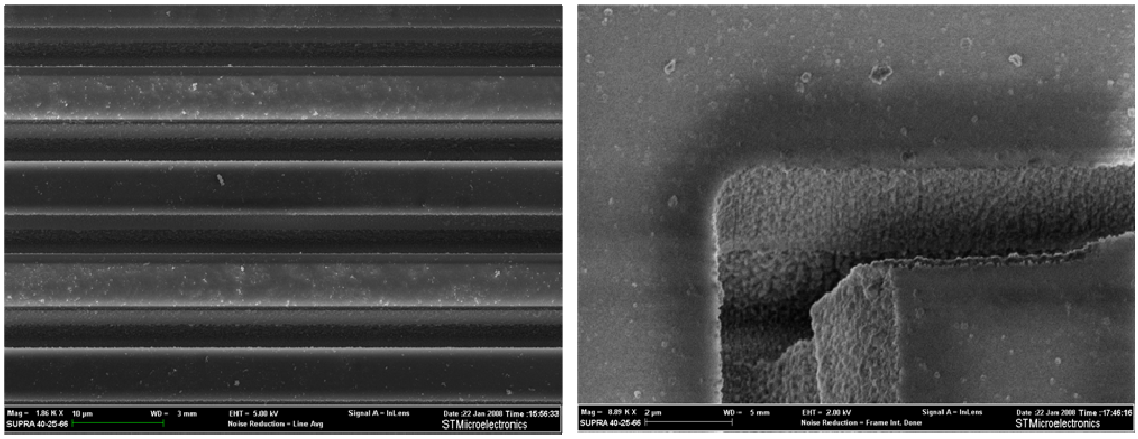

Figure 5.18. (a) SEM top view of the BGW structure. (b) Detail of a single element end.

Figure 5.18 (b) is a detail of a single element end: quite regular walls with a porosity gradient along the vertical direction can be observed. The whole structure is extended on an area of about 0.7 mm^2 and consists of 1.3 mm long straight lines, perpendicular to the propagation direction. The depth profile of the Bragg grating, as measured by the profilometer, is shown in Figure 5.19. The Bragg grating can be considered as a periodic perturbation of the waveguide which forbids the forward propagation of the electromagnetic radiation at specific wavelengths, according to the condition $\lambda_B=2n_{eff}\Lambda$, where λ_B is the Bragg wavelength, n_{eff} the effective refractive index of the mode supported by the waveguide, and Λ the grating pitch. To obtain such optical gap in the near infrared region, the pitch should be of the order of few hundreds of nanometers, close to the resolution of standard technologies used in integrated circuits. The porous silicon walls should also be too thin (about 500 nm) to be safety handled [30]. To overcome these problems, high order Bragg gratings could be considered: in this case the resonance condition becomes $\lambda_B=2n_{eff}\Lambda/k$ where k is an integer called order of the Bragg grating and which represents the number of quarter wavelengths within the air and porous silicon refractive indexes.

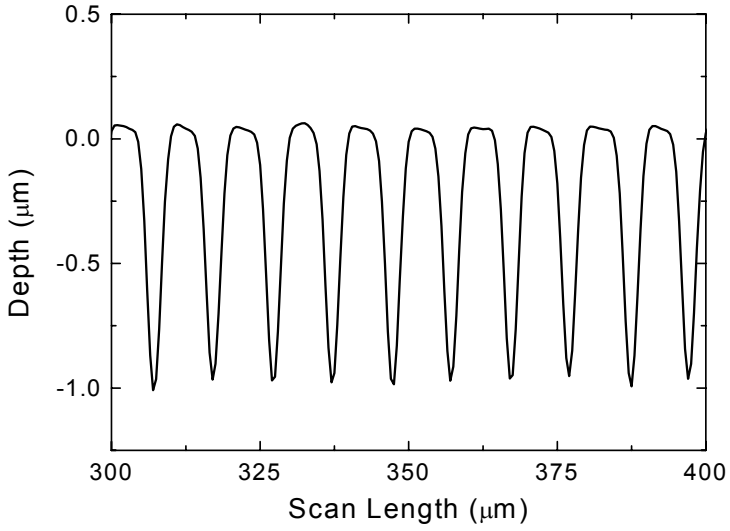

Figure 5.19. Thickness profile of the BGW measured by the profilometer after the HF rinsing.

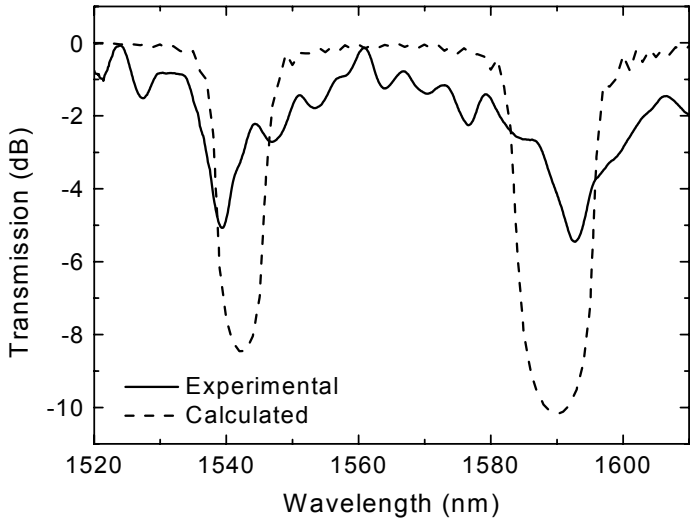

Figure 5.20. Experimental (solid curve) and calculated (dash curve) transmission spectra of the BGW structure.

The transmission spectrum of the resonant structure can be calculated by using the transfer matrix method together with the slab waveguide modal calculation [31]. In Figure 5.20 the experimental (solid curve) and calculated (dash curve) transmission spectra of the PSi BGW are shown: there is a good qualitative agreement between the two spectra. The transmission peaks, present at 1540 nm and 1590 nm, correspond to

the seventeenth Bragg order of the fundamental guided mode and the sixteenth Bragg order of the first guided mode, respectively. The oscillations of the baseline between the two peaks can be attributed to the inner surface roughness and variation of the walls thicknesses due to the DLW fabrication process [32]. The contrast reduction in the transmitted intensity between the numerical and experimental spectra is about 4 dB and due to the scattering losses experienced by the propagating modes in the PSi slab waveguide. The agreement between the spectra is a demonstration of the good control in the fabrication process, suggesting the possibility to use the PSi BGW as optical sensor of biochemical substances and in Lab-on-Chip applications. Even if the optical losses can be reduced by proper design below an acceptable value for telecommunication purposes, for example under 1 dB/cm as reported in the recent literature [18, 33], the ultimate application of such a device can be in the chemical and biological sensing. The easiness and low cost of fabrication, jointly with the morphological features of porous silica, can be the key factors for successful sensor devices.

5.5.3 Chemical Sensing by Bragg Grating Waveguide

The BGW has been characterized as optical sensor for chemical substances. In Figure 5.21 is reported the experimental set-up used for the optical sensor characterization. The device is placed in a test-chamber of about 0.5 x 1 x 1.5 cm^3 equipped with holes for the fibers access, and inlet/outlet gas channels. The experimental setup was in a humidity controlled room (relative humidity 50 % ± 5 %). The transmission spectral response of the BGW was registered by end-fire coupling. The sensor response has been studied on exposure to vapors of different substances changing the concentrations in the case of ethanol and iso-propanol. All the high purity chemicals used were supplied by Sigma-Aldrich. A continuous flow of pure nitrogen carriers the analyte vapors from the tank source into the test chamber; the total gas flow was set to 0.05 sccm. Different gases concentrations on the BGW surface were obtained by diluting in pure nitrogen the organic volatile substance after bubbling. The desired concentration of the considered gas, expressed in the following as volume by volume, has been obtained by properly setting the computer controller (MKS, Type 647C) of the gas flow-meters (MKS, Type 1479A) with a resolution of 0.1 % on the full scale (F. S.) (10 sccm) and an accuracy of ± 1% F. S.

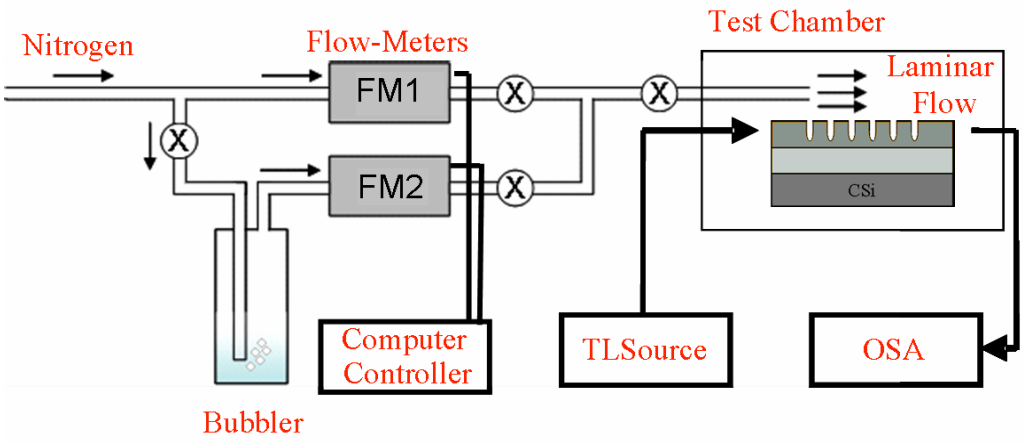

Figure 5.21. Experimental set-up to measure the transmission spectrum of the BGW in nitrogen and on exposure to different vapor substances. TLSource: Tunable Laser Source; OSA: Optical Spectrum Analyzer.

Table 5.3. Analytes used in the sensing experiments. *n* is the refractive index, VP is the vapor pressure, Δλ the experimental peak shift and LLF the estimated layer liquid fraction.

Analyte	*n*	VP (KPa)	Δλ (nm)	LLF
Methanol	1.329	16.9	4.2	0.015
Ethanol	1.360	5.8	5.5	0.018
Iso-propanol	1.377	6.8	7.4	0.023

When the vapors of the chemical substances penetrate into the sponge structure of the PSi BGW, the analyte molecules condense into the liquid phase, due to the capillary condensation phenomenon, and substitute the air in the PSi pores inducing an increasing of the waveguide refractive indexes. In Figure 5.22 (a) is reported the transmission spectrum of the structure in nitrogen and on exposure to different atmospheres of methanol, ethanol and iso-propanol. The largest spectral shift is observed for the iso-propanol, the analyte with the highest refractive index value (see Table 5.3). Each volatile compound determines a different shift of the Bragg peak so that the resonant device can be used to quickly recognize pure substances. The red shift of the BGW transmission peak as a function of the refractive index of each substance is shown in Figure 5.22 (b). In the linear region of the sensor response, the sensitivity was calculated as the slope of the curve obtaining a value of (63±12) nm/RIU (Refractive

Index Unit). Since the system is able to detect a peak shift of 0.1 nm, the limit of detection (LOD), is (48±9) x10^{-4} RIU.

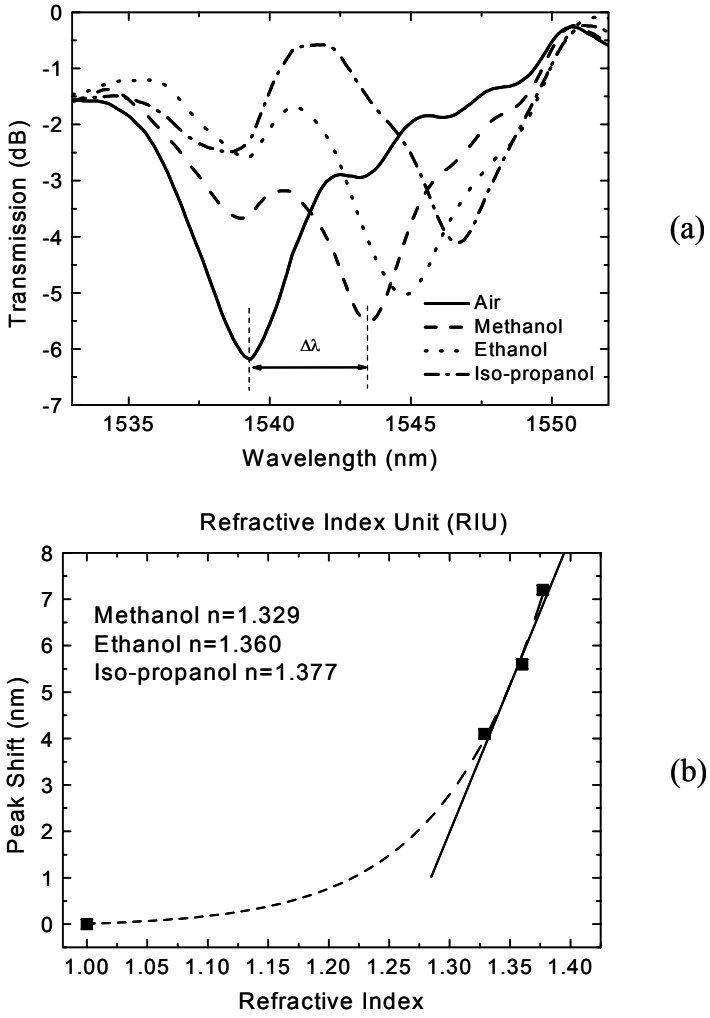

Figure 5.22. (a) Transmission spectra of the BGW on exposure to methanol, ethanol and iso-propanol atmosphere; (b) Shift of the transmission peak vs the refractive index of the organic substances.

Anyway, the relationship between the induced peak shift and the refractive index of the analyte gas is not so straightforward, being also related to the amount of adsorbed substance by capillary condensation which in turn depends on the physical parameters of the gas (surface tension, vapor pressure, and so on) [34]. By applying the Bruggeman effective medium approximation [35], the change in the average refractive index of the PSi waveguide layers as a function of the pore filling for each analyte can be determined. A transfer matrix method [36] can be then used to calculate the

transmission spectrum, assuming that the filling proceeds uniformly into the waveguiding stack [12].

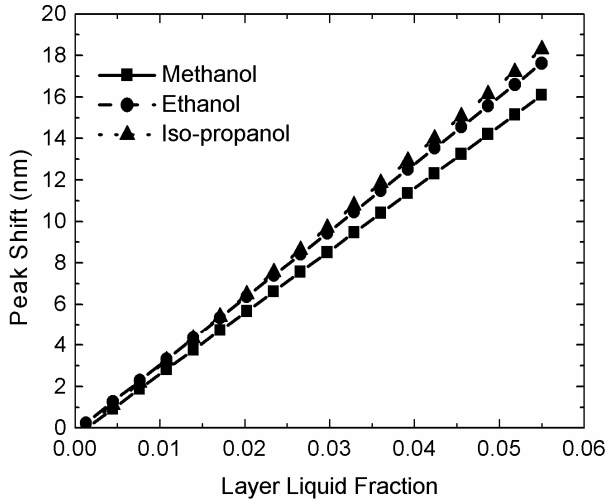

Figure 5.23. Calculated shift of the BGW transmission peak as function of the organic substances condensate fraction.

The Figure 5.23 shows the theoretical peak shift *vs* the Layer Liquid Fraction (LLF), i.e. the pores volume percentage filled by liquid. By comparing these results with the experimental shifts, the LLF of the liquid phase into the silica pores was estimated. The values found are reported in Table 5.3: due to the very low porosity of the cladding and core layers, a small percentage of the pores have been filled by the liquid phase.

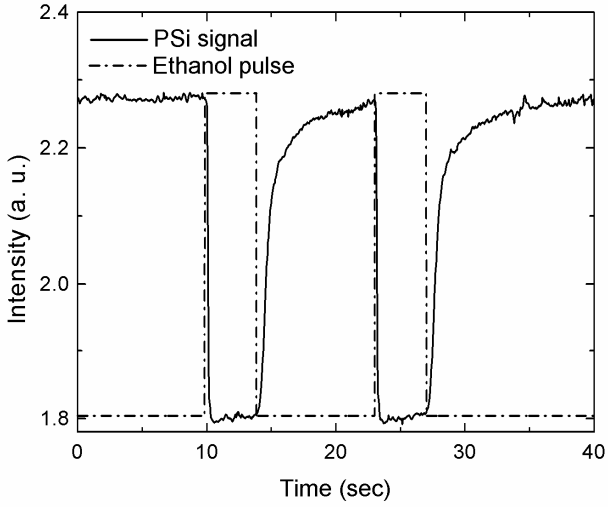

Figure 5.24. Reproducibility and reversibility of the gas sensing measurements in the case of ethanol exposure.

The reproducibility and the reversibility of the gas sensing measurement were verified in the case of an ethanol flow equal to 0.05 sccm. To this aim, the wavelength of the tunable laser source was set at 1545 nm and sent the output signal from the sensor to a photodetector (THORLABS, DET 410) connected to an oscilloscope.

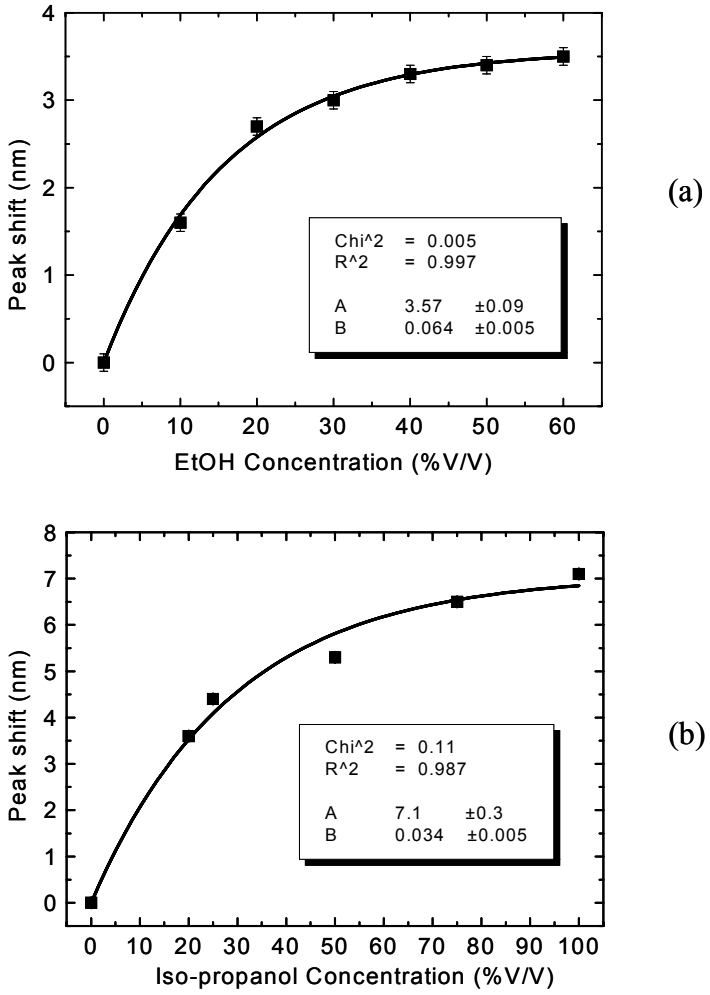

Figure 5.25. Response curves of the optical sensor to different concentrations of ethanol (a) and iso-propanol (b).

The device response was acquired on exposure to several ethanol pulse, 4 s long. The result of the time-resolved measurement is shown in Figure 5.24: the effect is reproducible and reversible. A response time of 0.3 s and a recovery time of 3 s can be estimated, which are faster than those reported for other optical sensor [37]. It also studied the sensor response at different gas concentrations. The experimental results are shown in Figure 5.24 (a) for the ethanol and in Figure 5.24 (b) for the iso-propanol. The peak shift increases with the concentration until the saturation: the experimental data

were fitted with an exponential growth curve $y=A(1-e^{-Bx})$ where A is the amplitude and B is the rate constant. The sensitivities were calculated in the limit of low concentrations $S \approx AB$ obtaining the values S_{EtOH}=0.228 (0.019) nm/%V/V and $S_{Isoprop}$=0.24 (0.04) nm/%V/V. The respective limits of detection are LOD_{EtOH}=1.3 (0.1) %V/V=1000 (80) ppm and $LOD_{Isoprop}$=1.2 (0.2) %V/V=700 (100) ppm, in both cases of the same order of the Threshold Working Limit (ethanol TWL= 1000 ppm; iso-propanol TWL=500 ppm) established by the actual legislation [38]. Due these experimental performances the PSi BGW sensor can be used as an alarm device in industrial applications.

References

[1] A. Chandrasekaran, A. Acharya, J. L. You, K. Y. Soo, M. Packirisamy, I. Stiharu, A. Darveau, "Hybrid integrated silicon microfluidic platform for fluorescence based biodetection", *Sensors* **7**, 1901-1915 (2007).

[2] B. Puers, E. Peeters, A. Van Den Bossche, W. Sansen, "A capacitive pressure sensor with low impedance output and active suppression of parasitic effects", *Sens. Actuat. A* **21-23**, 108-114 (1990).

[3] E. Obermeier, Proc. Semiconductor Wafer Bonding, Science, Technology and Applications. Electrochem. Soc, 212-220 (1995).

[4] Cozma, B. Puers, "Characterisation of the electrostatic bonding of silicon and Pyrex glasses", *J. Micromech. Microeng.* **5**, 98-102 (1995).

[5] J. Wei, H. Xie, M. L. Nai, C. K. Wong, L. C. Lee, "Low temperature wafer anodic bonding", *J. Micromech. Microeng.* **13**, 217–222 (2003).

[6] A. Hanneborg, M. Nese, H. Jakobsen, R. Holm, "Silicon-to-thin film anodic bonding", *J. Micromech. Microeng.* **2**, 117-121 (1992).

[7] T. Rogers, J. Kowal, "Selection of glass, anodic bonding conditions and material compatibility for silicon-glass capacitive sensors", *Sensors and Actuators A* **46/47**, 113-120 (1995).

[8] K. Hermansson, U. Lindberg, G. Palmskog, *Electrochem. Soc. Fall Mtg, Proceed.*, 91-92 (1991).

[9] U. Gosele, Q.-Y. Tong, "Semiconductor wafer bonding", *Annu. Rev. Mater. Sci.* **28**, 215-241 (1998).

[10] L. De Stefano, I. Rendina, L. Moretti, A. M. Rossi, S. Tundo, "Smart optical sensors for chemical substances based on porous silicon technology", *Applied Optics* **43/1**, 167-172 (2004).

[11] P. Allcock, P. A. Snow, "Time-resolved sensing of organic vapors in low modulating porous silicon dielectric mirrors", *J. Appl. Phys*. **90,** 50525057 (2001).

[12] L. De Stefano, L. Moretti, I. Rendina, A. M. Rossi, "Time-resolved sensing of chemical species in porous silicon optical microcavity", *Sensor and Actuators B* **100**, 168-172 (2004).

[13] J. Ruzicka, E. H. Hansen, "Flow Injection Analysis. Part I. A new concept of fast continuous flow analysis", *Analytica Chimica Acta* **78**, 145-157 (1975).

[14] J. Ruzicka, E. H. Hansen, Flow Injection Analysis, 2nd Edition, Wiley & Sons Inc., New York, USA (1998).

[15] M. Valcorcel, M. D. Luque de Castro, Flow-Injection Analysis. Principles and Applications, Ellis Horwood Ltd., Chichester, West Sussex, UK (1987).

[16] Y. Tao, M. Esashi, "Local formation of macroporous silicon through a mask", *J. Micromech. Microeng.* **14**, 1411-1415 (2004).

[17] G. Lerondel, R. Romestain, J.C. Vial, M. Thonissen, "Porous silicon lateral superlattices", *Appl. Phys. Lett.* **71**, 196-198 (1997).

[18] A. M. Rossi, G. Amato, V. Camarchia, L. Boarino, S. Borini, "High-quality porous-silicon buried waveguides", *Appl. Phys. Lett.* **78**, 3003-3005 (2001).

[19] A. M. Rossi, S. Borini, L. Boarino, G. Amato, "Lateral structuring of porous silicon: application to waveguides", *Phys. Stat. Sol. (a)* **197**, 284-287 (2003).

[20] Y. Khung, S. D. Graney, N. H. Voelcker, "Micropatterning of porous silicon films by direct laser writing", *Biotechnol. Prog.* **22,** 1388-1393 (2006).

[21] V.Y. Timoshenko, T. Dittrich, I. Sieber, J. Rappich, B.V. Kamenev, P.K. Kashkarov, "Laser-induced melting of porous silicon", *Phys. Stat. Sol. (a)* **182**, 325-330 (2000).

[22] M. Juan, J.S. Bouillard, J. Plan, R. Bachelot, P.M. Adam, G. Lerondel, P. Royer, "Soft photo structuring of porous silicon in water", *Phys. Stat. Sol. (a)* **204**, 1276-1280 (2007).

[23] C. Wongmanerod, S. Zangooie, H. Arwin, "Determination of pore size distribution and surface area of thin porous silicon layers by spectroscopic ellipsometry", *Appl. Surf. Sci.* **172,** 117-125 (2001).

[24] R.M.A. Azzam, N.M. Bashara, Ellipsometry and Polarized Light, Elsevier Science Publ. Co., 1 edition (1986).

[25] M. Rocchia, A. M. Rossi, L. Boarino, G. Amato, "Laser local oxidation of porous silicon: a FTIR spectroscopy investigation", *Phys. Stat. Sol. (a)* **202**, 1658-1661 (2005).

[26] R. A. Deutschmann, M. Huber, R. Neumann, K. Brunner and G. Abstreiter, "Direct sub-μm lateral patterning of SOI by focused laser beam induced oxidation", *Micro. Eng.* **48,** 367-370 (1999).

[27] F. Micheli, I. W. Boyd, "Photon-controlled oxidation of silicon", *Appl. Phys. Lett.* **51**, 1149-1151 (1987).

[28] X. Dai, S. J. Mihailov, R. Walker, "Ridge-waveguide-based, polarization-insensitive, Bragg grating refractometer", *Meas. Sci. Technol.* **17**, 1752-1756 (2006).

[29] E. Pap, K. Kordás, G. Tóth, J. Levoska, A. Uusimäki, J. Vähäkangas, S. Leppävuori, T. F. George, "Thermal oxidation of porous silicon: study on structure", *Appl. Phys. Lett.* **86**, 041501 (2005).

[30] G. Barillaro, A. Diligenti, M. Benedetti, S. Merlo, "Silicon micromachined periodic structures for optical applications at lambda = 1.55 μm", *Appl. Phys. Lett.* **89**, 151110. (2006).

[31] H. Kogelnik, Integrated Optics, II ed., T. Tamir Ed., New York: Springer-Verlag (1979).

[32] G. Barillaro, V. Annovazzi-Lodi, M. Benedetti, S. Merlo, "Reflection properties of hybrid quarter-wavelength silicon microstructures", *Appl. Phys. Lett.* **90**, 121110 (2007).

[33] P. Pirasteh, J. Charrier, Y. Dumeige, S. Haesaert, P. Joubert, "Optical loss study of porous silicon and oxidized porous silicon planar waveguides", *J. Appl. Phys.* **101**, 083110 (2007).

[34] L. Moretti, L. De Stefano, I. Rendina, "Quantitative analysis of capillary condensation in fractal-like porous silicon nanostructures", *J. Appl. Phys.* **101,** 024309 (2007).

[35] J. E. Spanier, I. P. Herman, "Use of hybrid phenomeno-logical and statistical effective-medium theories of dielectric functions to model the infrared reflectance of porous SiC films", *Phys. Rev. B* **61**, 10437-10450 (2000).

[36] M. A. Muriel, A. Carballar, "Internal field distributions in fiber Bragg gratings", *IEEE Phot. Technol. Lett.* **9**, 955-957 (1997).

[37] R. Marayanaswamy, O.S. Wolfbeis, eds., Optical Sensors, Springer-Verlag, Berlin Heidelberg (2004).

[38] Italian Ministerial Decree 07/09/2002.

CHAPTER 6 CONCLUSIONS

The realization of PSi devices with attractive sensing features, such as fast response time, high sensitivity and specificity, requires the targeting of at least three objectives: a proper design ability, based on numerical simulations by using a transfer matrix method; a well defined fabrication ability, which implies a good control of the electrochemical process; and, finally, a deep characterization technique such as the sophisticated variable angle spectroscopic ellipsometry. The results shown in this thesis demonstrate that these goals have been achieved: multilayered PSi structures which show complex photonic features such as optical resonances, photonic and fractal band gaps, have been realized. In particular, high contrast Bragg mirrors (n_H= 2.2, n_L= 1.3), narrow peak optical microcavity with high Q factor, and Thue-Morse sequences up to 128 different layers have been fabricated. When compared with the calculated reflectivity spectra, the experimental ones all show a very good agreement.

These photonic structures have been successfully used as optical sensors of biochemical molecules present in both liquid and gaseous substances. The sensitivity in the monitoring of chemical vapours has been correlated to the filling capability of the liquid phase of each substance which condense in the pores, but also to the geometrical characteristic of the PSi structures, thus underlying the most important parameters in the sensor design and fabrication.

Since the sensing mechanism is very specific but not selective, different methods of chemical functionalization of the PSi surface have been studied in order to link bioprobes which naturally show high selectivity in recognise target analytes. Two different examples of biological sensing have been reported: the first one is a monitoring of DNA-DNA hybridization by means of a label-free PSi optical biochip; a limit of detection of 260 nM DNA concentration has been obtained. This value is of the same order with those reported for other optical DNA hybridization sensors realized using more complicated and expensive technologies. In the second case, a sugar binding protein has been covalently immobilized on the PSi surface: the protein-chip complex has been investigated for glucose detection. A sensitivity of 0.034 nm/μM would easily allow the revelation of glucose concentration very close to the amount of the sugar present in the human interstitial fluids, such as lachrymal or saliva. The result suggests the use of the device in the detection of the glucose level in diabetic patients.

From the studies about the interfacing of porous silicon with the organic matter, an innovative biological passivation of the PSi, based on some amphiphilic proteins, the *Hydrophobins*, has been used to modify its surface thus avoiding any chemical treatment. The self-assembled protein biofilm allows to control both the wettability of the material and its resistance against alkaline solutions which rapidly dissolve the PSi. Beside the improved chemical stability, this bio/non-bio interface leaves unaltered the sensing ability of the optical transducer.

The optimization and functionalization of the PSi based optical transducer element is only the first step towards microsystems for sensing application: the step further has been the integration of the PSi sensing elements into a Lab-on-Chip prototype, designed and realized for biochemical analysis and medical diagnostic. Due to the mechanical and chemical characteristic of the nanostrucutred porous material several microelectronic techniques including the Anodic Bonding and the Flow Injection Analysis have been adapted and exploited. The integrated devices have been characterized as fast sensors of chemicals compounds. The integration of the PSi in a microsystem strongly reduce the response times, down to 100 ms or even less, as shown by time-resolved measurements. The sensor response dynamic has been characterized demonstrating a sensing effect completely reproducible and reversible. Moreover, the response time is different for different substances as it happens in chromatographic instruments: this is a clear evidence that PSi device could be the fundamental element of an all-optical chromatograph for gaseous or liquid complex mixtures.

Since PSi production is not completely compatible with standard lithography, which uses massively alkaline developers, the Direct-Laser-Writing on the PSi surface, as alternative process to the traditional photolithographic patterning, has been exploited. This powerful technique has been used to fabricate different microstructured devices, not all shown in this thesis, having different functionalities. In particular, a PSi Bragg grating waveguide with a pitch of 10 μm and resonant in the near-infrared wavelength region has been realized and characterized on exposure to volatile organic compounds. Limits of detection of hundred of ppm were estimated from the experimental data, suggesting to use the sensor as an alarm device in industrial applications.

So many interesting experimental results obtained and presented in this PhD thesis work confirm that PSi is a very promising and versatile platform for the fabrication of the so-called smart sensors and biochips due to its peculiar physical-chemical properties and

morphology: just quoting a very celebrate phrase of R. Feynman “...there is still plenty of room at the bottom” of the PSi pores!

APPENDIX A BOTTOM-UP APPROACH TO MICROOPTICS: BIOPHOTONICS IN *MARINE DIATOMS*

(Papers J16, J25, P2, P8, P13, P22)

Diatoms are microalgae with a peculiar cell wall made of amorphous hydrated silica valves, reciprocally interconnected like a Petri dish in a structure called "frustule". The valve surfaces exhibit specie-specific patterns of regular arrays of holes, called "areolae". More than 100000 types of diatoms have been discovered and classified by different shapes of their cell walls. Diatoms could be divided in two major classes on the base of their geometrical symmetries: the centric diatoms, having circular symmetry, and the pennate diatoms with anisotropic shape. Due to their peculiar structures and large variety of morphologies [1], a widespread interest about diatoms and their possible use in nanosciences and nanotechnology has growth. Some futuristic applications have already been proposed and realized: the silica cells of diatoms, with their different geometries, can be exploited in nanopatterning for the fabrication of photonic devices as an alternative to the traditional lithographic techniques [2]. The surface of the diatom structure has been used for the deposition and growth of other nanoporous materials (zeolites) to provide a micro/macroporous composite material for a specific application [3]. Also it is possible to extend the range of applications for diatom frustules, limited by the properties of silica, substituting the silicon atoms with magnesium atoms placing the diatom in magnesium gas at 900° C for 4 h without losses of the structure [4]. Despite the beautiful pattern ornamentations, which are specie-specific and can be analyzed by light and electron microscopy, the optical properties of diatoms frustules are still unexplored. In this appendix, the optical properties of the silica frustule of a centric diatom, the *Coscinodiscus walesii*, are investigated: impressive morphological and physical analogies with porous silicon have been observed.

A.1 Diatoms Morphology

Biologists are used to classify diatoms on the basis of their symmetry: usually diatoms are divided in centric, which show radial symmetry as it can be seen in Figure A.1 (a), and pennate, which have lateral symmetry (Figure A.1 (b)). In order to analyze the properties of the diatoms, a cleaning procedure that destroys the external organic matrix

covering their siliceous frustules is mandatory. A mixture of acids of different strength is generally used for this purpose.

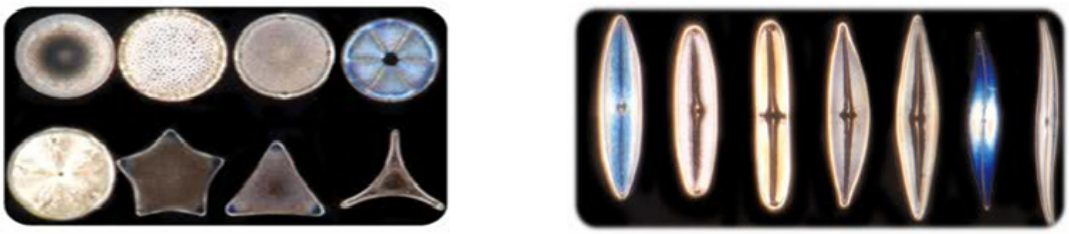

(a) (b)

Figure A.1. (a) Different centric diatoms species. (b) Different pennate diatoms species (Image source from Internet).

Some micro and nanostructured valves and less silicified frustules can be dissolved in strong acids. It is very important to accurately calibrate the strength of the mixture to avoid silica skeleton damages. The *Coscinodiscus wailesii* possesses highly silicified frustule, therefore the cleaning procedure uses highly concentrated acid. The samples analysed were cleaned using the following steps:

i. 50 ml of a highly concentrated, fixed phytobenthos sample was centrifuged at 3000 rpm for 10 min;
ii. the pellet was washed in distilled water 5 times to remove the excess of fixative;
iii. 2 ml of pellet was mixed with a similar volume of 97 % sulphuric acid for 5 min at 60°;
iv. the acid was removed and the pellet washed again in distilled water 5 times.

In Figure A.2 a SEM image of *Coscinodiscus wailesii* is reported. The inset B is a particular of diatom structure. The valves display regularly ordered and circular pores with diameter of about 500 nm (inset A). The pores are occluded by internal cribra with nanopores of 30-40 nm in diameter (inset B). The pores of the valves are in a regular repeating hexagonal lattice. As in the case of the porous silicon, an important parameter of the diatom is its porosity. The diatom porosity was calculated as the ratio between the total area occupied by the pores on the surface and the area of the simple hexagon. Thus a porosity value of about 0.53 was estimated for the considered sample.

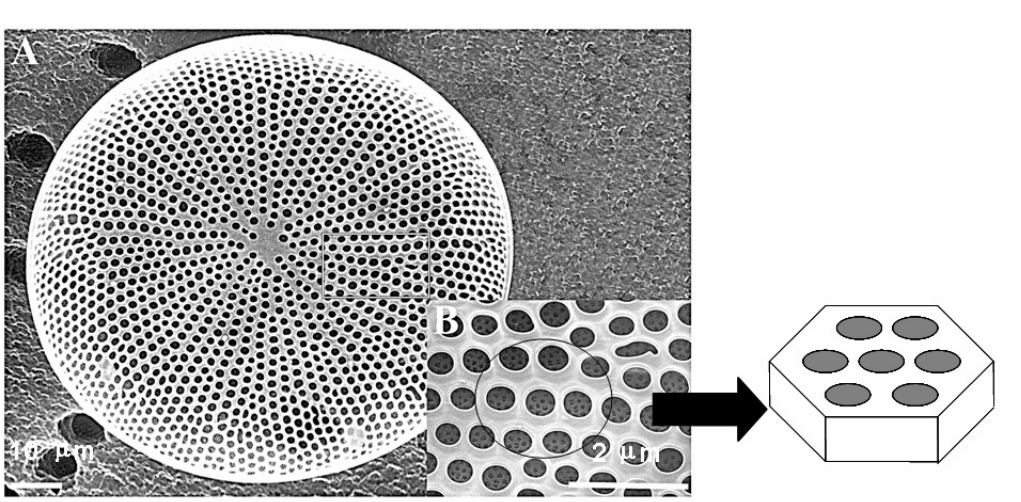

Figure A.2. Top view of a *Coscinodiscus wailesii* after the removal of organic material from the pores (inset A). In the inset B a particular of diatom structure is reported. The pores of the valves are in a regular repeating hexagonal lattice.

A.2 Optical Characterization

The reflectivity spectrum of the diatom was measured by using as source a white light directed on it through a Y fiber. The same fiber was used to guide the output signal to the optical spectrum analyzer. The spectrum was measured over the range 1000-1200 nm with a resolution of 0.2 nm. The diatom reflectivity spectrum is reported in Figure A.3. Typical fringes like a Fabry Perot interferometer are shown.

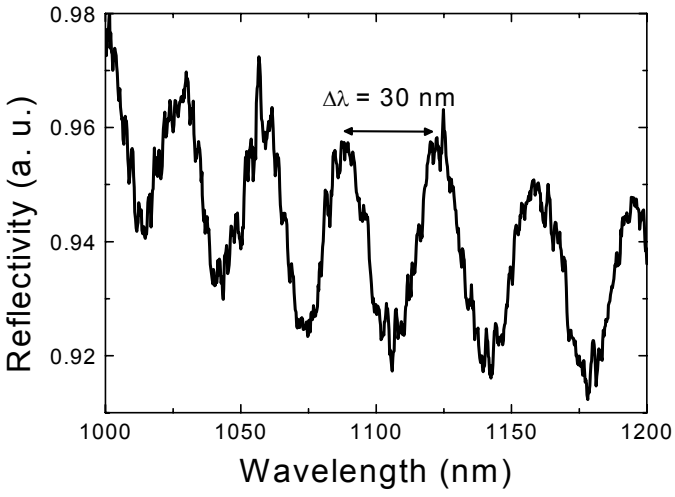

Figure A.3. Optical reflectivity spectrum of diatom. The difference between two successive maxima is 30 nm.

The refractive index of the diatom, n, was determined from the wavelengths of two successive maxima (λ_1 and λ_2) using the thickness d=15μm, measured by SEM, and the equation $n=\lambda_1\lambda_2/2d\Delta\lambda$. A value n=1.2 was obtained. Thus, using the Bruggemann Eq. (2.3), a porosity of 0.55, comparable with the value obtained by SEM analysis, was estimated.

A.3 Lensless Light Focusing

The areolae arrays of *Coscinodiscus walesii* are arranged on the diatom surface with a radial symmetry which is very similar to the one of some man-made optical devices, such as photonic crystal fibres or phase-locked arrays of optical fibres or lasers: the uncommon features of light propagation through these regular structures don't depend only on the interaction with the matter but also on the spatial order of the periodic lattice [5, 6]. Therefore, the light transmission characteristic of a single valve was investigated, by using the experimental set-up shown in Figure A.4. The central section of a diode laser beam (*@λ=785 nm*, elliptical spot size of approximately *2 mm*) was selected by a *100 μm* pinhole placed at *1 cm* from the glass slide to fit the valve dimension. The transmitted signal was collected by a 2 0x objective and recorded by a CCD camera (Leica DFC300 FX).

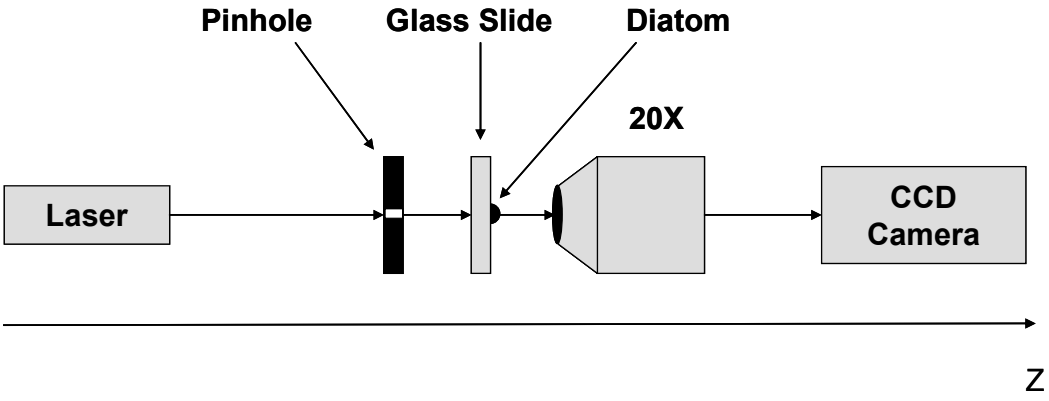

Figure A.4. The experimental set-up used to investigate the light transmission characteristic of the diatom valve. Distances are not in scale.

It was verified that the optical setup (pin-hole, glass slide and objective) without the diatom didn't change the features of the laser light: the beam profile divergence and its intensity changed less than *5 %* over a distance of *250 μm* from the focal plane of the diatom. The measurement started when the diatom surface was in the objective focal

plane; then, the transmitted light spot image was registered by moving the objective up to *200 μm* by steps of *4 μm*. It was found, quite surprisingly, that the valve acted as a microlens: the laser beam was highly focused at an output distance from the valve surface ranging from *100 μm* to *110 μm;* then the light beam diverged. The beam was confined in *8.1 μm* (value of the full width at half maximum) in its narrowest point, resulting in a spot size about *12* times smaller than the pinhole diameter (see Figures A.5 (a) and A.5 (b)).

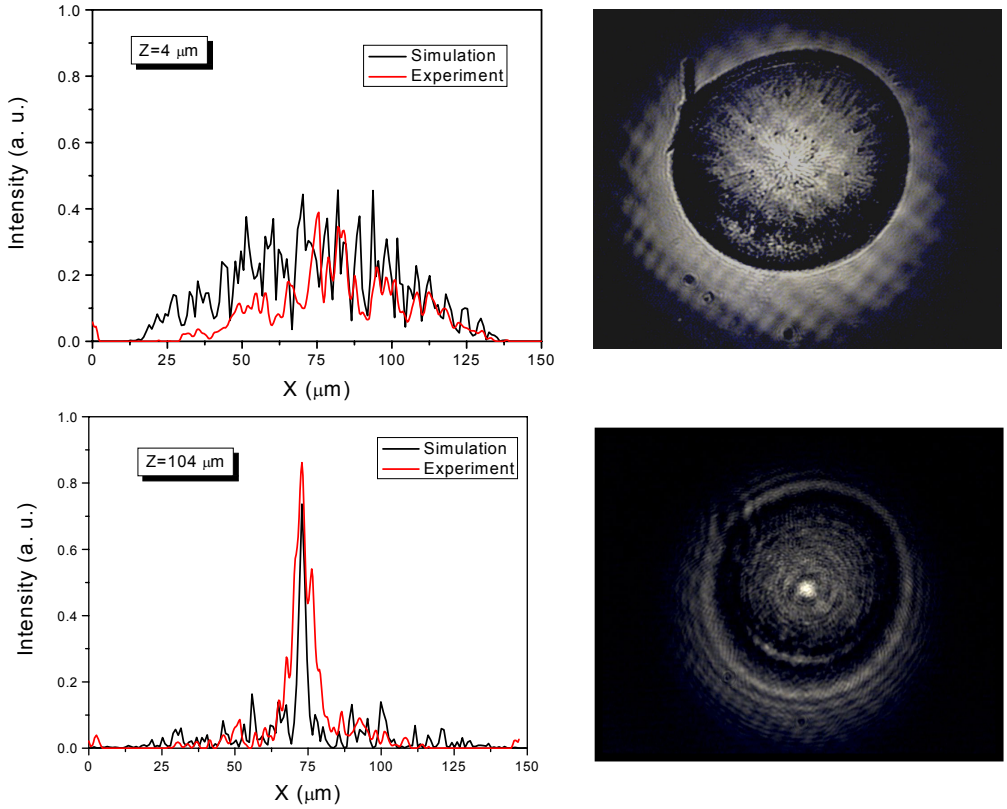

Figure A.5. (a) The intensity distribution of the transmitted light at the distance (z) of 4 μm (top plot) and 104 μm (bottom plot): the red line is the experimental recorded one, the black line is the numerical estimated. (b) The correspondent images of the diatom surface recorded by a CCD at the two distances considered.

The light focusing occurs at the centre of the diatom valve in correspondence of the uniform zone, free of areolae, which is about *15 μm* in size. Even if it's possible to demonstrate that the diatom valve could act as a guiding structure and hence support a guided mode in this defect [7], this focusing effect is attributed to a coherent superposition of the unfocused wave fronts coming from the about 600 areolae of *C.*

walesii valve which are regularly disposed on diatom surface: the light scattered by the holes on the diatom surface interferes constructively only at a fixed distance, which also depends on the holes spatial disposition, determining a well-defined spotlight. Moreover, the focusing effect found cannot be completely ascribed to the diffraction from a round obstacle, as in the well-known case of the Poisson-Arago spot [8]. The intensity of this bright spot, which appears in the shadow behind a circular obscuration, can be exactly evaluated in the frame of the Fresnel-Kirchoff or the Rayleigh-Sommerfeld diffraction models [9]. The intensity value of the Poisson-Arago spot increases continuously with the distance and saturates at $z/a \approx 4$, where a is the radius of the obstacle. In the case of the diatom observed this would mean a focusing distance of about 300 μm, which is outside the range investigated. In Figure A.6, the intensity of the spot center observed as a function of the distance is reported: the light converges with a complex modulation which cannot be simply modelled by diffraction. The numerical simulations based on this assumption qualitatively reproduce the behaviour of the experimental data.

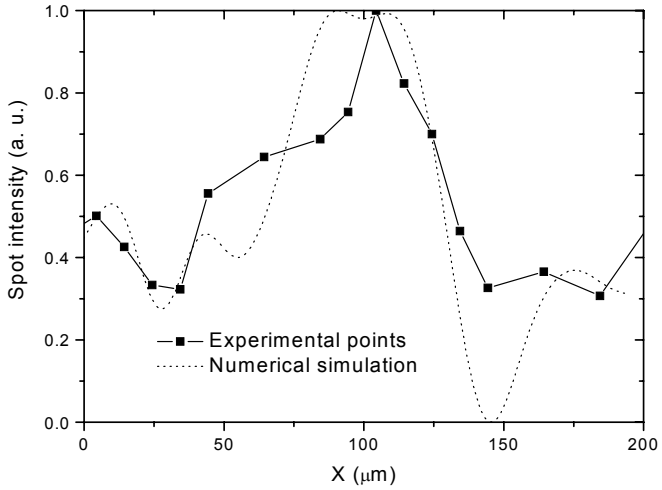

Figure A.6. Spot intensity as function of the distance.

In order to calculate the optical properties and analyze the light propagation through a real sample of diatom and not just exploiting a model of this organism, the electron microscope image of the tested valve was digitalised and the measured geometrical parameters used to simulate the optical transmission through it. The numerical calculations have been performed by a wide angle Beam Propagation Method, based on multi-steps Padè- wide angle technique [10-11]. The calculations grid is composed by

2000×2000×50 points and a (1, 1) Padè coefficient has been adopted in order to investigate the beam propagation with a divergence of about 30°. The valve refractive index value, used in numerical simulations, has been estimated by reflectivity measurement to be *1.43*, in accordance to the values elsewhere reported [12]. The inner structure of the diatom valve has been taken into account as a homogeneous layer of amorphous silica with proper thickness (*400 nm*), since the holes size in this ultrastructure is well below the light wavelength. The light intensity distribution on the diatom surface has been calculated and the colour plot reported in Figure A.7: from this picture is well evident that the highest contribution to the transmitted intensity comes from the valve holes.

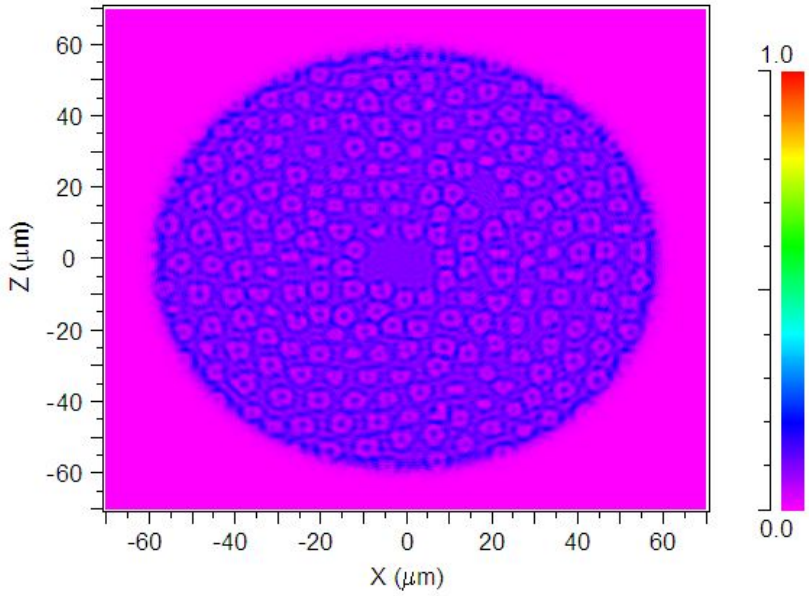

Figure A.7. Relative intensity of the light on the diatom valve surface.

The numerical results of the focusing simulation, plotted in Figure A.5 (a) as black curves, are in a good qualitative agreement with the experimental ones (red curves in Figure A.5 (b)). If the focusing effect really depends on the interference from the light scattered by the areolae, the focalisation distance would behave as the diffraction angle which is proportional to $1/\lambda$. In Figure A.8 the calculated focusing distances have been reported, as function of the incoming light wavelength, which are perfectly fitted by a rationale curve (i.e. $1/\lambda$ curve) thus clearly suggesting that the diatom focusing is a holes diffraction-driven effect. The discovery of the *C. walesii* focusing features really opens new opportunities in the field of microlenses and of diatom nanotechnology in general. Diatom based microlenses could be more flexible than those fabricated with

usual technologies [13], due to the intrinsic properties of their frustules: silica atoms can be substituted with other species without losing the structure [14], and since diatoms decrease in size through the succeeding generations, in a short period they can scale to nano-dimensions preserving symmetries and other characteristics [1].

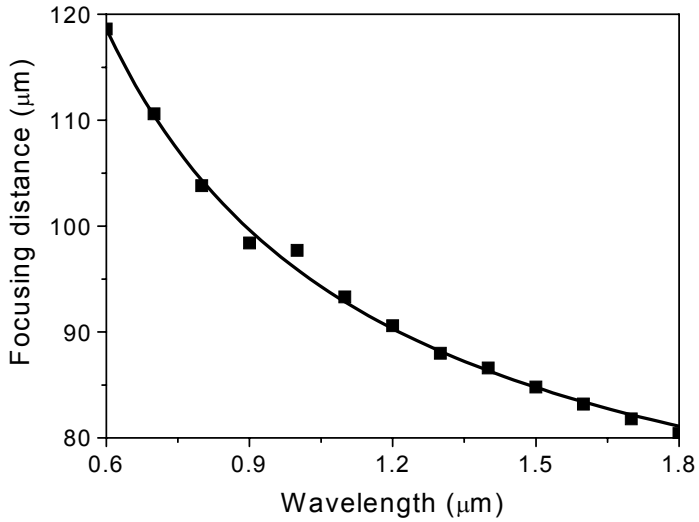

Figure A.8. The calculated focusing distances as a function of the light wavelength.

Furthermore, the diatoms have a very high reproduction rate that means lot of samples with their precise and reproducible nanometre scale features at very low production cost. The valves are easy to handle by standard micro-needles or micro-tips since geometry and material properties can make diatom frustules mechanically very strong, hence resistant to large physical forces [15]. Single valves could fit the top of an optical fibre to make a lensed fibre without modifying the glass core or, similarly, they could match the output of a vertical cavity surface emitting laser [16]. Other photonic micro-components which could benefit of diatoms focusing ability could be semiconductors and organic light emitting devices and in general all other optical micro-arrays. The focusing ability of the diatom's frustule could also have a biological function, which should of course be deepened in following researches. This mechanism could provide an effective way to concentrate the light with biologically useful wavelengths inside the diatoms protoplasm; indeed it is known that light intensity causes a redistribution of the chloroplast away from the frustule to the centre of the cell [17].

A.4 Photoluminescence and Optical Sensing by Diatoms

Recently, a study on the photoluminescence (PL) of diatoms has been reported [18]: under the 325 nm beam of He-Cd laser, authors found a broad peak at 2.75 eV (450 nm). In this paragraph, the effect of the surrounding atmosphere on the diatom PL spectra is investigated. To this aim, the frustules of the *C. walesii* were wet deposited on a single-polished, intrinsic silicon wafer, which gives a negligible contribution to photoluminescence (PL) signal at the wavelength considered. The PL was induced by c.w. He-Cd laser (Kimmon IK5651R-G) light at the wavelength 325 nm and measured at room temperature in a test chamber with quartz windows for optical access through a Triax 320 monochromator (Jobin-Yvon-Horiba) equipped by 1200 grooves/mm grating blazed for 500 nm and thermo-cooled charge-coupled device (CCD) camera. The spectra were recorded within an accumulation time of 3 s. The spot size of the laser beam was 1 mm^2, since the incident laser beam power was 20 mW, a light intensity of 20 mW/mm^2 resulted. In Figure A.9 the effect of diatom exposure to NO_2 is shown.

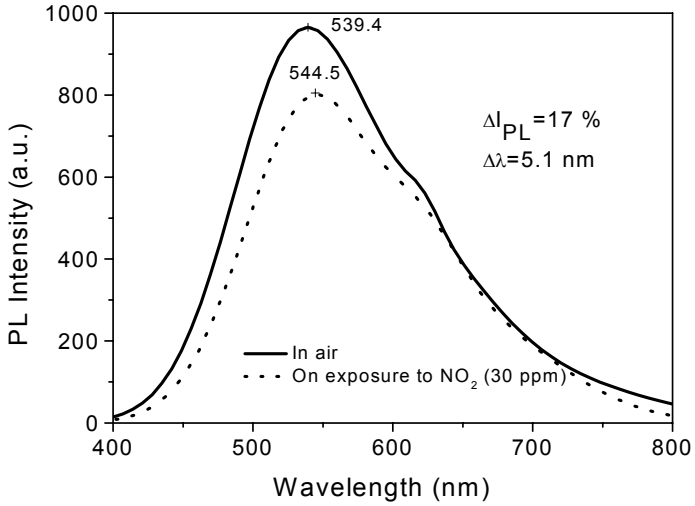

Figure A.9. Quenching of diatom photoluminescence spectrum in presence of NO_2.

The PL signal is quenched due to the electrophilic nature of NO_2 which can attract some electrons from the silica skeleton of diatoms and quench its photoluminescence. A stationary concentration of 30 ppm of NO_2 flowing into the test chamber induced a relative change of the PL intensity of about 17 %. The response time is of few seconds, about 2 s, and it depends on the gas diffusion in the test chamber: reducing the volume smaller response time can be obtained. The PL quenching effect is completely

reversible as soon as the gaseous atmosphere is replaced by air. Furthermore, it is worth nothing that the principal peak of the PL band shifts of 5.1 nm towards longer wavelengths, due to absorption of the gaseous substance into the nanometer pores of the diatom frustule which increases the average refractive index of the structures, as it happens in similar conditions to the porous silicon optical devices [19].

The effects on both the luminescent intensity and the band peak position registered on exposure to different substances suggest the possibility to obtain a dual-parameter optical sensor by using a free, simple to prepare, and almost ubiquitous material. The resolution of the experimental set-up could allow a sensitivity of few ppm, comparable with other common sensor devices [20].

References

[1] F. E. Round, R. M. Crawford, D.G. Mann, The diatoms. Biology & morphology of the genera, Cambridge University Press, Cambridge (1990).

[2] L. L. Brott, R. R. Naik, D. J. Pikas, S. M. Kirkpatrick, D. W. Tomlin, P. W. Whittlock, S. J. Clarson, M. O. Stone, "Ultrafast holographic nanopatterning of biocatalytically formed silica", *Nature* **413**, 291 (2001).

[3] M. W. Anderson, S. M. Holmes, N. Hanif, C. S. Cundy, "Hierarchical pore structures through diatom zeolitization", *Angew. Chem. Int. Ed.* **39**, 2707-2710, (2000).

[4] K. H. Sandhage, M. B. Dickerson, P. M. Huseman, M. A. Caranna, J. D. Clifton, T. A. Bull, T. J. Heibel, W. R. Overton, M. E. A. Schoenwaelder, "Novel, bioclastic route to self-assembled, 3D, chemically tailored meso/nanostructures: Shape-preserving reactive conversion of biosilica (diatom) microshells", *Adv. Mater.* **14**, 429 (2002).

[5] G. Josten , H. P. Weber, W. Luethy, "Lensless focusing with an array of phase-adjusted optical fibers", *Appl. Opt.* **28**, 5133-5137 (1989).

[6] M. De Stefano, L. De Stefano, "Nanostructures in diatom frustules: functional morphology of valvocopulae in Cocconeidacean monoraphid taxa", *Journal of Nanoscience and Nanotechnology* **5**, 15-24, (2005).

[7] J. D. Joannopoulus, R. D. Meade, J. N. Winn, Photonic crystals. Molding the flow of light, Princeton University Press, Princeton, NJ (1995).

[8] S. S. Hong, B. K. P. Horn, D. M. Freeman, M. S. Mermelstein, "Lensless focusing with subwavelength resolution by direct synthesis of the angular spectrum", *Applied Physics Letters* **88**, 261107 (2006).

[9] G. R. Wein, "A video technique for the quantitative analysis of the Poisson spot and other diffraction patterns", *Am. J. Phys.* **67**, 236 (1999).

[10] R. L. Lucke, "Rayleigh–Sommerfeld diffraction and Poisson's spot", *Eur. J. Phys.* **27**, 193 (2006).

[11] R. Scarmozzino, A. Gopinath, R. Pregla, S. Helfert, "Numerical Techniques for Modeling Guided-Wave Photonic Devices", *J. Selected Topics in Quantum Electronics* **6**, 150 (2000).

[12] G. R. Hadley, "Wide-angle beam propagation using Pade approximant operators", *Optics Letters* **17**, 1426 (1992).

[13] T. Fuhrmann, S. Landwehr, M. El Rharbi-Kucki, M. Sumper, "Diatoms as living photonic crystals", *Appl. Phys. B* **78**, 257-260 (2004).

[14] H. Ottevaere, H.Thienpont, "Comparative study of glass and plastic refractive microlenses and their fabrication techniques", Proceedings of the Symposium IEEE/LEOS Benelux Chapter, 218-221 (2002).

[15] M. R.Weatherspoon, S. M. Allan, E. Hunt, Y. Cai, K. H. Sandhage, "Sol-gel synthesis on self-replicating single-cell scaffolds: applying complex chemistries to nature's 3-D nanostructured templates", *Chem. Comm.* **5**, 651-653 (2005).

[16] C. E. Hamm, R. Merkel, O. Springer, P. Jurkojc, C. Maier, K. Prechtel, V. Smetacek, "Architecture and material properties of diatom shells provide effective mechanical protection", *Nature* **421**, 841-843 (2003).

[17] B. Stager, M. T. Gale, M. Rossi, "Replicated micro-optics for automotive applications", Proceedings of SPIE 5663, 238-245 (2005).

[18] K. S. A. Butcher, J. M Ferris, M. R. Phillips, in Proceedings of the 27th Annual A&NZIP Condensed Matter and Materials Meeting, edited by J. Cashion, T. Finlayson, D. Paganin, A. Smith, and G. Troup, 51–53 (2003).

[19] L. De Stefano, I. Rendina, L. Moretti, A. M. Rossi, S. Tundo, "Smart optical sensors for chemical substances based on porous silicon technology", *Applied Optics* **43**/**1**, 167-172 (2004).

[20] E. Massera, I. Nasti, L. Quercia, I. Rea, G. Di Francia, "Improvement of stability and recovery time in porous-silicon-based NO_2 sensor", *Sens. Act. B* **102**, 195-197 (2004).